To the Graduate Council:

I am submitting herewith a thesis written by Benjamin C. Johnson entitled “A Numerical Investigation of S-Duct Flows with Boundary-Layer Ingestion” I have examined the electronic copy of this thesis for form and content and recommend that it be accepted in partial fulfillment of the requirements for the degree of Master of Science, with a major in Computational Engineering.

Dr. Robert S. Webster
Major Professor

We have read this thesis
and recommend its acceptance:

Dr. W. Kyle Anderson

Dr. W. Roger Briley

Accepted for the Council:

Dr. Stephanie L. Bellar
Interim Dean, The Graduate School

A Numerical Investigation of S-Duct Flows with Boundary-Layer Ingestion

A Thesis Presented for the
Master of Science
Computational Engineering
The University of Tennessee, Chattanooga

Benjamin C. Johnson
May 2010

DEDICATION

My work is dedicated to my family and friends. To my family, who have made me what I am today. To my parents Gary and Karengaye, who taught me to be thorough, to go the extra mile, and to give 100% in every aspect of life. To all my friends, who have never stopped believing in me, and for their endless support while pursuing my dreams.

ACKNOWLEDGEMENTS

First, I want to share my appreciation to all the people at the Chattanooga SimCenter. Thank you for the chance to pursue my dreams. I am grateful for all the guidance and mentoring from fellow students, faculty, and staff. I want to thank Dr. D. Huddleston, Dr. T. Swafford, and Dr. R. Briley for creating this opportunity to further my education. I want to acknowledge and thank Dr. K. Anderson, Dr. R. Briley, and Dr. R. Webster for representing my thesis committee. Special thanks to Dr. Webster for serving as my committee chairperson and major professor. Your knowledge of computational engineering and continual guidance has sharpened my engineering skills. My appreciation also extends to Bruce Hilbert for his aid in the grid process. The SimCenter is a unique engineering experience and a phenomenal learning environmental. I am extremely honored to have been a part of it.

I want to thank Dr. C. Darvennes, Dr. S. Han, Dr. D. Huddleston, and Dr. C. Wilson for their guidance, mentoring, and teaching while at the Tennessee Technological University. Your letters of recommendation made this opportunity possible, and your joy for engineering has inspired me to be innovative and ingenious in my engineering practice.

I want to share my gratitude to the people at the NASA Glenn Research Center for their financial support through the research grant NNX07AO11A. My appreciation goes out to technical officer Dr. M. Hathaway, and Dr. K. Pham project POC, for giving me the opportunity to speak at the 2010 AIAA convention. Your support made my engineering experience at the Chattanooga SimCenter possible.

Finally, I want to thank Dr. Owens and others at NASA Langley Research Center for their engineering guidance, communications, and willingness to aid in this research.

ABSTRACT

The essence of this paper is to report the computational research conducted to further NASA's study of active flow control systems for a flush-mounted inlet with significant boundary-layer ingestion (BLI). In conjunction with a NASA-sponsored research grant, the aim is to further accumulate knowledge and insight on the effectiveness of flow control devices in reducing circumferential distortion. Using Computational Fluid Dynamics (CFD), this study seeks to validate wind tunnel results recorded by the NASA Langley Research Center. After numerically reproducing experimental data, the future goal is use CFD to simulate the interaction between the inlet and turbofan stage.

This study focused on NASA's air jet flow control devices, specifically a 16-jet version referred to as “configuration-10”. The accuracy and validity of the numerical solutions was dependent on their ability to match the following experimental values: mass flow rate through the S-duct, mass flow ratio, pressure measurements along the center line, and distortion coefficient at the aerodynamic interface plane. Three computational grids, containing 6.5, 30.5, and 36.9 million nodes, were constructed for the numerical simulations. The three grids varied in solid modeling techniques and grid element packing. Time limitations prevented the inclusion of results for the largest computational grid. Yet for the two smaller computational grids, the “Tenasi” flow solver was able to calculate valid numerical solutions for the “baseline” case (no jet flow) as well as low jet mass flow rate cases. High jet mass flow rate cases noticeably strayed from the experimental distortion measurements. Even though the numerical solutions did not replicate the experimental values for all mass flow ratio cases, this research significantly contributed to the knowledge and understanding of vorticity, flow characteristics, and distortion reduction for the BLI flush-mounted inlet. The CFD results

provide visual representations of the changing flow characteristics as the jet mass flow rate is increased, in addition to flow interaction with intrusive experimental measuring devices.

It is felt that better agreement with high-mass flow rate experimental cases can be calculated by numerically refining the jet boundary conditions and jet flow parameters. Overall, this paper reveals the steps taken in achieving early success in computationally verifying experimental data, and it discusses current actions being made towards further validating the numerical solutions.

TABLE OF CONTENTS

Chapter Page

LIST OF TABLES

Table Page

LIST OF FIGURES

Figure Page

NOMENCLATURE

VARIABLES:

a	Inlet lip length
a_s	Static speed of sound
A	Area
AIP	Aerodynamic interface plane
BLI	Boundary-layer ingestion
c_p	Heat capacity at constant pressure
c_v	Heat capacity at constant volume
CFD	Computational Fluid Dynamics
CFL	Courant–Friedrichs–Lewy number
D	Duct exit diameter
$DpCp_{avg}$	Circumferential Distortion
e	Internal energy
e_t	Total energy of an element of fluid
$\vec{f}$	Body force per unit mass of fluid
GDT	Gauss's Divergence Theorem
H_i	Inlet throat height
H_{max}	Cowl maximum height
ΔH	Inlet offset height
L	Reference length, Inlet length
L_a	Flat plate length ahead the X=0 plane
L_b	Flat plate length behind the X=0 plane
L_c	Cowl length
LHS	Left hand side
m	Mass
M	Mach number
MFR	Mass Flow Rate
MFR_{inlet}	Inlet mass flow rate
MFR_{jets}	Cumulative jet mass flow rate

$\vec{n}$	Unit normal vector defined positive outward
P_{jet}	Jet pressure
P_s	Static pressure
P_t	Total pressure
$\vec{P}$	Total stress in terms of force per unit area
Pr	Prandtl number
Pro-E	Pro Engineer 3-D Modeling Software
$\vec{q}$	Heat flux vector
$\vec{r}$	Position vector
R	Gas constant
RANS	Reynolds-Averaged Navier-Stokes
RHS	Right Hand Side
Re	Reynolds number
Re_D	Reynolds number with respect to exit diameter
RTT	Reynolds Transport Theorem
S	Surface
t	Time
T	Temperature
T_{jet}	Jet temperature
T_s	Static Temperature
T_t	Total temperature
u, v, w	Three velocity components
$\vec{u}$	Fluid velocity vector
$\vec{u}_s$	Velocity of the control volume surface
UTC	University of Tennessee at Chattanooga
UEET	Ultra Efficient Engine Technology
V	Volume
VLI	Viscous Layer Insertion
W_i	Inlet throat width
x, y, z	Cartesian coordinates

γ	Ratio of specific heats
δ	Kronecker delta, Boundary layer height
κ	Thermal conductivity
K	Bulk viscosity
λ	Second coefficient of viscosity
μ	Absolute viscosity
ξ, η, ζ	Curvilinear coordinates
ρ	Density
σ	Stress

SUPERSCRIPTS:

^	Non-dimensional variable
cv	Control volume
mv	Material volume

SUBSCRIPTS:

∞	Reference quantity
i, j, k	Indices for looping over multiple components

SYMBOLS:

∂	Partial differentiation
∇	Del operator

CHAPTER I
Introduction

In 1999, NASA created the Ultra Efficient Engine Technology (UEET) program to research and explore efficient alternatives to conventional transport configurations. The NASA X-48 Blended Wing Body (BWB) concept is the leading solution to a more fuel efficient air transport configuration. The X-48 concept was projected to weigh less, produce less noise, and consume 20% less fuel than conventional transport configurations.

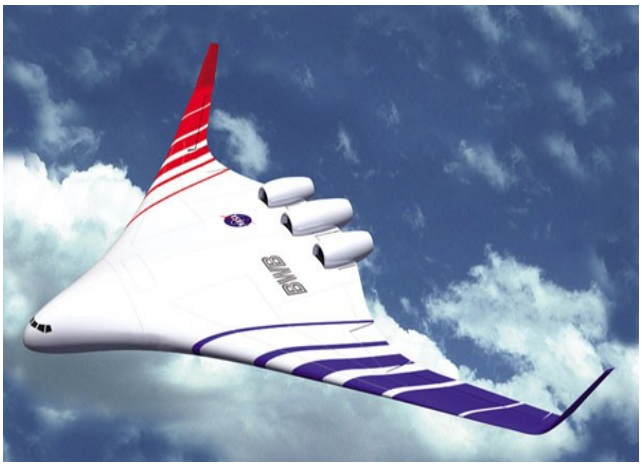

Figure 1:(left)X-48 blended-wing-body concept rendering. (Barnstorff, 2006)

Figure 2:(right) X-48 BWB prototype at Dryden Flight Research Center. (Creech, 2007)

In 2006, wind tunnel experiments on a 8.5% scale X-48 were conducted at the NASA Langley Research Center. In 2007, the 8.5% scale BWB prototype made its first flight at the Dryden Flight Research Center on Edwards Air Force Base. The X-48 concept was featured in the November issue of Time magazine for “Best inventions of the year for 2007”.

Notice in figure 1, the jet turbine engines appear to coincide with the centerline of the aircraft which increases efficiency by reducing drag. The initial concept design, shown in figure 1, would require a Boundary-Layer Ingesting (BLI) S-duct to redirect air flow to the jet turbine engines. Figure 2 shows the 8.5% scale flying X-48 prototype. Notice, the prototype no longer features BLI S-ducts, but the jet turbine engines are mounted on vertical pylons. The different engine configurations foreshadow future design compromises that would decrease the potential of the BWB design. Flow control devices for BLI inlets reduce circumferential distortion and uniform pressure values across the aerodynamic interface plane (AIP), also referred to as the fan face location. The engineering goal is to minimize drag by mounting the jet turbine engines close to the vertical centerline of the plane while maximizing engine efficiency by reducing circumferential distortion at the AIP. As a result, inlet flow control technology is crucial to the success of an ultra-efficient BWB concept.

In concordance with the NASA UEET program, the goal of this research is to support the development of commercial aircraft propulsion technologies that can reduce air travel's negative influences on the environment. From a propulsion stand point, the area of interest is energy efficiency and the reduction of fuel consumption. Through a NASA- sponsored research grant, the SimCenter at the University of Tennessee at Chattanooga (UTC) works to assist in the research and development of a flush-mounted, BLI, S-shaped inlet diffuser for a BWB engine design. Computational results for the air jet flow control devices need to agree with experimental wind tunnel results performed on a 2.5% scale inlet at the NASA Langley Research Center. Through the use of Computational Fluid Dynamics (CFD), the intent is to validate the “Tenasi” in-house flow solver code with further goals of analyzing the effectiveness of flow control devices

to reduce circumferential distortion at the AIP. By improving the pressure distribution at the the fan-face location or AIP, the turbo fan engine should experience an increase in efficiency and effectiveness, as well as decreasing the likelihood of compressor instabilities. The long term project goal is to numerically study the coupled fluid interaction between a turbine fan stage and BLI inlet.

From a CFD perspective, the complexity of this fluid flow problem lies in the simulation's ability to numerically capture the vorticity within the inlet as well as the flow physics around the air jet flow control devices. The jet flow control devices were angled to directly counter the vorticity building along the S-duct walls. This study sought to accurately simulate the jet interaction with the main fluid flow through the S-duct and to provided insight into the flow control jets' ability to diminish the counter rotating vortices present in S-bend diffuser inlets.

This study focused on the 16-jet version referred to as “configuration-10” set up because experimental evidence showed considerable reductions in distortion at the AIP for relatively low jet mass flow rates with this configuration. With aid from the NASA Langley Research Center, experimental data for the 16-jet “configuration-10” test cases were shared via a Microsoft Excel sheet recorded by Owens, Allan, and Gorton.(2006) In their documentation, the 16-jet version of the “configuration-10” experiment was denoted as test case R094. A variety of jet mass flow rates were tested and recorded as R094 Pt. 771, R094 Pt. 773, and so on. The Pt. 771 case has a jet mass flow rate equal to zero. In other words, the jet flow was turned off. Through the course of this study, the Pt. 771 case is referred to as the “baseline” case. A surface definition database file and engineering drawings were provided by the NASA Langley Research Center. The “Inlet-A” dimensions recorded by Berrier (2005) were also used to obtain a coherent and

complete virtual model of the BLI inlet. The air jet flow control devices were appended to the S-duct geometry in agreement with the "Inlet-A" engineering drawings.

Three computational grids were constructed during the duration of this research. Variations in grid methodology produced grids containing 6.5, 30.5, and 36.9 million nodes. The three grids were simulated to converge to a steady-state solution using the parallel "Tenasi" flow solver. "Tenasi" was used on the variable-Mach mode with the Mentor one-equation turbulence model. Converged "baseline"numerical solutions, for each respective grid, were used as restart files for calculating numerical solutions for various mass flow ratios. Results for the 36.9 million node grid are not presented in the results portion of this paper due to time limitations, but the grid was discussed to provide a glimpse of the ongoing research.

Including the introduction, the paper presented contains eight chapters. Chapter two covers the derivation of the integral and differential forms of the governing conservation equations. The non-dimensionalization of variables and coordinate transformation processes are also documented in Chapter two. A brief description of the "Tenasi" flow solver and its features is included in Chapter three. Chapter four describes the steps taken in building a virtual solid model for rendering the jet flow control devices. Again, the 2.5% scale S-duct geometry was constructed according to dimensions presented by Owens and Berrier.(2008, 2005) Chapter five discusses the iterative grid process used in the construction of the three computational grids. Chapter five also explains the key differences in the grid design and methodology. Chapter six establishes the validation criteria for achieving an accurate numerical solution. Documentation on boundary conditions, initial conditions, and post processing procedures are incorporated in Chapter six. Chapter seven presents the computational results. Numerical solutions

will be judged on their ability to match experimental values and show intuitive fluid flow characteristics common to S-bend diffuser inlets. Chapter seven also presents new questions in regards to the influence of intrusive experimental measuring devices, and it discusses possible revisions to aid future research. Chapter eight reviews the importance of the discoveries.

CHAPTER II
Governing equations

All laws for fluid and solid mechanics are derived for an arbitrary quantity of mass of fixed identity called a system. It is more intuitive to see how these laws pertain to a solid quantity of mass, but a fluid quantity of mass might need a more detailed explanation. Chapter two explains the steps taken in applying these laws of mechanics to a fluid system of fixed identity. To begin, the chapter presents the difference between material volumes (MV) and control volumes (CV), followed by the derivation of the integral form of the conservation equations. Also, the chapter discusses the technique used to convert the integral form of the governing equations to the differential form. The non-dimensionalization of variables procedure and coordinate transformation arithmetic are shown to complete the derivation of the governing conservation equations, also referred to as the Navier-Stokes equations.

A. Derivation of the Integral Form of the Governing Conservation Equations

To rewrite the basic laws of mechanics for a fluid system, the Reynolds Transport Theorem (RTT) is applied to a specific region which the fluid travels. Figure 2.A.1 shows a system of an arbitrary quantity of mass of fixed identity.

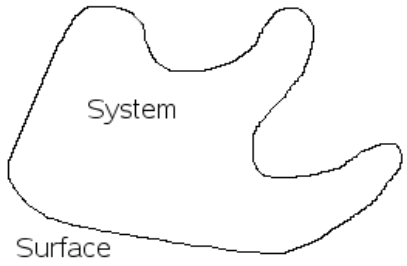

Figure 3: System of an arbitrary quantity of mass of fixed identity.

The system is made up of two components. The first portion is the surface boundary specifying the system of mass, and the second is the volume encapsulated by the surface boundary. The RTT equations are best visualized in the integral form as a reminder of the three dimensionality of the system. Fluid flow passing through the system is a function of time. Again, the RTT equations apply to the systems two components: the surface (S) and the volume (V) . Both, the surface and the volume can change position. Thus the surface and volume are functions with respect to time, $S(t)$ and $V(t)$. Just as the system is made up of a surface and volume, the RTT equations are written for a material and control volume. Superscripts MV and CV will be used to clarify which type of volume is being discussed.

A material volume is defined as being some arbitrary, moving, deforming volume which always contains the same, identifiable, fixed amount of fluid particles. Shown below is the integral form of the RTT equation for a material volume.

$$\frac{d}{dt}\iiint_{V^{mv}(t)} F(\vec{r},t)\,dV^{mv} = \iiint_{V^{mv}(t)} \frac{\partial F}{\partial t}\,dV^{mv} + \iint_{S^{mv}(t)} F(\vec{r},t)(\vec{u}\cdot\vec{n})\,dS^{mv} \quad (2.A.1)$$

A control volume is described as being some arbitrary, moving, deforming volume where fluid particles are allowed to pass through the surface. Likewise the integral form of the RTT equation for a control volume is listed below.

$$\frac{d}{dt}\iiint_{V^{cv}(t)} F(\vec{r},t)\,dV^{cv} = \iiint_{V^{cv}(t)} \frac{\partial F}{\partial t}\,dV^{cv} + \iint_{S^{cv}(t)} F(\vec{r},t)(\vec{u}_s\cdot\vec{n}^{cv})\,dS^{cv} \quad (2.A.2)$$

For both equations 2.A.1 and 2.A.2, the following is true.

F = some physical property per unit volume

$\vec{u}$ = local fluid velocity vector

$\vec{n}$ = unit normal vector defined positive outward

$\vec{u}_s$ = local velocity of the control volume surface

$\vec{r}$ = local position vector

The control volume surface has three velocity scenarios.

1. $\vec{u}_s=0$ Or $\vec{u}_s=constant$; acceleration, $\frac{d\vec{u}_s}{d\vec{r}}$, equals zero. The CV surface is at rest or in motion, respectively.
2. $\vec{u}_s=\vec{u}_s(t)$; the CV surface is moving non-uniformly as a function of time, t , without a change in shape.
3. $\vec{u}_s=\vec{u}_s(\vec{r},t)$; the CV surface is moving and changing shape.

During the special case when the material volume and the control volume instantaneously overlap, the RTT equation for a MV becomes the following.

$$\frac{d}{dt}\iiint_{V^{mv}} F(\vec{r},t)\,dV^{mv}=\iiint_{V^{cv}(t)} \frac{\partial F(\vec{r},t)}{\partial t}\,dV^{cv}+\iint_{S^{cv}(t)} F(\vec{r},t)(\vec{u}\cdot\vec{n}^{cv})\,dS^{cv} \quad (2.A.3)$$

Subtracting the equation for a CV (2.A.2), equation 2.A.3 becomes the following.

$$\begin{aligned}\frac{d}{dt}\iiint_{V^{mv}(t)} F(\vec{r},t)\,dV^{mv}-\frac{d}{dt}\iiint_{V^{cv}(t)} F(\vec{r},t)\,dV^{cv}=\iiint_{V^{cv}(t)} \frac{\partial F}{\partial t}\,dV^{cv}\\ -\iiint_{V^{cv}(t)} \frac{\partial F}{\partial t}\,dV^{cv}+\iint_{S^{cv}(t)} F(\vec{r},t)(\vec{u}\cdot\vec{n}^{cv})\,dS^{cv}-\iint_{S^{cv}(t)} F(\vec{r},t)(\vec{u}_s\cdot\vec{n}^{cv})\,dS^{cv}\end{aligned} \quad (2.A.4)$$

Notice the first and second term on the right hand side (RHS) cancel out, resulting in the following.

$$\begin{aligned}\frac{d}{dt}\iiint_{V^{mv}(t)} F(\vec{r},t)\,dV^{mv}=\frac{d}{dt}\iiint_{V^{cv}(t)} F(\vec{r},t)\,dV^{cv}\\ +\iint_{S^{cv}(t)} F(\vec{r},t)(\vec{u}-\vec{u}_s)\cdot\vec{n}^{cv}\,dS^{cv}\end{aligned} \quad (2.A.5)$$

For the case when the two volumes coincide, the RTT equation tells us the time-rate-of-change of quantity F within a MV is equal to the time-rate-of-change of the same quantity F within the CV plus the amount of quantity F passing through the surface boundary at any instance in time.

With equation 2.A.5, we can derive the conservation equations. Allow X to represent an extensive property. Recall, an extensive property is inherently dependent upon the amount of material under consideration.

$$X = \iiint_V F(\vec{r}, t)\, dV \tag{2.A.6}$$

Further, let the following be true for our quantity F

$$F = \rho x \tag{2.A.7}$$

where

ρ = amount of mass per unit volume

x = amount of X per unit mass

Inserting equation 2.A.7 into 2.A.5, we arrive at a simplified form of the RTT equation

$$\left[\frac{dX}{dt}\right] = \frac{d}{dt}\iiint_{V^{cv}(t)} \rho\, x\, dV^{cv} + \iint_{S^{cv}(t)} \rho\, x(\vec{u} - \vec{u}_s)\cdot\vec{n}^{cv}\, dS^{cv} \tag{2.A.8}$$

It is key to note that the left hand side (LHS) of equation 2.A.8 is for a fixed mass system.

Conservation of Mass Equation

To derive the conservation of mass equation, let the following be true.

$$X = m = mass \tag{2.A.13}$$

Recall x is the amount of X per unit mass.

$$x = \frac{X}{m} = 1 \tag{2.A.14}$$

An expression for the conservation of mass equation is formed by inserting equation 2.A.13 and 2.A.14 into equation 2.A.8.

$$\left[\frac{dm}{dt}\right] = \frac{d}{dt}\iiint_{V^{cv}(t)} \rho\, dV^{cv} + \iint_{S^{cv}(t)} \rho(\vec{u} - \vec{u}_s)\cdot\vec{n}^{cv}\, dS^{cv} \tag{2.A.15}$$

Since the rate of change of the mass for the system is constant by definition with respect to time, equation 2.A.15 simplifies to the following.

$$\frac{d}{dt}\iiint_{V^{cv}(t)} \rho \, dV^{cv} + \iint_{S^{cv}(t)} \rho \, (\vec{u} - \vec{u}_s) \cdot \vec{n}^{cv} \, dS^{cv} = 0 \qquad (2.A.16)$$

Note the integral form of the conservation of mass equation is valid for moving and deforming control volumes. Also, notice that the first term of the LHS is the time-rate-of-change with in the CV. The second term of the LHS is the net flux of mass passing through the surface of the control volume.

Conservation of Momentum Equation

Starting with equation 2.A.8, we perform the same procedure on the conservation of momentum equation. First recall, Newton's second law of motion says that the sum of all external forces, for a fixed mass system, is equal to the time rate of change of momentum of the system.

$$\sum \vec{F} = \frac{d}{dt}(m\vec{u}) \qquad (2.A.17)$$

$$X = m\vec{u} \quad \text{and} \quad x = \frac{X}{m} = \frac{(m\vec{u})}{m} = \vec{u} \qquad (2.A.18)$$

Inserting both forms of equation 2.A.18 into equation 2.A.8, we obtain the integral form of the conservation of momentum equation for a fixed mass system.

$$\left[\frac{d(m\vec{u})}{dt}\right] = \sum \vec{F} = \frac{d}{dt}\iiint_{V^{cv}(t)} \rho \, \vec{u} \, dV^{cv} + \iint_{S^{cv}(t)} \rho \, \vec{u} (\vec{u} - \vec{u}_s) \cdot \vec{n}^{cv} \, dS^{cv} \qquad (2.A.19)$$

Velocities $\vec{u}$ and $\vec{u}_s$ are measured relative to an inertial, non accelerating, reference frame. Notice the velocity variable is a vector component made up of three directional components. Note $\sum \vec{F}$ is the vector sum of all forces acting on the CV. Finally, notice equation 2.A.19 is valid for moving and deforming control volumes.

In fluid motion, there are two types of forces that influence the control volume: body forces and surface forces. Body forces act on a mass from a distance like gravity and electromagnetic forces.

$\vec{f}$ = body force per unit mass of fluid

Total body forces acting on a mass of fluid within a control volume can be calculated by the following expression for an instantaneous moment in time.

$$total\ body\ \ forces = \iiint_{V^{cv}(t)} \rho\, \vec{f}\, dV^{cv} \tag{2.A.20}$$

Surface forces originate from normal stresses due to fluid pressure and shear stresses due to viscous effects.

$\vec{P}$ = total stress in terms of force per unit area

The total stress term accounts for both normal and shear stresses acting on a control volume. The complexity of the normal and shear stress components are discussed momentarily, but for now let the following be true.

$$total\ surface\ \ forces = \iint_{S^{cv}(t)} \vec{P}\, dS^{cv} \tag{2.A.21}$$

Inserting equations 2.A.20 and 2.A.21 into equation 2.A.19, the integral form of the momentum equation becomes the following.

$$\begin{aligned} \iiint_{V^{cv}(t)} \rho\, \vec{f}\, dV^{cv} + \iint_{S^{cv}(t)} \vec{P}\, dS^{cv} = \frac{d}{dt} \iiint_{V^{cv}(t)} \rho\, \vec{u}\, dV^{cv} \\ + \iint_{S^{cv}(t)} \rho\, \vec{u}(\vec{u} - \vec{u}_s) \cdot \vec{n}^{cv}\, dS^{cv} \end{aligned} \tag{2.A.22}$$

The LHS is the sum of the body and surface forces acting on the CV. The RHS is the sum of the time-rate-of-change of momentum within the CV and the net flux of momentum passing through the CV. As stated earlier, the total stress vector $\vec{P}$ can be broken up

into 9 components. (3 normal stresses σ_{ii} and 6 shear stresses σ_{ij}) Recall, stress describes the amount of force distributed over an amount of unit area.

$$stress = \sigma_{ij} = \frac{force}{unit\ area} \tag{2.A.23}$$

where i and j loop over the three directional components which can be rewritten with subscripts 1, 2, or 3. The following matrix shows the linear algebra in matrix form for calculating the vector components of $\vec{P}$.

$$\begin{bmatrix} P_1 \\ P_2 \\ P_3 \end{bmatrix} = \begin{bmatrix} \sigma_{11} & \sigma_{21} & \sigma_{31} \\ \sigma_{12} & \sigma_{22} & \sigma_{32} \\ \sigma_{13} & \sigma_{23} & \sigma_{33} \end{bmatrix} \begin{bmatrix} n_1 \\ n_2 \\ n_3 \end{bmatrix} \tag{2.A.23}$$

Note that the normal stresses fall on the main diagonal of the stress tensor. We can denote a surface normal vector as $\vec{n}$ with Cartesian components n_1 , n_2 and n_3 . The matrix algebra presented in equation 2.A.23 can also be written in tensor form. Shown below is one component of the the total stress calculation.

$$P_1 = \sigma_{11} n_1 + \sigma_{21} n_2 + \sigma_{31} n_3 = \sigma_{k1} n_k \tag{2.A.24}$$

Notice, equation 2.A.24 can be rewritten in tensor, i and j , form. The tensor form allows the matrix algebra of equation 2.A.23 to be written as one expression.

$$P_j = \sigma_{ij} n_i \tag{2.A.25}$$

Replacing vector $\vec{P}$ with equation 2.A.25 , we arrive at the final integral form of the conservation of momentum equation. For consistency purposes, the whole equation will be written in tensor notation.

$$\begin{aligned} \iiint_{V^{cv}(t)} \rho\ \vec{f}_j\, dV^{cv} + \oiint_{S^{cv}(t)} \sigma_{ij} n_i^{cv}\, dS^{cv} = \frac{d}{dt} \iiint_{V^{cv}(t)} \rho\, \vec{u}_j\, dV^{cv} \\ + \oiint_{S^{cv}(t)} \rho\, \vec{u}_j (\vec{u}_i - \vec{u}_{s_i}) \cdot n_i^{cv}\, dS^{cv} \end{aligned} \tag{2.A.26}$$

Conservation of Energy Equation

The final governing equation to be derive is the conservation of energy equation, also known as the 1st Law of Thermodynamics.

[Energy Added To a System] – [Energy Taken Out of a System]

= [Change of energy of system] (2.A.27)

Notice the LHS represents the rate-of-change of the total energy coming in and out of a fluid. The RHS monitors change of energy within the system due to work and heat. Work is a result of external forces. Heat transfer, to or from the fluid, is done by conduction. With this knowledge, equation 2.A.27 becomes the following.

[Energy Added] – [Energy Removed] = [Work Added]

+ [Heat Added/Removed] (2.A.28)

Let the following be true.

$$e_t = e + \frac{1}{2}\vec{u}\cdot\vec{u} \tag{2.A.29}$$

where

e_t = total energy of an element of fluid

The first term on the RHS is the internal energy per unit mass. The second term represents the kinetic energy per unit mass. Equation 2.A.29 can be written for a MV, as shown below.

$$\oiiint_{V^{mv}(t)} \rho\, e_t \, dV^{mv} = \oiiint_{V^{mv}(t)} \rho\,(e + \frac{1}{2}\vec{u}\cdot\vec{u})\, dV^{mv} \tag{2.A.30}$$

Recall, work is the force times distance, $\vec{F}\cdot d\vec{r}$,over an increment of time, dt . The rate of doing work can be expressed in the following equation.

$$\vec{F}\cdot\frac{d\vec{r}}{dt} \tag{2.A.31}$$

Notice that the time-rate-of-change of distance with respect to time is equivalent to velocity.

$$\frac{d\vec{r}}{dt}=\vec{u} \tag{2.A.32}$$

By substituting equation 2.A.32 into equation 2.A.31, we arrive at the following equation.

$$\vec{F}\cdot\vec{u} \tag{2.A.33}$$

Recall, work can be added to a system by body forces and surface forces. Work due to body forces has the following equation:

$$work\ done\ by\ body\ forces=\iiint_{V^{mv}(t)}\vec{u}\cdot\rho\vec{f}\,dV^{mv} \tag{2.A.34}$$

Likewise, work added by surface forces has the following equation:

$$work\ done\ by\ surface\ forces=\iint_{S^{mv}(t)}\vec{u}\cdot\vec{P}\,ds^{mv} \tag{2.A.35}$$

Before deriving the conservation of energy equation, we should discuss the second term on the RHS of equation 2.A.28. Heat, $\vec{q}$, due to conduction leaves the fluid through its surfaces. As a result, heat due to conduction is negative by convention. Conductive heat flux for a MV surface can be expressed by the following equation.

$$q_t=\iint_{S^{mv}(t)}\vec{q}\cdot\vec{n}\,ds^{mv} \tag{2.A.36}$$

Recall, we are considering the scenario where the MV and CV instantaneously coincide with each other. Insert equations 2.A.34, 2.A.35, and 2.A.36 to equation 2.A.8 while letting the following be true.

$$X=\frac{total\ energy}{volume} \tag{2.A.37}$$

$$x=\frac{X}{m}=e+\frac{1}{2}\vec{u}\cdot\vec{u} \tag{2.A.38}$$

Doing this, we arrive at an integral form of the conservation of energy equation for a fixed mass system.

$$\begin{aligned}&\frac{d}{dt}\iiint_{V^{cv}(t)}\rho\left(e+\frac{1}{2}\vec{u}\cdot\vec{u}\right)dV^{cv}\\&+\iint_{S^{cv}(t)}\rho\left(e+\frac{1}{2}\vec{u}\cdot\vec{u}\right)(\vec{u}-\vec{u}_s)\cdot\vec{n}^{cv}\,ds^{cv}=\iint_{S^{cv}(t)}\vec{u}\cdot\vec{P}\,ds^{cv}\\&+\iiint_{V^{cv}(t)}\vec{u}\cdot\rho\vec{f}\,dV^{cv}-\iint_{S^{cv}(t)}\vec{q}\cdot\vec{n}^{cv}\,ds^{cv}\end{aligned}\qquad(2.A.39)$$

Since the conservation of momentum equation 2.A.26 is in an i and j tensor notation, it is helpful to have consistent notation among the three governing equations. Thus, the conservation of mass equation 2.A.16 is rewritten in tensor form.

$$\frac{d}{dt}\iiint_{V^{cv}(t)}\rho\,dV^{cv}+\iint_{S^{cv}(t)}\rho(u_j-u_{s_j})\cdot n_j^{cv}\,ds^{cv}=0\qquad(2.A.40)$$

As seen in equation 2.A.26, the tensor form of the conservation of momentum equation is the following.

$$\begin{aligned}&\iiint_{V^{cv}(t)}\rho f_j\,dV^{cv}+\iint_{S^{cv}(t)}\sigma_{ij}n_i^{cv}\,ds^{cv}=\frac{d}{dt}\iiint_{V^{cv}(t)}\rho u_j\,dV^{cv}\\&+\iint_{S^{cv}(t)}\rho u_j(u_i-u_{s_i})\cdot n_i^{cv}\,ds^{cv}\end{aligned}\qquad(2.A.41)$$

Likewise, the conservation of energy equation in tensor form is shown below.

$$\begin{aligned}&\frac{d}{dt}\iiint_{V^{cv}(t)}\rho\left(e+\frac{1}{2}u_j\cdot u_j\right)dV^{cv}\\&+\iint_{S^{cv}(t)}\rho\left(e+\frac{1}{2}u_j\cdot u_j\right)(u_i-u_{s_i})\cdot n_i^{cv}\,ds^{cv}=\iint_{S^{cv}(t)}u_j\cdot\sigma_{ij}n_i^{cv}\,ds^{cv}\\&+\iiint_{V^{cv}(t)}\rho u_j f_j\,dV^{cv}-\iint_{S^{cv}(t)}q_j\cdot n_j^{cv}\,ds^{cv}\end{aligned}\qquad(2.A.42)$$

Keep in mind, the three governing conservation equations are for non-reacting fluid flow for a moving and deformable control volume. Notice, equations 2.A40 through 2.A42 monitor control volumes only. As a result, the superscript denoting a control volume can be dropped, knowing equations will be dealing with control volumes only from this point on.

B. Transformation of the Integral Form to the Differential Form and Closing Off the System of Equations

The next step in the derivation process is to convert the integral form of the equations into a differential form. To do so, Gauss's Divergence Theorem (GDT) is used on the integral form of the governing equations. For an arbitrary vector $\vec{A}$, GDT states

$$\iiint_V \vec{\nabla}\cdot\vec{A}\,dV = \iint_S \vec{A}\cdot\vec{n}\,ds \tag{2.B.1}$$

Similarly, GDT can be written in tensor form.

$$\iiint_V \frac{\partial A_j}{\partial x_j}\,dV = \iint_S A_j n_j\,ds \tag{2.B.2}$$

Using 2.B.2, let's convert equations 2.A40, 2.A.41, and 2.A42 from tensor form to a differential form. We begin with the conservation of mass equation, as seen in equation 2.A.40.

$$\frac{d}{dt}\iiint_{V(t)} \rho\,dV + \iint_{S(t)} \rho(u_j - u_{s_j})\cdot n_j\,ds = 0 \tag{2.B.3}$$

If we make the simplifying assumption that our CV is fixed in space and non-deforming, $V(t)$ and $S(t)$ are no longer a function with respect to time and $u_{s_j} = 0$.

Implementing these simplifications, the conservation of mass equation 2.B.3 becomes

$$\iiint_V \frac{\partial \rho}{\partial t}\,dV + \iint_S \rho\,u_j n_j\,ds = 0 \tag{2.B.4}$$

Note, the partial with respect to time was moved inside the integral. Applying GDT to the second term on the LHS, we arrive at the following.

$$\iiint_V \frac{\partial \rho}{\partial t}\,dV + \iiint_v \frac{\partial}{\partial x_j}(\rho u_j)\,dV = 0 \tag{2.B.5}$$

The next step is to combine like terms.

$$\iiint_V \left[\frac{\partial \rho}{\partial t} + \frac{\partial}{\partial x_j}(\rho u_j)\right] dV = 0 \tag{2.B.6}$$

Since our volume is arbitrary, the integrand falls out and we arrive at the differential form of the mass conservation equation.

$$\frac{\partial \rho}{\partial t}+\frac{\partial}{\partial x_j}(\rho u_j)=0 \tag{2.B.7}$$

Performing the same transformation procedure to the conservation of momentum equation, we begin with the tensor notation as seen in equation 2.A.41.

$$\begin{aligned}\iiint_{V(t)} \rho f_j \, dV+\oiint_{S(t)} \sigma_{ij} n_i \, ds=\frac{d}{dt}\iiint_{V(t)} \rho u_j \, dV \\ +\oiint_{S(t)} \rho u_j (u_i-u_{s_i})\cdot n_i \, ds\end{aligned} \tag{2.B.8}$$

Remembering our control volume is fix in space and is non-deforming, we move all integrals to the LHS.

$$\frac{d}{dt}\iiint_V \rho u_j \, dV+\oiint_S \rho u_j u_i \cdot n_i \, ds-\oiint_S \sigma_{ij} n_i \, ds-\iiint_V \rho f_j \, dV=0 \tag{2.B.9}$$

Apply the GDT.

$$\iiint_V \left[\frac{\partial}{\partial t}(\rho u_j)+\frac{\partial}{\partial x_i}(\rho u_j u_i)-\frac{\partial \sigma_{ij}}{\partial x_i}-\rho f_j\right] dV=0 \tag{2.B.10}$$

Drop the integrand and we arrive at the differential form of the momentum equation.

$$\frac{\partial}{\partial t}(\rho u_j)+\frac{\partial}{\partial x_i}(\rho u_j u_i)-\frac{\partial \sigma_{ij}}{\partial x_i}-\rho f_j=0 \tag{2.B.11}$$

Doing the same for the conservation of energy equation, we start with the integral form of the equation as seen in 2.A.42. Applying the CV simplifying assumption, equation 2.A.42 becomes the following.

$$\begin{aligned}\frac{d}{dt}\iiint_V \rho\left(e+\frac{1}{2}u_j\cdot u_j\right) dV \\ +\oiint_S \rho\left(e+\frac{1}{2}u_j\cdot u_j\right) u_i\cdot n_i \, ds=\oiint_S u_j\cdot \sigma_{ij} n_i \, ds \\ +\iiint_V \rho u_j \, f_j \, dV-\oiint_S q_j\cdot n_j \, ds\end{aligned} \tag{2.B.12}$$

Move all integrals to the LHS and apply GDT.

$$\iiint_V \left[\frac{\partial}{\partial t}\left[\rho(e+\frac{1}{2}u_j \cdot u_j)\right] + \frac{\partial}{\partial x_i}\left[\rho(e+\frac{1}{2}u_j \cdot u_j)u_i\right] - \frac{\partial}{\partial x_i}(u_j \cdot \sigma_{ij}) - \rho u_j f_j + \frac{\partial q_j}{\partial x_j}\right] dV = 0$$

(2.B.13)

Drop the integrand and we have the differential form of the energy equation.

$$\frac{\partial}{\partial t}\left[\rho(e+\frac{1}{2}u_j \cdot u_j)\right] + \frac{\partial}{\partial x_i}\left[\rho(e+\frac{1}{2}u_j \cdot u_j)u_i\right] - \frac{\partial}{\partial x_i}(u_j \cdot \sigma_{ij}) - \rho u_j f_j + \frac{\partial q_j}{\partial x_j} = 0 \quad (2.B.14)$$

Equations 2.B.7, 2.B.11, and 2.B.14 are often put in a compact vector form. This form of the governing equations is shown in equations 2.B.15 through 2.B.20.

$$\frac{\partial Q}{\partial t} + \frac{\partial F_1}{\partial x_1} + \frac{\partial F_2}{\partial x_2} + \frac{\partial F_3}{\partial x_3} + H = 0 \quad (2.B.15)$$

where

$$Q = \begin{bmatrix} \rho \\ \rho u_1 \\ \rho u_2 \\ \rho u_3 \\ \rho e_t \end{bmatrix} \quad (2.B.16)$$

$$F_1 = \begin{bmatrix} \rho u_1 \\ \rho u_1 u_1 - \sigma_{11} \\ \rho u_1 u_2 - \sigma_{12} \\ \rho u_1 u_3 - \sigma_{13} \\ \rho u_1 e_t - (u_1\sigma_{11} + u_2\sigma_{12} + u_3\sigma_{13}) + q_1 \end{bmatrix} \quad (2.B.17)$$

$$F_2 = \begin{bmatrix} \rho u_2 \\ \rho u_1 u_2 - \sigma_{21} \\ \rho u_2 u_2 - \sigma_{22} \\ \rho u_2 u_3 - \sigma_{23} \\ \rho u_2 e_t - (u_1\sigma_{21} + u_2\sigma_{22} + u_3\sigma_{23}) + q_2 \end{bmatrix} \quad (2.B.18)$$

$$F_3=\begin{bmatrix} \rho u_3 \\ \rho u_1 u_3-\sigma_{31} \\ \rho u_2 u_3-\sigma_{32} \\ \rho u_3 u_3-\sigma_{33} \\ \rho u_3 e_t-(u_1\sigma_{31}+u_2\sigma_{32}+u_3\sigma_{33})+q_3 \end{bmatrix} \tag{2.B.19}$$

$$H=\begin{bmatrix} 0 \\ \rho f_1 \\ \rho f_2 \\ \rho f_3 \\ \rho(f_1u_1+f_2u_2+f_3u_3) \end{bmatrix} \tag{2.B.20}$$

Notice, the first row represents components taken from the conservation of mass equation. Row two, three, and four are the first, second, and third components of the momentum equation. The last row has components from the conservation of energy equation.

At this point, there are five equations with seventeen unknowns: ρ , e , u_j (3 components), q_j (3 components), and σ_{ij} (9 components). There are actually only fourteen unknowns since there is symmetry within the stress tensor σ_{ij} (6 unique components). To close off the system of equations, we include the pressure and internal energy equations of state. Both equations are a function of density and temperature.

$$p=p(\rho,T) \tag{2.B.21}$$

$$e=e(\rho,T) \tag{2.B.22}$$

This brings the total number of equations up to seven. The constitutive equations, including stress tensor σ_{ij} and heat flux q_j , are used to completely close the system of equations. Shown below is a more complete equation for the stress tensor σ_{ij}

$$\sigma_{ij}=-p\delta_{ij}+\lambda\delta_{ij}\frac{\partial u_k}{\partial x_k}+\mu\left(\frac{\partial u_i}{\partial x_j}+\frac{\partial u_j}{\partial x_i}\right) \tag{2.B.23}$$

Equation 2.B.23 can be written in a two part form.

$$\sigma_{ij} = -p\delta_{ij} + \tau_{ij} \tag{2.B.24}$$

$$\tau_{ij} = \lambda \delta_{ij} \frac{\partial u_k}{\partial x_k} + \mu \left(\frac{\partial u_i}{\partial x_j} + \frac{\partial u_j}{\partial x_i} \right) \tag{2.B.25}$$

where

p = static pressure

δ_{ij} = Kronecker delta

μ = absolute viscosity

λ = second coefficient of viscosity

K = bulk viscosity

The Kronecker delta has the following definition.

$$\delta_{ij} = \begin{cases} 1 & i = j \\ 0 & i \neq j \end{cases} \tag{2.B.26}$$

The bulk viscosity equation provides a relation between absolute viscosity and the second coefficient of viscosity.

$$K = \lambda + \frac{2}{3}\mu = 0 \tag{2.B.27}$$

From equation 2.B.25, the following relationship is true for the case of monatomic gases.

$$\lambda = -\frac{2}{3}\mu \tag{2.B.28}$$

Fourier's Law of Heat Conduction is used to close out the system of equations

$$q_j = -\kappa \frac{\partial T}{\partial x_j} \tag{2.B.29}$$

where

T = static temperature

κ = thermal conductivity

Temperature can be calculated using the perfect gas equation

$$a^2 = \gamma RT = \gamma \frac{p}{\rho} \tag{2.B.30}$$

where

a = sonic velocity

γ = ratio of specific heats

R = ideal gas constant

Recall, γ is the ratio of specific heats

$$\gamma = \frac{c_p}{c_v} \tag{2.B.31}$$

where

c_p = heat capacity at constant pressure

c_v = heat capacity at constant volume

Heat capacity for constant pressure and constant volume can be calculated using the following formulas.

$$c_p = \frac{\gamma R}{\gamma - 1} \tag{2.B.32}$$

$$c_v = \frac{R}{\gamma - 1} \tag{2.B.33}$$

C. The Non-Dimensionalization of the Variables

The next step is to non-dimensionalize the variables of the conservation equations. Let a "hatted" quantity represent a non-dimensional variable. Let ∞ represent a reference quantity. Immediately following are some of the parameters and identities used in the non-dimensionalization process.

$$\hat{t} = t\frac{a_\infty}{L} \qquad \hat{x}_j = \frac{x_j}{L} \qquad \hat{\rho} = \frac{\rho}{\rho_\infty} \qquad \hat{u}_j = \frac{u_j}{a_\infty} \qquad \hat{e}_t = \frac{e_t}{a_\infty^2}$$

$$\hat{f}_j = \frac{L}{a_\infty^2} f_j \qquad \hat{\mu} = \frac{\mu}{\mu_\infty} \qquad \hat{\lambda} = \frac{\lambda}{\mu_\infty} \qquad Re'_\infty = \frac{\rho_\infty a_\infty L}{\mu_\infty} \tag{2.C.1}$$

Before beginning, it is key to note the following

$$\frac{d}{dt}() = \frac{d\hat{t}}{dt}\frac{d}{d\hat{t}}() = \frac{a_\infty}{L}\frac{d}{d\hat{t}}() \tag{2.C.2}$$

where

L = reference length

Notice, the last identity shown in 2.C.1 is Reynolds number. Note, this Reynolds number is calculated using the reference speed of sound. Another form of Reynolds number is shown below

$$Re_\infty = \frac{\rho_\infty U_\infty L}{\mu_\infty} \tag{2.C.3}$$

where U_∞ is a specified reference velocity. The two Reynolds numbers are related in the following way.

$$Re_\infty = M_\infty Re'_\infty \tag{2.C.4}$$

M_∞ represents a reference Mach number.

$$M_\infty = \frac{U_\infty}{a_\infty} \tag{2.C.5}$$

Along with Reynolds number, there is another common dimensionless number known as Prandtl number.

$$Pr = \frac{\mu c_p}{\kappa} \tag{2.C.6}$$

To begin the non-dimensionalization process, we start with the stress tensor equation as seen in equation 2.B.24.

$$\sigma_{ij} = -p\,\delta_{ij} + \tau_{ij} \tag{2.C.7}$$

Letting the following be true,

$$\hat{\sigma}_{ij} = \frac{\sigma_{ij}}{\rho_\infty a_\infty^2} \tag{2.C.8}$$

The stress tensor equation becomes

$$\hat{\sigma}_{ij} = \frac{\sigma_{ij}}{\rho_\infty a_\infty^2} = \frac{-p}{\rho_\infty a_\infty^2}\,\delta_{ij} + \frac{\tau_{ij}}{\rho_\infty a_\infty^2} \tag{2.C.9}$$

From equation 2.C.9, we have defined two more identities to add to the equations in 2.C.1.

$$\hat{p} = \frac{p}{\rho_\infty a_\infty^2} \qquad \hat{\tau}_{ij} = \frac{\tau_{ij}}{\rho_\infty a_\infty^2} \tag{2.C.10}$$

The two equations shown above are used to simplify equation 2.C.9, producing the non-dimensional form of the stress tensor equation.

$$\hat{\sigma}_{ij} = -\hat{p}\,\delta_{ij} + \hat{\tau}_{ij} \tag{2.C.11}$$

To non-dimensionalize the second part of the stress tensor equation, we begin with equation 2.B.25.

$$\tau_{ij} = \lambda\,\delta_{ij}\frac{\partial u_k}{\partial x_k} + \mu\left(\frac{\partial u_i}{\partial x_j} + \frac{\partial u_j}{\partial x_i}\right) \tag{2.C.12}$$

Recall the following identities from the parameters listed in 2.C.1. Note, the equations have been recomposed to better visualize the substitutions being made.

$$\mu = \hat{\mu}\,\mu_\infty \qquad \lambda = \hat{\lambda}\,\mu_\infty \qquad x_j = \hat{x}_j L \qquad u_j = \hat{u}_j a_\infty \tag{2.C.13}$$

Inserting the identities shown in 2.C.13, we get the following.

$$\hat{\tau}_{ij} = \frac{\tau_{ij}}{\rho_\infty a_\infty^2} = \delta_{ij}\frac{\hat{\lambda}\,\mu_\infty}{\rho_\infty a_\infty^2}\frac{\partial(\hat{u}_k a_\infty)}{\partial(\hat{x}_k L)} + \frac{\hat{\mu}\,\mu_\infty}{\rho_\infty a_\infty^2}\left[\frac{\partial(\hat{u}_i a_\infty)}{\partial(\hat{x}_j L)} + \frac{\partial(\hat{u}_j a_\infty)}{\partial(\hat{x}_i L)}\right] \tag{2.C.14}$$

Keep in mind, the reference values are constants and can be brought out of partial differentiations. Rearranging appropriately, equation 2.C.14 becomes

$$\hat{\tau}_{ij} = \delta_{ij}\frac{\hat{\lambda}}{\frac{\rho_\infty a_\infty L}{\mu_\infty}}\frac{\partial \hat{u}_k}{\partial \hat{x}_k} + \frac{\hat{\mu}}{\frac{\rho_\infty a_\infty L}{\mu_\infty}}\left(\frac{\partial \hat{u}_i}{\partial \hat{x}_j} + \frac{\partial \hat{u}_j}{\partial \hat{x}_i}\right) \tag{2.C.15}$$

Notice the common denominator of the first and second term is in fact Reynolds number. Bringing this term out to the front, we arrive at the complete non-dimensional form of the stress tensor equation

$$\hat{\sigma}_{ij} = -\hat{p}\delta_{ij} + \hat{\tau}_{ij} \tag{2.C.16}$$

where

$$\hat{\tau}_{ij} = \frac{1}{Re'_\infty}\left[\delta_{ij}\hat{\lambda}\frac{\partial \hat{u}_k}{\partial \hat{x}_k} + \hat{\mu}\left(\frac{\partial \hat{u}_i}{\partial \hat{x}_j} + \frac{\partial \hat{u}_j}{\partial \hat{x}_i}\right)\right] \tag{2.C.17}$$

Having identities for pressure (2.C.10) and density (2.C.1), we can begin the non-dimensional process for the speed of sound equation (2.B.30).

$$a^2 = \gamma\frac{p}{\rho} \tag{2.C.18}$$

Below are the rearranged identities for pressure and density from equations 2.C.10 and 2.C.1, respectively.

$$p = \hat{p}\,\rho_\infty a_\infty^2 \qquad \rho = \hat{\rho}\,\rho_\infty \tag{2.C.19}$$

Remembering that the ratio of specific heats is already non-dimensional, we insert the identities shown in 2.C.19.

$$a^2 = \gamma \frac{\hat{p}\rho_\infty a_\infty^2}{\hat{\rho}\rho_\infty} \tag{2.C.20}$$

Notice that the reference density values cancel. Thus, we non-dimensionalize speed of sound in the following way.

$$\hat{a}^2 = \frac{a^2}{a_\infty^2} \tag{2.C.21}$$

If equation 2.C.21 is true, we can finish deriving the non-dimensional form of equation 2.C.18.

$$\hat{a}^2 = \gamma \frac{\hat{p}}{\hat{\rho}} \tag{2.C.22}$$

Likewise, a non-dimensional expression can be evaluated for temperature since the followings is true.

$$a^2 = \gamma RT \tag{2.C.23}$$

Rearranging to solve for temperature,

$$T = \frac{a^2}{\gamma R} \tag{2.C.24}$$

Inserting our speed of sound identity $a^2 = \hat{a}^2 a_\infty^2$ from equation 2.C.21, we arrive at the following equation.

$$T = \frac{\hat{a}^2 a_\infty^2}{\gamma R} \tag{2.C.25}$$

Let temperature be non-dimensionalized in the following way.

$$\hat{T} = \frac{T}{a_\infty^2} \tag{2.C.26}$$

Using equation 2.C.26, we arrive at the non-dimensional equation for temperature.

$$\hat{T}=\frac{\hat{a}^2}{\gamma R} \tag{2.C.27}$$

We are now prepared to non-dimensionalize the three conservation equations (2.B.7, 2.B.11, and 2.B.14).The non-dimensionalization process of the mass conservation equation starts with equation 2.B.7.

$$\frac{\partial \rho}{\partial t}+\frac{\partial}{\partial x_j}(\rho u_j)=0 \tag{2.C.28}$$

We begin by inserting the following rearranged identities from 2.C.1 into equation 2.C.28.

$$\rho=\hat{\rho}\,\rho_\infty \qquad x_j=\hat{x}_j L \qquad u_j=\hat{u}_j a_\infty \tag{2.C.29}$$

$$\frac{\partial \rho}{\partial t}+\frac{\partial}{\partial x_j}(\rho u_j)=\frac{d\hat{t}}{dt}\frac{\partial}{\partial \hat{t}}(\hat{\rho}\rho_\infty)+\frac{\partial \hat{x}_j}{\partial x_j}\frac{\partial}{\partial \hat{x}_j}(\hat{\rho}\rho_\infty \hat{u}_j a_\infty)=0 \tag{2.C.30}$$

Next, we rearrange the reference variables,

$$\frac{\rho_\infty a_\infty}{L}\frac{\partial \hat{\rho}}{\partial \hat{t}}+\frac{\rho_\infty a_\infty}{L}\frac{\partial}{\partial \hat{x}_j}(\hat{\rho}\hat{u}_j)=0 \tag{2.C.31}$$

Dividing through by the common leading term $\frac{\rho_\infty a_\infty}{L}$, we get the non-dimensional form of the conservation of mass equation.

$$\frac{\partial \hat{\rho}}{\partial \hat{t}}+\frac{\partial}{\partial \hat{x}_j}(\hat{\rho}\hat{u}_j)=0 \tag{2.C.32}$$

Similarly, the same procedure is used to derive the non-dimensional forms of the conservation of momentum (2.C.38) and conservation of energy (2.C.55) equations.

$$\begin{gathered}\frac{\partial}{\partial \hat{t}}(\hat{\rho}\hat{u}_j)+\frac{\partial}{\partial \hat{x}_i}(\hat{\rho}\hat{u}_j\hat{u}_i)+\delta_{ij}\frac{\partial \hat{p}}{\partial x_i} \\ \frac{-1}{Re'_\infty}\frac{\partial}{\partial x_i}\left[\delta_{ij}\hat{\lambda}\frac{\partial \hat{u}_k}{\partial \hat{x}_k}+\hat{\mu}\left(\frac{\partial \hat{u}_i}{\partial \hat{x}_j}+\frac{\partial \hat{u}_j}{\partial \hat{x}_i}\right)\right]-\hat{\rho}\,\hat{f}_j=0\end{gathered} \tag{2.C.38}$$

$$\frac{\partial}{\partial \hat{t}}(\hat{\rho}\,\hat{e}_t)+\frac{\partial}{\partial \hat{x}_i}(\hat{\rho}\,\hat{e}_t\hat{u}_i)+\delta_{ij}\frac{\partial}{\partial \hat{x}_i}(\hat{u}_j\,\hat{p})-(\hat{\rho}\,\hat{u}_j\,\hat{f}_j)$$
$$-\frac{1}{Re'_\infty}\left[\delta_{ij}\hat{\lambda}\frac{\partial \hat{u}_k}{\partial \hat{x}_k}+\hat{\mu}\left(\frac{\partial \hat{u}_i}{\partial \hat{x}_j}+\frac{\partial \hat{u}_j}{\partial \hat{x}_i}\right)\right] \qquad (2.C.55)$$
$$-\frac{1}{Re'_\infty(\gamma-1)}\frac{\partial}{\partial \hat{x}_j}\left[\frac{\hat{\mu}}{Pr}\frac{\partial(\hat{a}^2)}{\partial \hat{x}_j}\right]=0$$

Equations 2.C.28 through 2.C.55 show the step-by-step derivations of the conservation of mass, momentum, and energy equations which are located in Appendix-A.

Now that we have our three governing equations in non-dimensional form (2.C.32, 2.C.38, and 2.C.55), we can now rewrite our conservation equations in conservative vector form, as seen in equations 2.C.56 through 2.C.70. Note, we can now drop the "hats" from the non-dimensional variables with the understanding that all variables are non-dimensional from this point on.

$$\frac{\partial q}{\partial t}+\frac{\partial f}{\partial x_1}+\frac{\partial g}{\partial x_2}+\frac{\partial h}{\partial x_3}=\frac{1}{Re'_\infty}\left[\frac{\partial f^v}{\partial x_1}+\frac{\partial g^v}{\partial x_2}+\frac{\partial h^v}{\partial x_3}\right]+b \qquad (2.C.56)$$

where

$$q=\begin{bmatrix}\rho\\ \rho u_1\\ \rho u_2\\ \rho u_3\\ \rho e_t\end{bmatrix} \qquad (2.C.57)$$

$$f=\begin{bmatrix}\rho u_1\\ \rho u_1^2+p\\ \rho u_1u_2\\ \rho u_1u_3\\ u_1(\rho e_t+p)\end{bmatrix} \qquad (2.C.58)$$

$$g=\begin{bmatrix}\rho u_2\\ \rho u_2 u_1\\ \rho u_2^2+p\\ \rho u_2 u_3\\ u_2(\rho e_t+p)\end{bmatrix} \tag{2.C.59}$$

$$h=\begin{bmatrix}\rho u_3\\ \rho u_3 u_1\\ \rho u_3 u_2+p\\ \rho u_3^2+p\\ u_3(\rho e_t+p)\end{bmatrix} \tag{2.C.60}$$

$$b=\begin{bmatrix}0\\ \rho f_1\\ \rho f_2\\ \rho f_3\\ \rho(f_1 u_1+f_2 u_2+f_3 u_3)\end{bmatrix} \tag{2.C.61}$$

$$f^v=\begin{bmatrix}0\\ \tau_{11}\\ \tau_{12}\\ \tau_{13}\\ u_1\tau_{11}+u_2\tau_{21}+u_3\tau_{31}+\dfrac{1}{\gamma-1}\dfrac{\mu}{Pr}\dfrac{\partial a^2}{\partial x_1}\end{bmatrix} \tag{2.C.62}$$

$$g^v=\begin{bmatrix}0\\ \tau_{21}\\ \tau_{22}\\ \tau_{23}\\ u_1\tau_{12}+u_2\tau_{22}+u_3\tau_{32}+\dfrac{1}{\gamma-1}\dfrac{\mu}{Pr}\dfrac{\partial a^2}{\partial x_2}\end{bmatrix} \tag{2.C.63}$$

$$h^v = \begin{bmatrix} 0 \\ \tau_{31} \\ \tau_{32} \\ \tau_{33} \\ u_1\tau_{13} + u_2\tau_{23} + u_3\tau_{33} + \dfrac{1}{\gamma - 1}\dfrac{\mu}{Pr}\dfrac{\partial a^2}{\partial x_3} \end{bmatrix} \tag{2.C.64}$$

$$\tau_{11} = (\lambda + 2\mu)\frac{\partial u_1}{\partial x_1} + \lambda\left(\frac{\partial u_2}{\partial x_2} + \frac{\partial u_3}{\partial x_3}\right) \tag{2.C.65}$$

$$\tau_{22} = (\lambda + 2\mu)\frac{\partial u_2}{\partial x_2} + \lambda\left(\frac{\partial u_1}{\partial x_1} + \frac{\partial u_3}{\partial x_3}\right) \tag{2.C.66}$$

$$\tau_{33} = (\lambda + 2\mu)\frac{\partial u_3}{\partial x_3} + \lambda\left(\frac{\partial u_1}{\partial x_1} + \frac{\partial u_2}{\partial x_2}\right) \tag{2.C.67}$$

$$\tau_{21} = \tau_{12} = \mu\left(\frac{\partial u_2}{\partial x_1} + \frac{\partial u_1}{\partial x_2}\right) \tag{2.C.68}$$

$$\tau_{31} = \tau_{13} = \mu\left(\frac{\partial u_3}{\partial x_1} + \frac{\partial u_1}{\partial x_3}\right) \tag{2.C.69}$$

$$\tau_{32} = \tau_{23} = \mu\left(\frac{\partial u_3}{\partial x_2} + \frac{\partial u_2}{\partial x_3}\right) \tag{2.C.70}$$

D. Coordinate Transformation from Cartesian Coordinates to General Curvilinear Coordinates

In Computational Fluid Dynamics (CFD), the use of structured and unstructured grids sometimes require a coordinate transformation. The chain rule of differentiation is used to convert Cartesian Coordinates to general Curvilinear Coordinates. To understand the chain rule, let us say we have a function f which is dependent on the four independent variables x , y , z ,and t .

$$f = f(x, y, z, t) \tag{2.D.1}$$

The independent variables x , y , z ,and t are functions with respect to the general Curvilinear coordinates ξ , η , ζ , and τ .

$$\begin{aligned} x &= x(\xi,\eta,\zeta,\tau) \\ y &= y(\xi,\eta,\zeta,\tau) \\ z &= z(\xi,\eta,\zeta,\tau) \\ t &= t(\tau) \end{aligned} \tag{2.D.2}$$

Note that the time coordinate, t ,is only a function of the transformed time-like coordinate τ . As a result, function f can be written in the following way.

$$f = f\left[x(\xi,\eta,\zeta,\tau), y(\xi,\eta,\zeta,\tau), z(\xi,\eta,\zeta,\tau), t(\tau)\right] \tag{2.D.3}$$

The Curvilinear coordinates can inversely be written in terms of Cartesian coordinates.

$$\begin{aligned} \xi &= \xi(x, y, z, t) \\ \eta &= \eta(x, y, z, t) \\ \zeta &= \zeta(x, y, z, t) \\ \tau &= \tau(t) \end{aligned} \tag{2.D.4}$$

Thus, function f can be reasoned to be directly dependent on the Curvilinear coordinates.

$$f\left[x(\xi,\eta,\zeta,\tau), y(\xi,\eta,\zeta,\tau), z(\xi,\eta,\zeta,\tau), t(\tau)\right] \equiv F(\xi,\eta,\zeta,\tau) \tag{2.D.5}$$

Similarly

$$f = F(\xi,\eta,\zeta,\tau) \tag{2.D.6}$$

The chain rule can now be written for any partial derivative of function f .

$$\frac{\partial f}{\partial t} = \left(\frac{\partial x}{\partial t}\right) \cdot \left(\frac{\partial f}{\partial x}\right) \tag{2.D.7}$$

Since function f (written in Cartesian coordinates) is equivalent to function F (written in Curvilinear coordinates), the chain rule can take the following form.

$$\frac{\partial f}{\partial t} = \left(\frac{\partial \xi}{\partial t}\right) \cdot \left(\frac{\partial F}{\partial \xi}\right) \tag{2.D.8}$$

Subscripts are used to simplify partial derivative notation.

$$\left(\frac{\partial \xi}{\partial t}\right)=\xi_t \tag{2.D.9}$$

Any function in Cartesian coordinates can be transformed into Curvilinear coordinates using equations 2.D.10 through 2.D.13. Note, the f and F scripts are dropped from the equations since the transformation equations apply to any function having independent variables x , y , z ,and t .

$$\frac{\partial}{\partial t}=\xi_t\left(\frac{\partial}{\partial \xi}\right)+\eta_t\left(\frac{\partial}{\partial \eta}\right)+\zeta_t\left(\frac{\partial}{\partial \zeta}\right)+\tau_t\left(\frac{\partial}{\partial \tau}\right) \tag{2.D.10}$$

$$\frac{\partial}{\partial x}=\xi_x\left(\frac{\partial}{\partial \xi}\right)+\eta_x\left(\frac{\partial}{\partial \eta}\right)+\zeta_x\left(\frac{\partial}{\partial \zeta}\right) \tag{2.D.11}$$

$$\frac{\partial}{\partial y}=\xi_y\left(\frac{\partial}{\partial \xi}\right)+\eta_y\left(\frac{\partial}{\partial \eta}\right)+\zeta_y\left(\frac{\partial}{\partial \zeta}\right) \tag{2.D.12}$$

$$\frac{\partial}{\partial z}=\xi_z\left(\frac{\partial}{\partial \xi}\right)+\eta_z\left(\frac{\partial}{\partial \eta}\right)+\zeta_z\left(\frac{\partial}{\partial \zeta}\right) \tag{2.D.13}$$

Our time-like variable τ is not dependent on position variables x , y ,or z .

$$\tau_x=\tau_y=\tau_z=0 \tag{2.D.14}$$

Since the independent Cartesian variables x , y , z ,and t are dependent on the Curvilinear variables ξ , η , ζ ,and τ , equations 2.D.10 through 2.D.13 can be rewritten accordingly.

$$\frac{\partial}{\partial \tau}=x_\tau\left(\frac{\partial}{\partial x}\right)+y_\tau\left(\frac{\partial}{\partial y}\right)+z_\tau\left(\frac{\partial}{\partial z}\right)+t_\tau\left(\frac{\partial}{\partial \tau}\right) \tag{2.D.15}$$

$$\frac{\partial}{\partial \xi}=x_\xi\left(\frac{\partial}{\partial x}\right)+y_\xi\left(\frac{\partial}{\partial y}\right)+z_\xi\left(\frac{\partial}{\partial z}\right) \tag{2.D.16}$$

$$\frac{\partial}{\partial \eta}=x_\eta\left(\frac{\partial}{\partial x}\right)+y_\eta\left(\frac{\partial}{\partial y}\right)+z_\eta\left(\frac{\partial}{\partial z}\right) \tag{2.D.17}$$

$$\frac{\partial}{\partial \zeta}=x_\zeta\left(\frac{\partial}{\partial x}\right)+y_\zeta\left(\frac{\partial}{\partial y}\right)+z_\zeta\left(\frac{\partial}{\partial z}\right) \tag{2.D.18}$$

So far, we have just been rewriting the equations in terms of the different coordinate variables. We need to solve for the Cartesian derivatives in terms of the curvilinear derivatives. To do so, we can write equations 2.D.15 through 2.D.18 in $b = A\,x$ matrix form.

$$\begin{bmatrix} \frac{\partial}{\partial \tau} \\ \frac{\partial}{\partial \xi} \\ \frac{\partial}{\partial \eta} \\ \frac{\partial}{\partial \zeta} \end{bmatrix} = \begin{bmatrix} t_\tau & x_\tau & y_\tau & z_\tau \\ 0 & x_\xi & y_\xi & z_\xi \\ 0 & x_\eta & y_\eta & z_\eta \\ 0 & x_\zeta & y_\zeta & z_\zeta \end{bmatrix} \begin{bmatrix} \frac{\partial}{\partial t} \\ \frac{\partial}{\partial x} \\ \frac{\partial}{\partial y} \\ \frac{\partial}{\partial z} \end{bmatrix} \tag{2.D.19}$$

To solve the Cartesian derivatives, we need to calculated the inverse of matrix A . We begin by calculating the determinant of A .

$$det\ A = t_\tau \begin{pmatrix} x_\xi & y_\xi & z_\xi \\ x_\eta & y_\eta & z_\eta \\ x_\zeta & y_\zeta & z_\zeta \end{pmatrix} \tag{2.D.20}$$

$$J' = det\ A = t_\tau \left[x_\xi (y_\eta z_\zeta - y_\zeta z_\eta) + y_\xi (z_\eta x_\zeta - z_\zeta x_\eta) + z_\xi (x_\eta y_\zeta - x_\zeta y_\eta) \right] \tag{2.D.21}$$

$$J' = det\ A = t_\tau J = t_\tau \frac{\partial(x, y, z)}{\partial(\xi, \eta, \zeta)} \tag{2.D.22}$$

where J or $\frac{\partial(x, y, z)}{\partial(\xi, \eta, \zeta)}$ is called the Jacobian of the inverse coordinate transformation. Recall, the inverse matrix is calculated by dividing the adjugate matrix by the determinant.

$$A^{-1} = \frac{1}{det\ A}\, adj\ (A) = \frac{1}{t_\tau J}\, adj\ (A)$$

Immediately following is the arithmetic for calculating the adjugate matrix, $adj(A)$, from the A matrix in equation 2.D.19.

$$adj\,(A)=\begin{bmatrix}
\begin{vmatrix} x_\xi & y_\xi & z_\xi \\ x_\eta & y_\eta & z_\eta \\ x_\zeta & y_\zeta & z_\zeta \end{vmatrix} & -\begin{vmatrix} x_\tau & y_\tau & z_\tau \\ x_\eta & y_\eta & z_\eta \\ x_\zeta & y_\zeta & z_\zeta \end{vmatrix} & \begin{vmatrix} x_\tau & y_\tau & z_\tau \\ x_\xi & y_\xi & z_\xi \\ x_\zeta & y_\zeta & z_\zeta \end{vmatrix} & -\begin{vmatrix} x_\tau & y_\tau & z_\tau \\ x_\xi & y_\xi & z_\xi \\ x_\eta & y_\eta & z_\eta \end{vmatrix} \\
-\begin{vmatrix} 0 & y_\xi & z_\xi \\ 0 & y_\eta & z_\eta \\ 0 & y_\zeta & z_\zeta \end{vmatrix} & \begin{vmatrix} t_\tau & y_\tau & z_\tau \\ 0 & y_\eta & z_\eta \\ 0 & y_\zeta & z_\zeta \end{vmatrix} & -\begin{vmatrix} t_\tau & y_\tau & z_\tau \\ 0 & y_\xi & z_\xi \\ 0 & y_\zeta & z_\zeta \end{vmatrix} & \begin{vmatrix} t_\tau & y_\tau & z_\tau \\ 0 & y_\xi & z_\xi \\ 0 & y_\eta & z_\eta \end{vmatrix} \\
\begin{vmatrix} 0 & x_\xi & z_\xi \\ 0 & x_\eta & z_\eta \\ 0 & x_\zeta & z_\zeta \end{vmatrix} & -\begin{vmatrix} t_\tau & x_\tau & z_\tau \\ 0 & x_\eta & z_\eta \\ 0 & x_\zeta & z_\zeta \end{vmatrix} & \begin{vmatrix} t_\tau & x_\tau & z_\tau \\ 0 & x_\xi & z_\xi \\ 0 & x_\zeta & z_\zeta \end{vmatrix} & -\begin{vmatrix} t_\tau & x_\tau & z_\tau \\ 0 & x_\xi & z_\xi \\ 0 & x_\eta & z_\eta \end{vmatrix} \\
-\begin{vmatrix} 0 & x_\xi & y_\xi \\ 0 & x_\eta & y_\eta \\ 0 & x_\zeta & y_\zeta \end{vmatrix} & \begin{vmatrix} t_\tau & x_\tau & y_\tau \\ 0 & x_\eta & y_\eta \\ 0 & x_\zeta & y_\zeta \end{vmatrix} & -\begin{vmatrix} t_\tau & x_\tau & y_\tau \\ 0 & x_\xi & y_\xi \\ 0 & x_\zeta & y_\zeta \end{vmatrix} & \begin{vmatrix} t_\tau & x_\tau & y_\tau \\ 0 & x_\xi & y_\xi \\ 0 & x_\eta & y_\eta \end{vmatrix}
\end{bmatrix}$$

(2.D.23)

$$adj\,(A)=\begin{bmatrix}
J & \begin{pmatrix} -x_\tau\left[y_\eta z_\zeta - y_\zeta z_\eta\right] \\ -y_\tau\left[z_\eta x_\zeta - z_\zeta x_\eta\right] \\ -z_\tau\left[x_\eta y_\zeta - x_\zeta y_\eta\right] \end{pmatrix} & \begin{pmatrix} x_\tau\left[y_\xi z_\zeta - y_\zeta z_\xi\right] \\ +y_\tau\left[z_\xi x_\zeta - z_\zeta x_\xi\right] \\ +z_\tau\left[x_\xi y_\zeta - x_\zeta y_\xi\right] \end{pmatrix} & \begin{pmatrix} -x_\tau\left[y_\xi z_\eta - y_\eta z_\xi\right] \\ -y_\tau\left[z_\xi x_\eta - z_\eta x_\xi\right] \\ -z_\tau\left[x_\xi y_\eta - x_\eta y_\xi\right] \end{pmatrix} \\
0 & t_\tau\left(y_\eta z_\zeta - y_\zeta z_\eta\right) & -t_\tau\left(y_\xi z_\zeta - y_\zeta z_\xi\right) & t_\tau\left(y_\xi z_\eta - y_\eta z_\xi\right) \\
0 & -t_\tau\left(z_\zeta x_\eta - z_\eta x_\zeta\right) & t_\tau\left(z_\zeta x_\xi - z_\xi x_\zeta\right) & -t_\tau\left(z_\eta x_\xi - z_\xi x_\eta\right) \\
0 & t_\tau\left(x_\eta y_\zeta - x_\zeta y_\eta\right) & -t_\tau\left(x_\xi y_\zeta - x_\zeta y_\xi\right) & t_\tau\left(x_\xi y_\eta - x_\eta y_\xi\right)
\end{bmatrix}$$

(2.D.24)

Notice, we can reverse the order of the partial derivatives about the minus operator to get the whole expression in positive or negative terms .

$$\begin{pmatrix} x_\tau\left[y_\xi z_\zeta - y_\zeta z_\xi\right] \\ +y_\tau\left[z_\xi x_\zeta - z_\zeta x_\xi\right] \\ +z_\tau\left[x_\xi y_\zeta - x_\zeta y_\xi\right] \end{pmatrix} = \begin{pmatrix} -x_\tau\left[y_\zeta z_\xi - y_\xi z_\zeta\right] \\ -y_\tau\left[z_\zeta x_\xi - z_\xi x_\zeta\right] \\ -z_\tau\left[x_\zeta y_\xi - x_\xi y_\zeta\right] \end{pmatrix}$$

$$-t_\tau\left(y_\xi z_\zeta - y_\zeta z_\xi\right) = t_\tau\left(y_\zeta z_\xi - y_\xi z_\zeta\right)$$

Repeating this algebra, allow us to obtain a consistent subscript order for each column.

$$adj\,(A)=\begin{bmatrix} J & \begin{pmatrix}-x_\tau\left[y_\eta z_\zeta - y_\zeta z_\eta\right]\\ -y_\tau\left[z_\eta x_\zeta - z_\zeta x_\eta\right]\\ -z_\tau\left[x_\eta y_\zeta - x_\zeta y_\eta\right]\end{pmatrix} & \begin{pmatrix}-x_\tau\left[y_\zeta z_\xi - y_\xi z_\zeta\right]\\ -y_\tau\left[z_\zeta x_\xi - z_\xi x_\zeta\right]\\ -z_\tau\left[x_\zeta y_\xi - x_\xi y_\zeta\right]\end{pmatrix} & \begin{pmatrix}-x_\tau\left[y_\xi z_\eta - y_\eta z_\xi\right]\\ -y_\tau\left[z_\xi x_\eta - z_\eta x_\xi\right]\\ -z_\tau\left[x_\xi y_\eta - x_\eta y_\xi\right]\end{pmatrix} \\ 0 & t_\tau\left(y_\eta z_\zeta - y_\zeta z_\eta\right) & t_\tau\left(y_\zeta z_\xi - y_\xi z_\zeta\right) & t_\tau\left(y_\xi z_\eta - y_\eta z_\xi\right) \\ 0 & t_\tau\left(z_\eta x_\zeta - z_\zeta x_\eta\right) & t_\tau\left(z_\zeta x_\xi - z_\xi x_\zeta\right) & t_\tau\left(z_\xi x_\eta - z_\eta x_\xi\right) \\ 0 & t_\tau\left(x_\eta y_\zeta - x_\zeta y_\eta\right) & t_\tau\left(x_\zeta y_\xi - x_\xi y_\zeta\right) & t_\tau\left(x_\xi y_\eta - x_\eta y_\xi\right) \end{bmatrix}$$

(2.D.25)

Notice, column three in 2.D.25 has the consistent subscript order of $\zeta\xi$ $\xi\zeta$ opposed to the varying order as seen in column three of 2.D.24. Now that we have all the pieces for calculating inverse matrix A , we rewrite our equation in $x=A^{-1}b$ form.

$$\begin{bmatrix}\frac{\partial}{\partial t}\\ \frac{\partial}{\partial x}\\ \frac{\partial}{\partial y}\\ \frac{\partial}{\partial z}\end{bmatrix}=\frac{1}{t_\tau J}\begin{bmatrix} J & \begin{pmatrix}-x_\tau\left[y_\eta z_\zeta - y_\zeta z_\eta\right]\\ -y_\tau\left[z_\eta x_\zeta - z_\zeta x_\eta\right]\\ -z_\tau\left[x_\eta y_\zeta - x_\zeta y_\eta\right]\end{pmatrix} & \begin{pmatrix}-x_\tau\left[y_\zeta z_\xi - y_\xi z_\zeta\right]\\ -y_\tau\left[z_\zeta x_\xi - z_\xi x_\zeta\right]\\ -z_\tau\left[x_\zeta y_\xi - x_\xi y_\zeta\right]\end{pmatrix} & \begin{pmatrix}-x_\tau\left[y_\xi z_\eta - y_\eta z_\xi\right]\\ -y_\tau\left[z_\xi x_\eta - z_\eta x_\xi\right]\\ -z_\tau\left[x_\xi y_\eta - x_\eta y_\xi\right]\end{pmatrix} \\ 0 & t_\tau\left(y_\eta z_\zeta - y_\zeta z_\eta\right) & t_\tau\left(y_\zeta z_\xi - y_\xi z_\zeta\right) & t_\tau\left(y_\xi z_\eta - y_\eta z_\xi\right) \\ 0 & t_\tau\left(z_\eta x_\zeta - z_\zeta x_\eta\right) & t_\tau\left(z_\zeta x_\xi - z_\xi x_\zeta\right) & t_\tau\left(z_\xi x_\eta - z_\eta x_\xi\right) \\ 0 & t_\tau\left(x_\eta y_\zeta - x_\zeta y_\eta\right) & t_\tau\left(x_\zeta y_\xi - x_\xi y_\zeta\right) & t_\tau\left(x_\xi y_\eta - x_\eta y_\xi\right) \end{bmatrix}\begin{bmatrix}\frac{\partial}{\partial \tau}\\ \frac{\partial}{\partial \xi}\\ \frac{\partial}{\partial \eta}\\ \frac{\partial}{\partial \zeta}\end{bmatrix}$$

(2.D.26)

Our original transformation equations 2.D.10 through 2.D.13 can be rewritten in the following matrix form.

$$\begin{bmatrix}\frac{\partial}{\partial t}\\ \frac{\partial}{\partial x}\\ \frac{\partial}{\partial y}\\ \frac{\partial}{\partial z}\end{bmatrix}=\begin{bmatrix}\frac{\partial \tau}{\partial t} & \frac{\partial \xi}{\partial t} & \frac{\partial \eta}{\partial t} & \frac{\partial \zeta}{\partial t}\\ 0 & \frac{\partial \xi}{\partial x} & \frac{\partial \eta}{\partial x} & \frac{\partial \zeta}{\partial x}\\ 0 & \frac{\partial \xi}{\partial y} & \frac{\partial \eta}{\partial y} & \frac{\partial \zeta}{\partial y}\\ 0 & \frac{\partial \xi}{\partial z} & \frac{\partial \eta}{\partial z} & \frac{\partial \zeta}{\partial z}\end{bmatrix}\begin{bmatrix}\frac{\partial}{\partial \tau}\\ \frac{\partial}{\partial \xi}\\ \frac{\partial}{\partial \eta}\\ \frac{\partial}{\partial \zeta}\end{bmatrix} \qquad (2.D.27)$$

To solve for the partial derivatives, we just have to make one to one comparisons between the four by four matrices in 2.D.26 and 2.D.27.

$$\tau_t = \frac{1}{t_\tau} \tag{2.D.28}$$

$$\xi_\tau = \frac{\tau_t}{J}\left[-x_\tau\left(y_\eta z_\zeta - y_\zeta z_\eta\right) - y_\tau\left(z_\eta x_\zeta - z_\zeta x_\eta\right) - z_\tau\left(x_\eta y_\zeta - x_\zeta y_\eta\right)\right] \tag{2.D.29}$$

$$\eta_\tau = \frac{\tau_t}{J}\left[-x_\tau\left(y_\zeta z_\xi - y_\xi z_\zeta\right) - y_\tau\left(z_\zeta x_\xi - z_\xi x_\zeta\right) - z_\tau\left(x_\zeta y_\xi - x_\xi y_\zeta\right)\right] \tag{2.D.30}$$

$$\zeta_\tau = \frac{\tau_t}{J}\left[-x_\tau\left(y_\xi z_\eta - y_\eta z_\xi\right) - y_\tau\left(z_\xi x_\eta - z_\eta x_\xi\right) - z_\tau\left(x_\xi y_\eta - x_\eta y_\xi\right)\right] \tag{2.D.31}$$

$$\xi_x = \frac{1}{J}\left(y_\eta z_\zeta - y_\zeta z_\eta\right) \tag{2.D.32}$$

$$\eta_x = \frac{1}{J}\left(y_\zeta z_\xi - y_\xi z_\zeta\right) \tag{2.D.33}$$

$$\zeta_x = \frac{1}{J}\left(y_\xi z_\eta - y_\eta z_\xi\right) \tag{2.D.34}$$

$$\xi_y = \frac{1}{J}\left(z_\eta x_\zeta - z_\zeta x_\eta\right) \tag{2.D.35}$$

$$\eta_y = \frac{1}{J}\left(z_\zeta x_\xi - z_\xi x_\zeta\right) \tag{2.D.36}$$

$$\zeta_y = \frac{1}{J}\left(z_\xi x_\eta - z_\eta x_\xi\right) \tag{2.D.37}$$

$$\xi_z = \frac{1}{J}\left(x_\eta y_\zeta - x_\zeta y_\eta\right) \tag{2.D.38}$$

$$\eta_z = \frac{1}{J}\left(x_\zeta y_\xi - x_\xi y_\zeta\right) \tag{2.D.39}$$

$$\zeta_z = \frac{1}{J}\left(x_\xi y_\eta - x_\eta y_\xi\right) \tag{2.D.40}$$

Now to apply equations 2.D.10 through 2.D.13 to the conservative vector form of our governing equations as seen in equation 2.C.57.

$$\frac{\partial q}{\partial t}+\frac{\partial f}{\partial x_1}+\frac{\partial g}{\partial x_2}+\frac{\partial h}{\partial x_3}=\frac{1}{Re'_\infty}\left[\frac{\partial f^v}{\partial x_1}+\frac{\partial g^v}{\partial x_2}+\frac{\partial h^v}{\partial x_3}\right]+b \qquad (2.D.41)$$

Shown below is the subscript number notation.

$$x_1=x, \xi_1=\xi$$
$$x_2=y, \xi_2=\eta$$
$$x_3=z, \xi_3=\zeta$$

Applying equations 2.D.10 through 2.D.13 to their respective partial derivatives, we have the expanded expression for equation 2.D.41.

$$\frac{\partial q}{\partial t}=\xi_t\frac{\partial q}{\partial \xi}+\eta_t\frac{\partial q}{\partial \eta}+\zeta_t\frac{\partial q}{\partial \zeta}+\tau_t\frac{\partial q}{\partial \tau} \qquad (2.D.42)$$

$$\frac{\partial f}{\partial x}=\xi_x\frac{\partial f}{\partial \xi}+\eta_x\frac{\partial f}{\partial \eta}+\zeta_x\frac{\partial f}{\partial \zeta} \qquad (2.D.43)$$

$$\frac{\partial g}{\partial y}=\xi_y\frac{\partial g}{\partial \xi}+\eta_y\frac{\partial g}{\partial \eta}+\zeta_y\frac{\partial g}{\partial \zeta} \qquad (2.D.44)$$

$$\frac{\partial h}{\partial z}=\xi_z\frac{\partial h}{\partial \xi}+\eta_z\frac{\partial h}{\partial \eta}+\zeta_z\frac{\partial h}{\partial \zeta} \qquad (2.D.45)$$

$$\frac{\partial f^v}{\partial x}=\xi_x\frac{\partial f^v}{\partial \xi}+\eta_x\frac{\partial f^v}{\partial \eta}+\zeta_x\frac{\partial f^v}{\partial \zeta} \qquad (2.D.46)$$

$$\frac{\partial g^v}{\partial y}=\xi_y\frac{\partial g^v}{\partial \xi}+\eta_y\frac{\partial g^v}{\partial \eta}+\zeta_y\frac{\partial g^v}{\partial \zeta} \qquad (2.D.47)$$

$$\frac{\partial h^v}{\partial z}=\xi_z\frac{\partial h^v}{\partial \xi}+\eta_z\frac{\partial h^v}{\partial \eta}+\zeta_z\frac{\partial h^v}{\partial \zeta} \qquad (2.D.48)$$

If we multiplying through by $J'=Jt_\tau$ and rearrange, the conservative vector form of the equations becomes the following.

$$\begin{aligned}
&\frac{\partial}{\partial\tau}(Jq)+\frac{\partial}{\partial\xi}\left[Jt_\tau(\xi_t q+\xi_x f+\xi_y g+\xi_z h)\right]\\
&+\frac{\partial}{\partial\eta}\left[Jt_\tau(\eta_t q+\eta_x f+\eta_y g+\eta_z h)\right]\\
&+\frac{\partial}{\partial\zeta}\left[Jt_\tau(\zeta_t q+\zeta_x f+\zeta_y g+\zeta_z h)\right]=\frac{\partial}{\partial\xi}\left[\frac{Jt_\tau}{Re'_\infty}(\xi_x f^v+\xi_y g^v+\xi_z h^v)\right]\\
&+\frac{\partial}{\partial\eta}\left[\frac{Jt_\tau}{Re'_\infty}(\eta_x f^v+\eta_y g^v+\eta_z h^v)\right]\\
&+\frac{\partial}{\partial\zeta}\left[\frac{Jt_\tau}{Re'_\infty}(\zeta_x f^v+\zeta_y g^v+\zeta_z h^v)\right]+J'b
\end{aligned} \tag{2.D.49}$$

where the following is true.

$$\bar{Q}=Jq \tag{2.D.50}$$

$$F=Jt_\tau(\xi_t q+\xi_x f+\xi_y g+\xi_z h) \tag{2.D.51}$$

$$G=Jt_\tau(\eta_t q+\eta_x f+\eta_y g+\eta_z h) \tag{2.D.52}$$

$$H=Jt_\tau(\zeta_t q+\zeta_x f+\zeta_y g+\zeta_z h) \tag{2.D.53}$$

$$F^v=Jt_\tau(\xi_x f^v+\xi_y g^v+\xi_z h^v) \tag{2.D.54}$$

$$G^v=Jt_\tau(\eta_x f^v+\eta_y g^v+\eta_z h^v) \tag{2.D.55}$$

$$H^v=Jt_\tau(\zeta_x f^v+\zeta_y g^v+\zeta_z h^v) \tag{2.D.56}$$

With definitions 2.D.50 through 2.D.56, equation 2.D.49 becomes.

$$\frac{\partial\bar{Q}}{\partial t}+\frac{\partial F}{\partial\xi}+\frac{\partial G}{\partial\eta}+\frac{\partial H}{\partial\zeta}=\frac{1}{Re'_\infty}\left[\frac{\partial F^v}{\partial\xi}+\frac{\partial G^v}{\partial\eta}+\frac{\partial H^v}{\partial\zeta}\right]+Jt_\tau b \tag{2.D.57}$$

Like before, we can group the Reynolds number inside the flux vector variables.

$$\tilde{F}^v=\frac{F^v}{Re'_\infty}=\frac{Jt_\tau}{Re'_\infty}(\xi_x f^v+\xi_y g^v+\xi_z h^v) \tag{2.D.58}$$

$$\tilde{G}^v=\frac{G^v}{Re'_\infty}=\frac{Jt_\tau}{Re'_\infty}(\eta_x f^v+\eta_y g^v+\eta_z h^v) \tag{2.D.59}$$

$$\tilde{H}^v=\frac{H^v}{Re'_\infty}=\frac{Jt_\tau}{Re'_\infty}(\zeta_x f^v+\zeta_y g^v+\zeta_z h^v) \tag{2.D.60}$$

Moving everything to the LHS and applying expressions 2.D.58 through 2.D.60, we arrive at the strong conservation law form of our governing equations.

$$\frac{\partial \bar{Q}}{\partial t}+\frac{\partial}{\partial \xi}(F-\tilde{F}^{v})+\frac{\partial}{\partial \eta}(G-\tilde{G}^{v})+\frac{\partial}{\partial \zeta}(H-\tilde{H}^{v})-J t_{\tau} b=0 \qquad (2.D.61)$$

where $\bar{Q}$, F , G , and H are calculated using equations 2.D.50 through 2.D.53.

$$\bar{Q}=Jq$$

$$F=J t_{\tau}(\xi_{t} q+\xi_{x} f+\xi_{y} g+\xi_{z} h)$$

$$G=J t_{\tau}(\eta_{t} q+\eta_{x} f+\eta_{y} g+\eta_{z} h)$$

$$H=J t_{\tau}(\zeta_{t} q+\zeta_{x} f+\zeta_{y} g+\zeta_{z} h)$$

$\tilde{F}^{v}$, $\tilde{G}^{v}$, and $\tilde{H}^{v}$ are calculated using equations 2.D.58, 2.D.59, and 2.D.60, respectively.

$$\tilde{F}^{v}=\frac{J t_{\tau}}{Re'_{\infty}}(\xi_{x} f^{v}+\xi_{y} g^{v}+\xi_{z} h^{v})$$

$$\tilde{G}^{v}=\frac{J t_{\tau}}{Re'_{\infty}}(\eta_{x} f^{v}+\eta_{y} g^{v}+\eta_{z} h^{v})$$

$$\tilde{H}^{v}=\frac{J t_{\tau}}{Re'_{\infty}}(\zeta_{x} f^{v}+\zeta_{y} g^{v}+\zeta_{z} h^{v})$$

Keeping in mind our subscript notation, we can rewrite equations 2.C.57 through 2.C.60.

$$x_{1}=x, \xi_{1}=\xi, u_{1}=u, f_{1}=f_{x}$$
$$x_{2}=y, \xi_{2}=\eta, u_{2}=v, f_{2}=f_{y}$$
$$x_{3}=z, \xi_{3}=\zeta, u_{3}=w, f_{3}=f_{z}$$

$$q=\begin{bmatrix} \rho \\ \rho u \\ \rho v \\ \rho w \\ \rho e_{t} \end{bmatrix} \qquad (2.D.62)$$

$$f = \begin{bmatrix} \rho u \\ \rho u^2 + p \\ \rho u v \\ \rho u w \\ u(\rho e_t + p) \end{bmatrix} \tag{2.D.63}$$

$$g = \begin{bmatrix} \rho v \\ \rho v u \\ \rho v^2 + p \\ \rho v w \\ v(\rho e_t + p) \end{bmatrix} \tag{2.D.64}$$

$$h = \begin{bmatrix} \rho w \\ \rho w u \\ \rho w v + p \\ \rho w^2 + p \\ w(\rho e_t + p) \end{bmatrix} \tag{2.D.65}$$

$$b = \begin{bmatrix} 0 \\ \rho f_x \\ \rho f_y \\ \rho f_z \\ \rho(f_x u + f_y v + f_z w) \end{bmatrix} \tag{2.D.66}$$

$$f^v = \begin{bmatrix} 0 \\ \tau_{11} \\ \tau_{12} \\ \tau_{13} \\ u\tau_{11} + v\tau_{21} + w\tau_{31} + \dfrac{1}{\gamma - 1}\dfrac{\mu}{Pr}\dfrac{\partial a^2}{\partial x} \end{bmatrix} \tag{2.D.67}$$

$$g^v = \begin{bmatrix} 0 \\ \tau_{21} \\ \tau_{22} \\ \tau_{23} \\ u\tau_{12} + v\tau_{22} + w\tau_{32} + \dfrac{1}{\gamma - 1}\dfrac{\mu}{Pr}\dfrac{\partial a^2}{\partial y} \end{bmatrix} \tag{2.D.68}$$

$$h^{v}=\begin{bmatrix} 0 \\ \tau_{31} \\ \tau_{32} \\ \tau_{33} \\ u\,\tau_{13}+v\,\tau_{23}+w\,\tau_{33}+\dfrac{1}{\gamma-1}\dfrac{\mu}{Pr}\dfrac{\partial a^{2}}{\partial z} \end{bmatrix} \tag{2.D.69}$$

$$\tau_{11}=(\lambda+2\mu)\frac{\partial u}{\partial x}+\lambda\left(\frac{\partial v}{\partial y}+\frac{\partial w}{\partial z}\right) \tag{2.D.70}$$

$$\tau_{22}=(\lambda+2\mu)\frac{\partial v}{\partial y}+\lambda\left(\frac{\partial u}{\partial x}+\frac{\partial w}{\partial z}\right) \tag{2.D.71}$$

$$\tau_{33}=(\lambda+2\mu)\frac{\partial w}{\partial z}+\lambda\left(\frac{\partial u}{\partial x}+\frac{\partial v}{\partial y}\right) \tag{2.D.72}$$

$$\tau_{21}=\tau_{12}=\mu\left(\frac{\partial v}{\partial x}+\frac{\partial u}{\partial y}\right) \tag{2.D.73}$$

$$\tau_{31}=\tau_{13}=\mu\left(\frac{\partial w}{\partial x}+\frac{\partial u}{\partial z}\right) \tag{2.D.74}$$

$$\tau_{32}=\tau_{23}=\mu\left(\frac{\partial w}{\partial y}+\frac{\partial v}{\partial z}\right) \tag{2.D.75}$$

CHAPTER III
Flow Solver

During this research, all numerical simulations were calculated using the SimCenter's "in house" flow solver called "Tenasi". The "Tenasi" code is a finely tuned and proven flow solver used for Computational Fluid Dynamics (CFD) research and design performed by the University of Tennessee at Chattanooga (UTC). "Tenasi" is a robust code which solves the three-dimensional, time-dependent, Reynolds-averaged Navier-Stokes (RANS) equations. This chapter highlights some of the key features of the "Tenasi" code to convey the code's power and versatility.

A. The UTC "Tenasi" Flow solver

"Tenasi" is a steady and unsteady three-dimensional flow solver capable of calculating solutions for incompressible, compressible, and arbitrary-Mach flow cases. Being an edge based solver, "Tenasi" has the versatility to incorporate structured, unstructured, and mixed hybrid grids. The discretized three-dimensional grid follows a node centered methodology. The median dual technique is used to calculated spacial volumes around each node. Node, edge, and element connectivities are maintained throughout the calculations. Compressed row storage and ribbon vector techniques are implemented for rapid memory and data accessibility.

Like many mainstream CFD solvers, the "Tenasi" code's parallel processing features considerably improves run times for large computational grids. Domain decomposition is user specified with the general rule of limiting 150,000 nodes per processor. Node-to-node connectivity is maintained across the block-to-block interfaces

to minimize interpolation errors. Memory messaging is distributed and passed using the MPI libraries.

The "Tenasi" code has a variety of start up features. Interior nodes can be preset to a scaled value of the free-stream flow conditions. A scaling factor of one sets all variables, stored at the nodes, to free-stream flow conditions. A scaling factor of zero presets all values to an initial condition similar to a vacuum. When it comes to time stepping, "Tenasi" has two options. A user specified time step can be declared or a constant Courant–Friedrichs–Lewy (CFL) number can be chosen when running the flow solver. Courant number is defined as the following.

$$CFL = u\frac{\Delta t}{\Delta x} \tag{3.A.1}$$

where

Δt = time step
Δx = spacial interval
u = velocity

Specifying a time step value insures the numerical solution progresses at the user declared time interval. With the grid specifying the spacial interval, the CFL number varies at each node while maintaining a constant time step. Running the code at a constant CFL number allows the time step to float at each node. Thus, the numerical solution iterates non uniformly with respect to time towards a steady state solution. Equation 3.A.2 is for calculating the local time step in the case of running a constant CFL.

$$\Delta t = CFL\,\frac{\Delta x}{u} \tag{3.A.2}$$

To insure stability during the early iterations, the "Tenasi" code has the flexibility to ramp the CFL number over a specified increment of numerical iterations. The process of "ramping" the Courant number can greatly reduce the iteration count when seeking a steady state solution. Also, the "Tenasi" code has restart capabilities, allowing the user to start from a previous solution file.

"Tenasi" has the option to run both explicitly and implicitly in the temporal direction. An implicit temporal scheme has the advantage of running higher CFL numbers while remaining numerically stable. Temporal accuracy is improved by using a Relaxed Newton's method. The iterative Newton's method is shown below.

$$x^{k+1} = x^k - \frac{F(x^k)}{F'(x^k)} \tag{3.A.3}$$

where x^0 is an initial guess. The following is also true.

$$F'(x) = \frac{\partial F(x)}{\partial x} \tag{3.A.4}$$

The Relaxed Newton's method includes a scaling factor, h .

$$x^{k+1} = x^k - h\frac{F(x^k)}{F'(x^k)} \tag{3.A.5}$$

where

$h < 1$ = under relaxed
$h > 1$ = over relaxed
$h = 1$ = reduces to original Newton's Method

Since the term $F'(x)$ is difficult to invert, equation 3.A.5 can be rewritten in the following way.

$$\frac{1}{h}F'(x^k)(x^{k+1} - x^k) = -F(x^k) \tag{3.A.6}$$

The Relaxed Newton's method iteratively converges towards a solution within a numerical time step. The increased computational cost of implementing Newton's method is justified by the higher order of convergence. The user specifies the number of “inner” Newton iterations to perform inside each “outside” numerical iteration. Newton's method is used to linearize the system of nonlinear questions while removing linearization errors in the unsteady terms. The final discretized linear system, $Ax=b$, is solved using the Symmetric Gauss-Seidel algorithm.

$$x^{k+1}=(D-L)^{-1}(Ux^{k}+b) \tag{3.A.6}$$

where the original A matrix is broken up into three components: the diagonal D , the lower triangle L , and the upper triangle U . Recall, the Gauss-Seidel method uses previously solved results as soon as they are available.

First order inviscid fluxes are calculated using Roe averaging techniques.(Roe, 1981) Second and third order spatial accuracy is achieved using the TVD schemes by Osher and Chakravarty.(1984) Viscous terms are obtained by a directional derivative scheme. A central differencing scheme is used to derive the viscous flux velocity derivatives. If necessary, “Tenasi” can implement both Barth and Venkatakrishnan flux limitation techniques. All derivatives and Jacobian values can be calculated using numerical or analytical differentiation. In the area of turbulence models, the “Tenasi” code offers the user a choice from five models: the Spalart-Allmaras and Menter SAS one-equation models as well as the $q-\omega$, Mentor SST, and the Mentor hybrid $k-\omega, k-\epsilon$ two-equation techniques. Further details on the main features of “Tenasi” may be found in Gatlin (1987), Whitfield (1988), Arabshahi (1989), Vanden (1992), Arabshahi and Whitfield (1995). Much of the explanation for the implementation and use of parallel, unstructured flow solvers may be found in Hyams. (2000)

CHAPTER IV
Solid Model

A solid model of the S-duct geometry was created using the Pro Engineer (Pro-E) 3-D modeling software. To virtually render the 2.5% scale inlet tested at the NASA Langley Research Center, duct dimensions and model specifications for the "Inlet-A" geometry were obtained from two S-duct documents by Berrier and Owens.(2005, 2008) The one hundred and seventy-six flow control air-jets were inserted into the Pro-E solid model in agreement with the engineering drawings by Ortega.(2004) This chapter summarizes the steps taken in virtually modeling the flat plate, cowl, and S-duct. The chapter also discusses the process used for rendering the 176 air jet flow control devices.

A. The Pro-E Solid model

As stated, Pro-E Wildfire 2.0 was used to generate the flat plate, cowl, and S-duct. Model specifications from Owens, Allan, and Gorton (2008) were cross referenced with the data presented by Berrier, Carter, and Allan (2005) to achieve a coherent geometric description of the "Inlet-A" geometry. Immediately following are notable dimensions for the "Inlet-A" geometry.

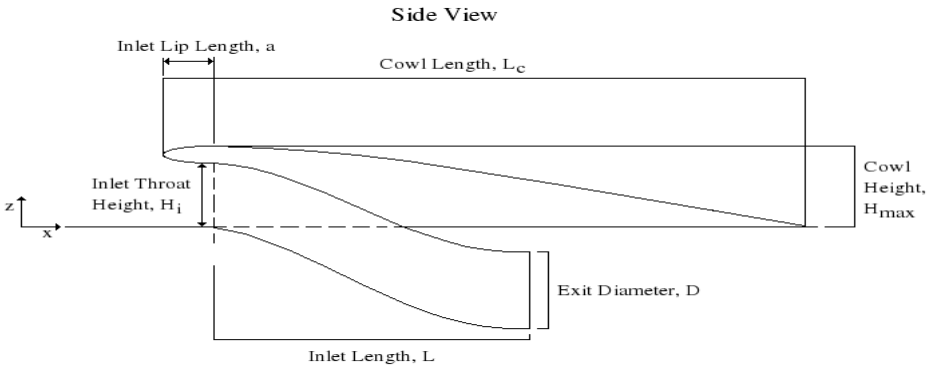

Figure 4: Side view of "Inlet-A" geometry.

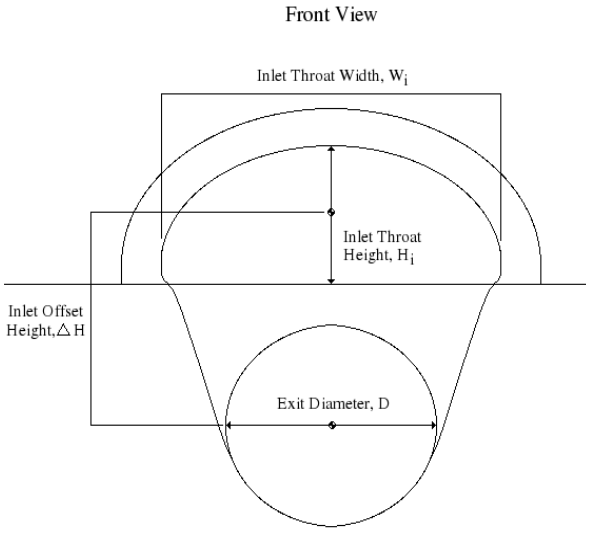

Figure 5: Front view of "Inlet-A" geometry.

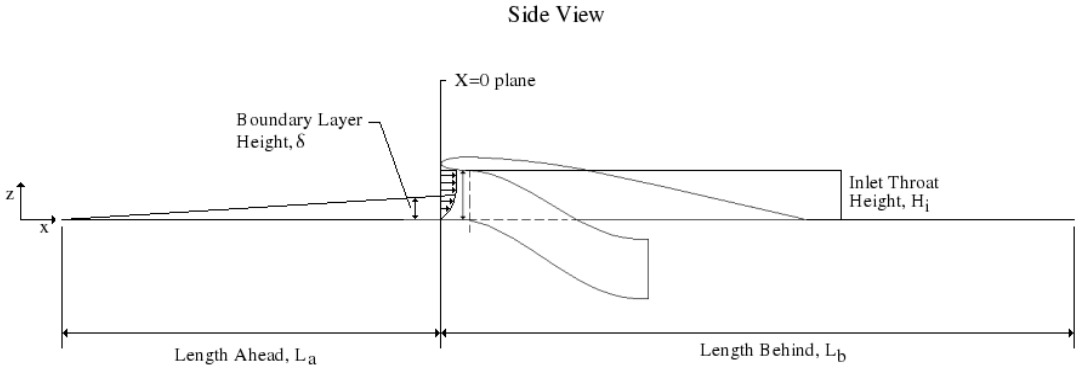

Figure 6: Side view of flat plate geometry.

Table 1: Notable geometry dimensions.

Note: All values are in Inches.

Inlet Lip Length, a	0.479	Inlet Length, L	7.696
Exit Diameter, D	2.448	Flat Plate Length Ahead, L_a	50.000
Inlet Throat Height, H_i	1.703	Flat Plate Length Behind, L_b	70.000
Cowl Maximum Height, H_{max}	2.185	Cowl Length, L_c	15.323
Inlet Offset Height, ΔH	2.543	Inlet Throat Width, W_i	3.249

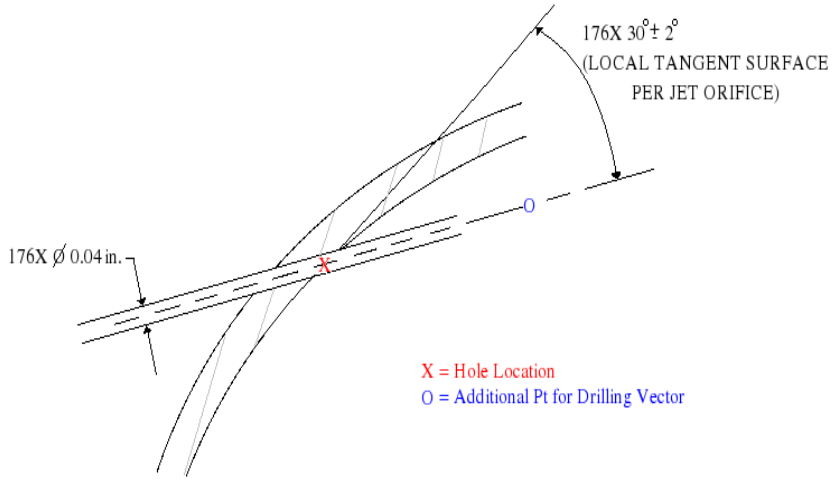

Figure 7: Jet hole specifications.

In agreement with the engineering drawings by Ortega (2004), the jet holes were "drilled" at an angle of 30 degrees with respect to the local S-duct surface. The jet flow control devices were angled in such a way to diminish the secondary flow building up along the surface wall. The air jet angle calculations are in a constant X-plane, meaning the local surface tangential slope is only dependent on the Y and Z-axis components. In other words, the injection angle or "drilling" angle simplified to a two dimensional calculation. To obtain a "drilling" vector for all 176 jets, a C-language computer code was written to calculate the local surface tangential slopes for any given hole. The code took the Cartesian coordinates for any hole location (denoted in figure 7 as the red "X") and calculated an additional point (shown in figure 7 as the blue "O") for specifying a "drilling" vector. The tangential surface slope was approximated by the Forward and Backward Euler Methods. Equations 4.A.1 and 4.A.2 show the Forward and Backward Euler equations, respectively.

$$y'(t) = \frac{y(t+h) - y(t)}{h} \qquad (4.A.1)$$

$$y'(t)=\frac{y(t)-y(t-h)}{h} \tag{4.A.2}$$

The "run" and "rise" making up the slope corresponds to the Y and Z axis, respectively. Let the stepping criteria, h , be the Y-axis displacement from one jet to the next. The Backward Euler method (4.A.2) was used to calculate the tangential slope for jet holes lying on the lower surface of the S-duct. Inserting the stepping criteria, the Backward Euler equation becomes

$$z'(n)=\frac{z(n)-z(n-1)}{y(n)-y(n-1)} \tag{4.A.3}$$

where the variable n represent the node or jet hole number. The Forward Euler equation 4.A.1 was found to be a better tangential slope estimate for jet holes located on the side wall.

$$z'(n)=\frac{z(n+1)-z(n)}{y(n+1)-y(n)} \tag{4.A.4}$$

After calculating a tangential slope from equations 4.A.3 or 4.A.4, the tangential angle was calculated using the inverse tangent function.

$$\theta_t=\tan^{-1}(z'(n)) \tag{4.A.5}$$

The 30 degree injection angle was applied to the tangential angle calculated by equation 4.A.5. The code used this injection or "drilling" angle to calculate Cartesian coordinate values for additional vector referencing points. These additional points were used to define the 176 unique "drilling" vectors. The additional points were placed away from the jet hole locations at a vector length of 0.1 inches. "Drilling" vectors for all 176 jets were obtained by combining the additional points with the hole locations using Pro-E's axis tool. Material was subtracted from the solid model using the revolve tool. Revolutions were made about the "drilling" vector axis. The jet hole diameter was set to

0.04 inches as specified by Ortega.(2004) Figures 4.5 and 4.6 provide a visual interpretation of how the additional points were used to line up the “drilling” vectors or injection angles for section-A and section-H, respectively. Section-A lies in a constant X-plane 7.356 inches upstream of the aerodynamic interface plane (AIP). Like wise, section-H is located 4.088 inches in front of the AIP. A “dotted” line is used to connect the hole locations, providing a general idea of the S-duct profile. The vantage point for figures 8 and 9 is from the duct exit looking upstream and out the front of the inlet.

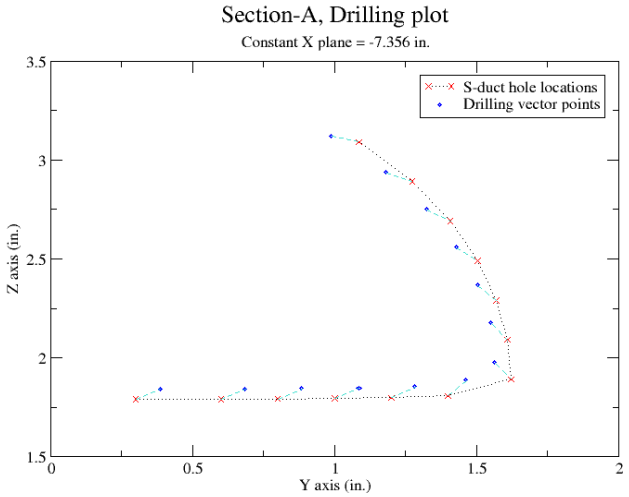

Figure 8: Drilling plot for jet section-A.

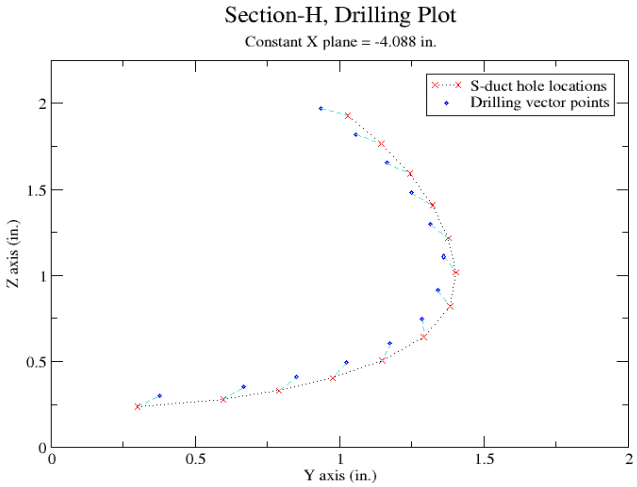

Figure 9: Drilling plot for jet section-H.

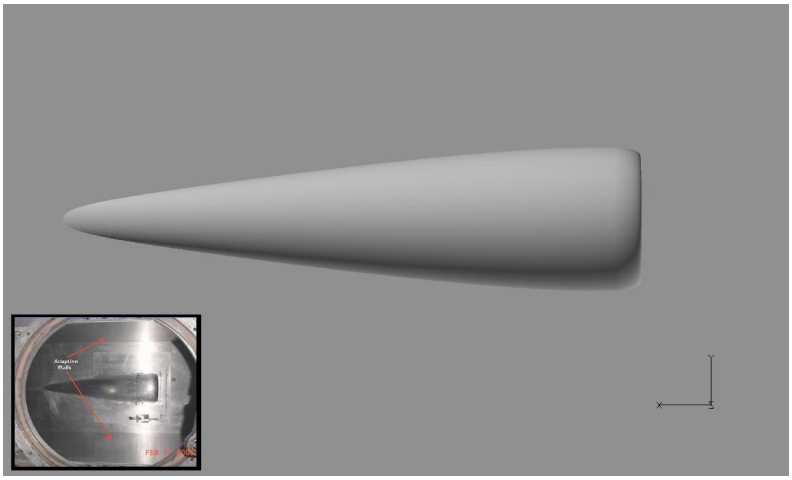

Figure 10: Top view of solid model.

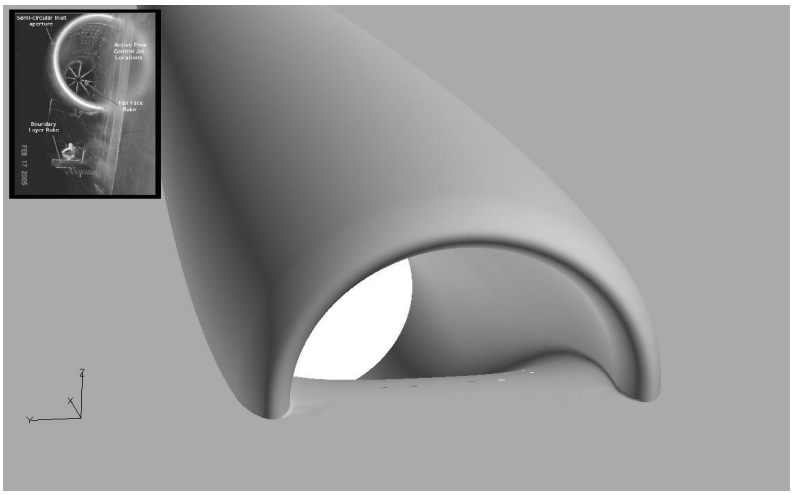

Figure 11: Iso view of solid model.

Figures 10 and 11 show the finished Pro-E solid model. The Pro-E assembly feature was used to combine the two Pro-E part files containing the flat plate, cowl, and S-duct. The small photo inserts seen in figures 10 and 11 are images of the 2.5% scale “inlet-A” S-duct tested at the NASA Langley Research Center.(Owens, 2008)

CHAPTER V
Grid

Over the course of this research, a total of three computational grids were constructed in attempts of matching the experimental data presented by Owens, Allen, and Gorton.(2006) The 16-jet “configuration-10” setup was chosen for this study due to the configuration's ability to clearly reduce the circumferential distortion (DPCP) at the aerodynamic interface plane (AIP). All three-dimensional grids were constructed using the Computational Fluid Dynamics (CFD) meshing software Gridgen. Owens, Allan, and Gorton (2006) provided a Gridgen database file including the 2.5% scale inlet, flat plate, and tunnel walls. The inflow boundary plane was spaced upstream to produce the appropriate boundary-layer-to-height ratio of 35% required at the S-duct inlet. A Pro-E IGES file of the 16-jet “configuration-10” was imported into Gridgen to render the jet hole geometries. This chapter documents the details of the grid making process. Topics covered include: the selection of an experimental case, a brief revisit to the Pro-E solid model, grid modifications learned from computational results by Sreenivas and Sawyer (2008), and a description of the iterative grid process, resulting in the three computational grids used in this study.

A. Selecting an Experimental Case

Owens, Allan, and Gorton (2006) stored their experimental results in a Microsoft Excel sheet. The NASA Langley wind tunnel experiments tested three variables that influenced distortion at the AIP or fan face location. The first variable was the number of jets chosen to divide up the cumulative jet mass flow rate. The second variable was jet location. With176 jet locations to choose from, there are a extensive number of possible

jet configurations. The configurations Owens tested are denoted by the configuration number, ranging from R013 to R107. The third variable was the cumulative jet mass flow rate, MFR_{jets}, passing through the combined number of jets. A variety of jet mass flow rates were tested for any given jet configuration. The spread of jet mass flow rate cases are recorded using a Pt.# system. The experimental test case, chosen for comparison purposes, was designated as 554 R094. Jet configuration R094 was found to be a 16-jet version of "configuration-10". According to the journal article by Owens, Allan, and Gorton (2008), case 554 R094 showed clear signs of reducing circumferential distortion at the AIP for relatively low mass flow ratios. The mass flow ratio is a percentage of the jet mass flow rate with respect to the inlet mass flow rate, MFR_{inlet}.

$$Mass\ \ Flow\ \ Ratio = \frac{MFR_{jets}}{MFR_{inlet}} \tag{5.A.1}$$

Due to the relatively low number of jets and the favorable reduction in distortion, case R094 could be a practical implementation of the air jet flow control device. Initial research started with the "baseline" case recorded as R094 Pt. 771. The term "baseline" was used because $MFR_{jets} = 0$. Jet mass flow rate was varied for the remainder of experimental test cases. Data for these cases were stored as R094 Pt. 772, R094 Pt. 773, and so on. Not interested in reproducing every jet mass flow rate case, this study simulated only the odd number cases (Pt. 773, Pt. 775, and Pt.777), hoping to reproduce the distortion reduction trend recorded by Owens, Allan, and Gorton in 2006.

B. Solid Model Revisited

Even though a Gridgen database file was provided by the engineers at NASA Langley, the Pro-E solid model needed to accurately render any jet configuration. Unique "drilling" vectors for each jet translates into unique ellipses specifying the jet hole edges.

In terms of up front cost, the Pro-E model was time consuming. Yet by rendering all 176 jet holes, any possible jet configuration could be obtained by manipulating the Pro-E model source tree. By “hiding” unused jets within the source tree, an IGES file containing the 16-jet “configuration-10 “setup was exported from Pro-E. Figure 12 shows the 16-jet “configuration-10” solid model. The air jet flow control devices are highlighted in red.

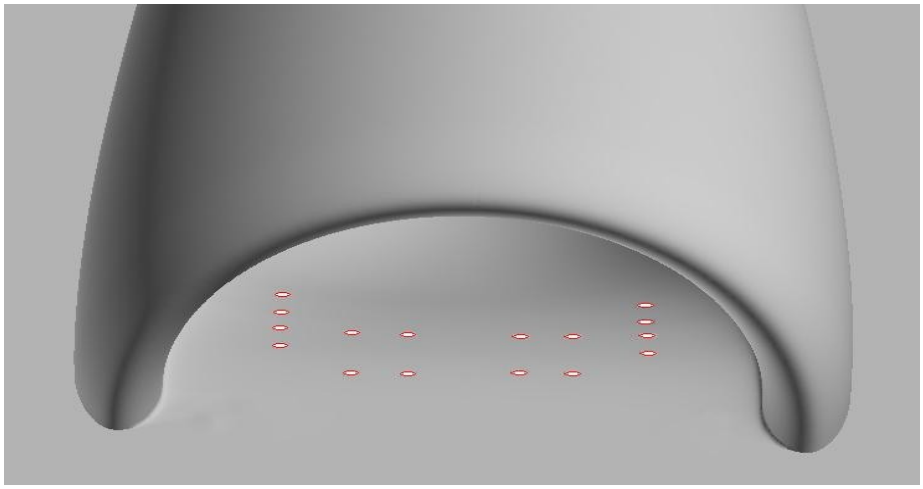

Figure 12: 16 jet, Configuration-10 solid model.

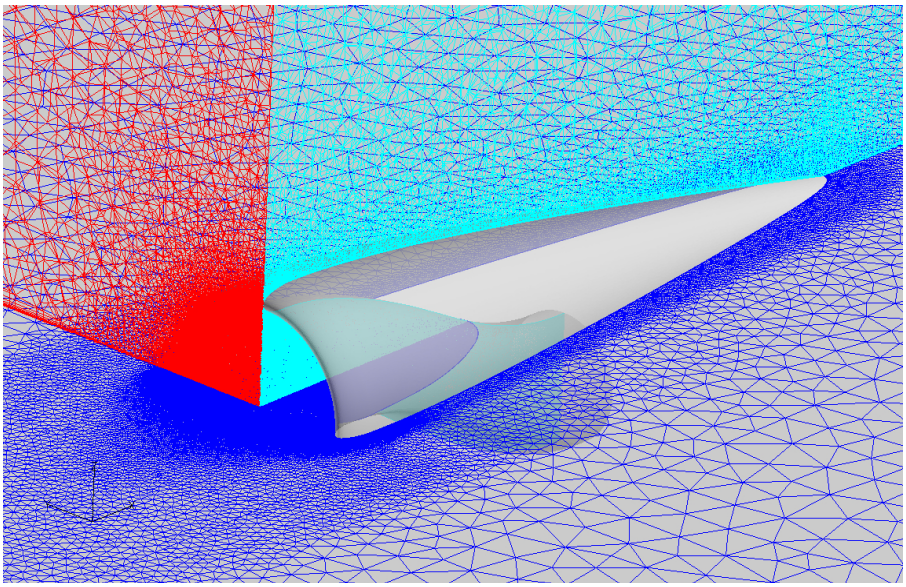

Figure 13: Iso view depicting the reference X,Y, and Z-axis planes.

As seen in figure 13, the X = 0 plane (represented by the color red) coincides with the constant X-plane passing through the leading edge of the cowl. The Y = 0 plane (highlighted in a light blue) is the symmetry plane for the cowl and inlet geometries. The Z = 0 plane (depicted as dark blue) lies on the flat plate boundary in which the cowl is mounted. This referencing configuration is maintained through out the course of this computational study.

C. Grid Refinements Obtained From Previous SimCenter Research

Initial research on the “inlet-A” geometry was conducted by Sreenivas and Sawyer.(2008) Using Owens' provided database file, a hybrid structured and unstructured grid was constructed to replicate the exact experimental setup used at the NASA Langley research facility. The database file included dimensional surface definitions for the wind tunnel walls, cowl, and 2.5% scale “inlet-A” S-duct geometry. Initial research returned valuable information on the S-duct flow characteristics and possible grid refinements. Shown below is a Mach number plot from the initial research.

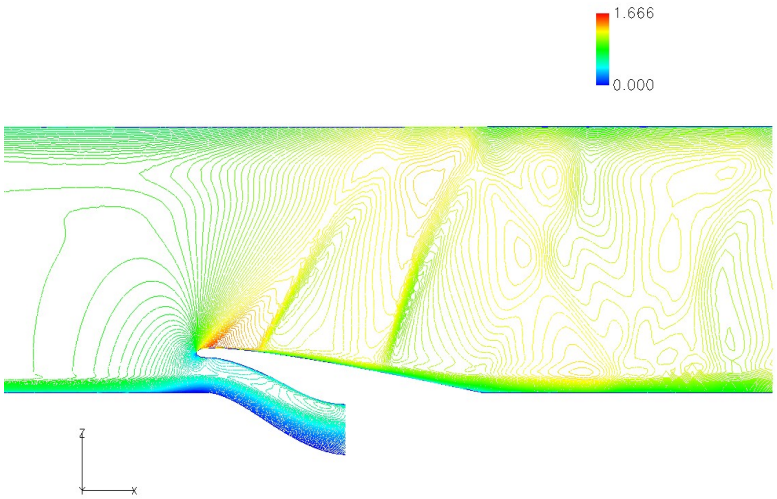

Figure 14: Mach number plot of grid using provided database.

Figure 14 revealed two shocks forming downstream of the S-duct inlet. It is interesting to note that the plot shows signs of the shocks reflecting off the tunnel walls. There was concern the shocks could affect the flow upstream and flow within the S-duct. As a result, the tunnel walls were replaced by farfield domains for future computational grids.

To maintain a cube-like farfield grid geometry, the flat plate length behind the inlet was extended to 70 inches. The flat plate length ahead of the inlet remained at 50 inches to maintain the necessary 35% boundary-layer-to-inlet height ratio. The tunnel side walls were replaced with farfield domains spaced 60 inches in the positive and negative Y-directions. The tunnel ceiling was replaced with another farfield domain spaced approximately 112 inches above the flat plate. The combined height, including the S-duct, was about 115 inches. Thus, the cube-like grid had dimensional specifications of 120 inches by 120 inches by 115 inches. Using these new grid dimensions, Sreenivas and Sawyer found that the shocks and other flow characteristics downstream of the S-duct inlet had little-to-no effect on the flow within the S-duct. Grid modifications to the outer boundaries by Sreenivas and Sawyer carried over to the grid process performed in this research. Figures 15 and 16 show the cube-like outer boundaries.

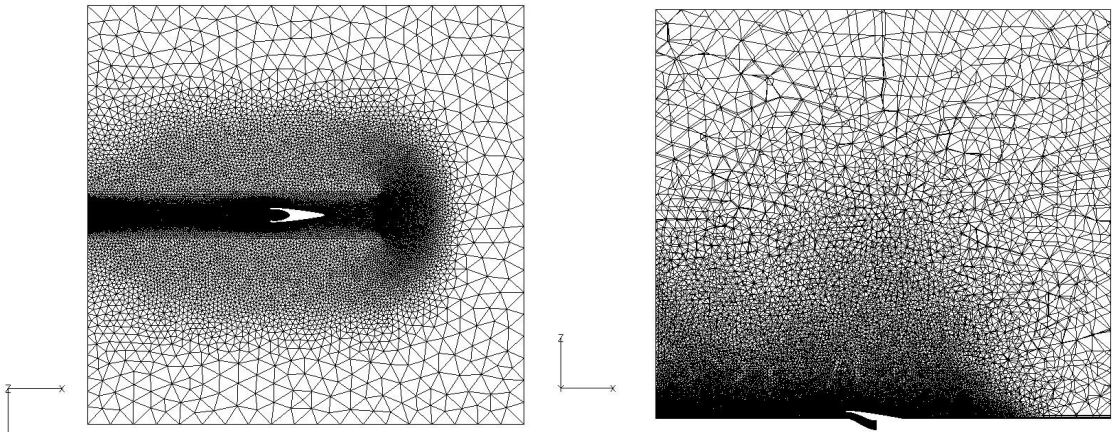

Figure 15:(left) Z=0 plane of cube-like grid.

Figure 16:(right) Y=0 plane of cube like grid.

D. Iterative Grid Process

The Pro-E IGES file containing the16-jet “configuration-10” surface definition was appended to the cube-like grid created by Sreenivas and Sawyer. Treating Owens' database file as the superior model for the cowl and S-duct, the Pro-E file was imported solely for locating the jet hole edges. Once the two database files coincided, the jet hole edges could be rendered using Gridgen's connector tool. Gridgen's domain tools were used to create unstructured grid domains. Both the jet connectors and jet domains were verified to be 100% on the S-duct surface definition. Figure 17 shows how the jets were rendered only as jet domains for the first computational grid. This was simpler and quicker to implement. Yet, the full jet holes were eventually added in the second and third computational grids.

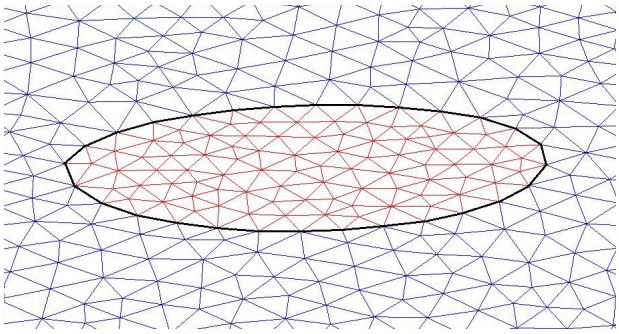

Figure 17: Single jet grid domain.

In figure 17, the jet domain is depicted with red triangle elements. The jet hole edges are highlighted by the bold black edges, and the S-duct surface can be seen by the blue triangle elements. Triangle areas and tetrahedron volumes around the vicinity of the jet hole domains could be adjusted using Gridgen's boundary decay parameter. This feature was used to pack grid cells near connectors with fine grid spacings. Figures 18 and 19 show the element packing along the S-duct surface domain. Jet holes are represented by blank ovals appearing on the S-duct surface.

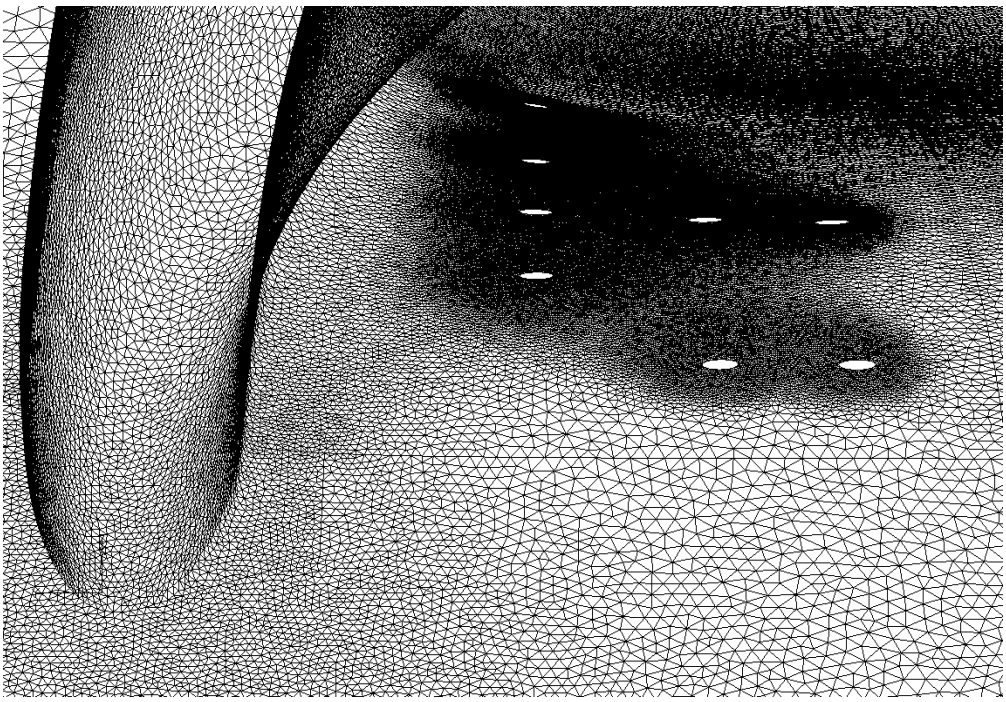

Figure 18: Grid spacing along the S-duct surface.

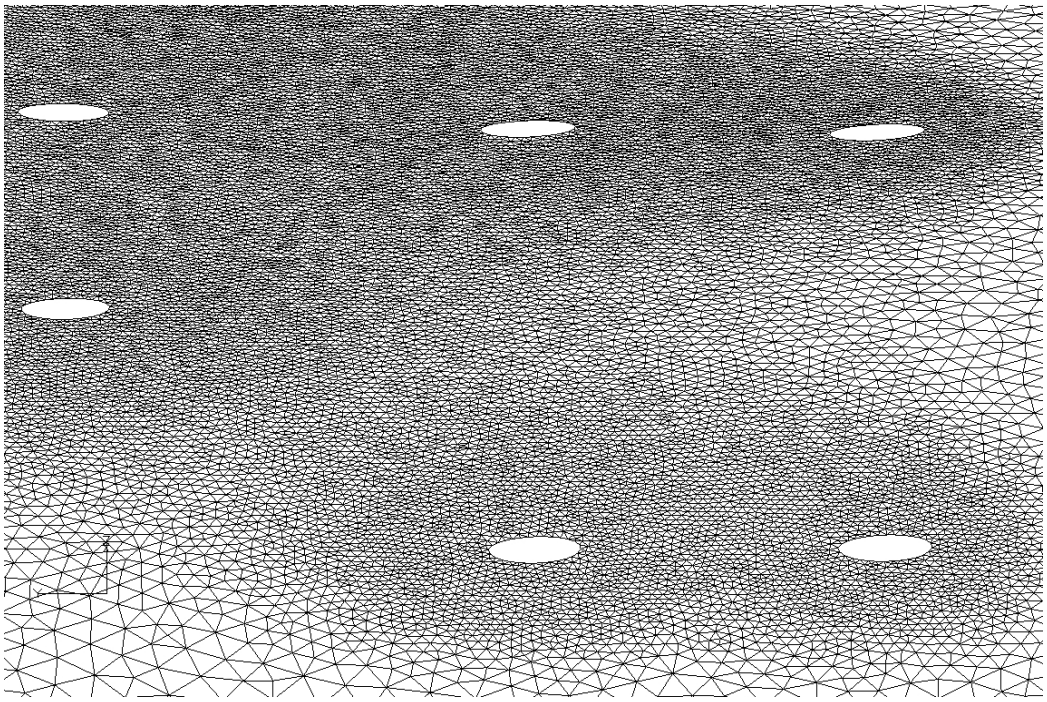

Figure 19: Closer look at grid spacing along the S-duct surface.

The simplest way to represent the jet holes was by manipulating boundary conditions specified for each individual jet domain. Flow conditions for each jet were user specified in the boundary conditions and were uniformly distributed across the whole jet domain. This smaller grid and simpler method for the jets allowed for experimentation with the unknowns of including the air jet flow control devices in the numerical study.

The first grid accumulated just over 4 million nodes with 1.5 million nodes resting inside the S-duct. The first computational grid was purely unstructured and consisted only of tetrahedron elements before the insertion of viscous layers. Viscous layer elements were added using the in-house viscous layer insertion (VLI) program developed by Karmen.(2007) Using linear elastic grid techniques, the VLI code perturbs the boundary nodes in a surface normal direction using prism cells to fill in the user declared number of viscous layers. Viscous layer packing for all three grids start at 1e-5, increasing at a 1.1 growth rate factor. After the viscous layers were inserted, the grid was ready for decomposition into the user specified number of partitions. The decomped grid was then input into the "Tenasi" flow solver. The final node count (after VLI) for the first computational mesh was approximately 6.5 million. Immediately following are pictures of the inserted viscous layers.

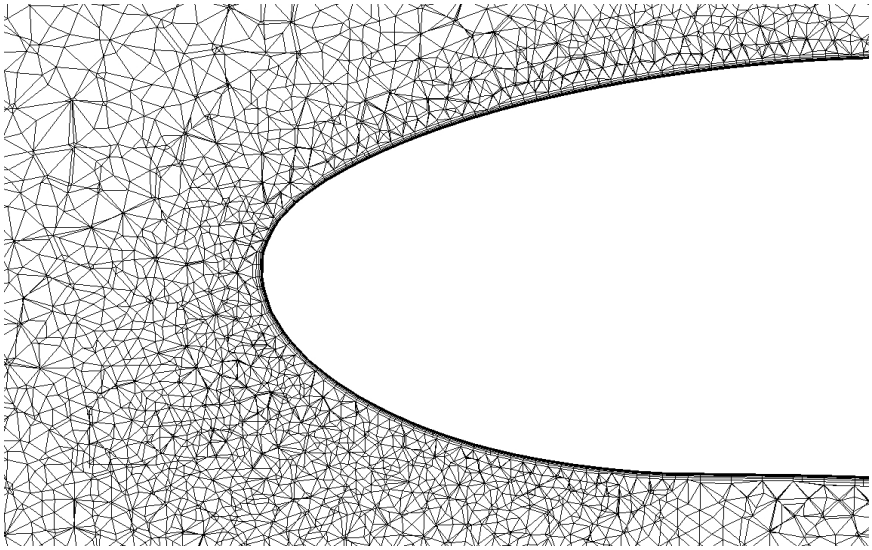

Figure 20: VLI inserted viscous layers.

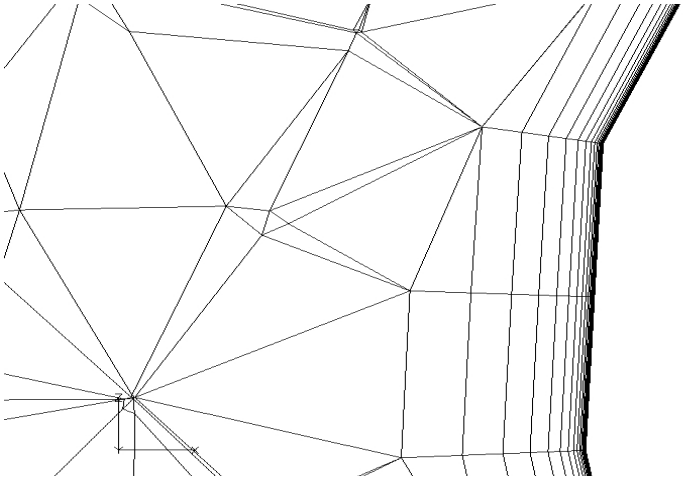

Figure 21: Closer look at the VLI inserted viscous layers.

CFD is indeed an iterative process. Computational grids seem to always need revisions. The second computational grid sought to more realistically replicate the experimental setup documented by Owens, Allan, and Gorton.(2006) By rending more of the actual tunnel model, the physics could be more accurately simulated in agreement with experimental data recorded by the NASA Langley Research Center . The first way the solid model became more realistic was by adding the pressure rake. The pressure rake

radially positions 40 Pitot tubes. The rake placed in the S-duct directly influences fluid flow within the S-duct and pressure readings at the AIP. It was documented in Owens' journal report (2008) that the eight rakes accounted for approximately 15% area blockage on the AIP. Knowing the duct exit diameter is 2.448 inches, frontal area dimensions for a single rake were calculated using the documented 15% value. Other dimensions for the rake assembly were estimated using the SAE Aerospace Recommended Practice 1420 standard.(2002) Even though the Pitot tubes were not rendered, the probe array was place downstream 0.5 inches of the AIP, knowing the Pitot tubes extended upstream from the eight pressure rakes. Note the 0.5 inches is an estimation since previous documents failed to specify the actual distance between the AIP and pressure rake. The second way the computational grid became more realistic was by rendering the fully “drilled” jet holes. The second computational grid remained purely unstructured. Viscous layers were again inserted using Karmen's VLI program.(2007) Figures 22-26 are images of key features of the second computational grid used in this study.

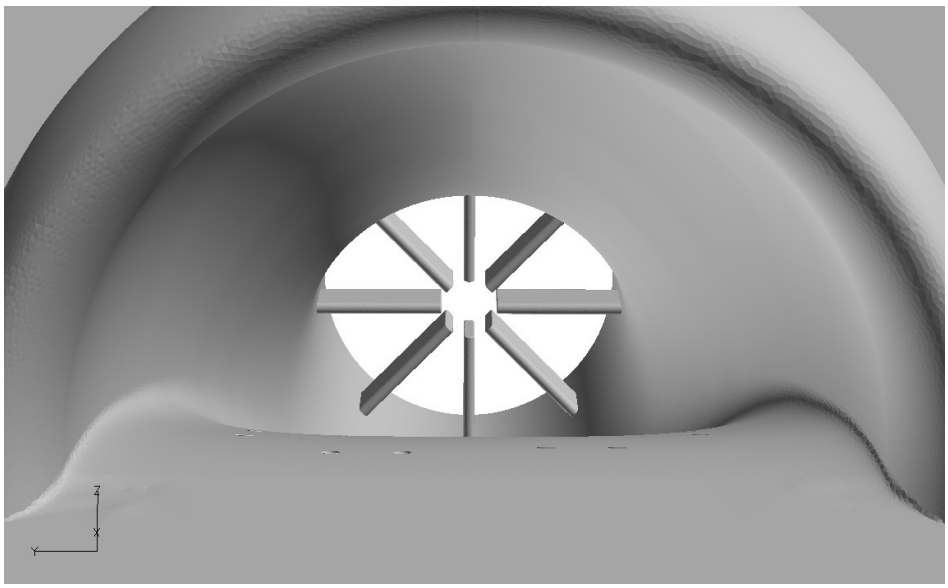

Figure 22: Pressure rake on the second computational grid.

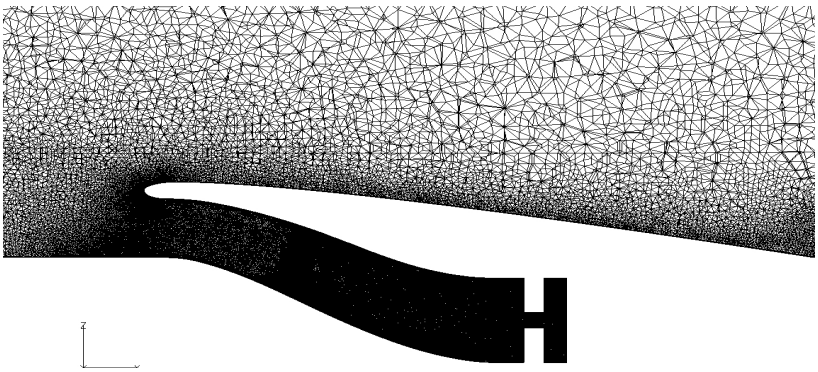

Figure 23: Y=0 plane for second computational grid.

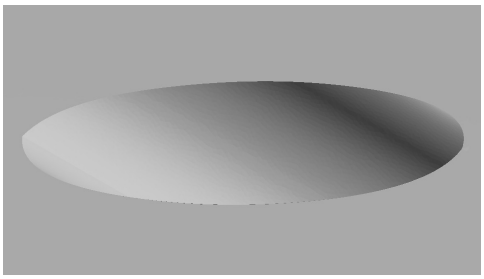

Figure 24: Single jet hole modeled in the second computational grid.

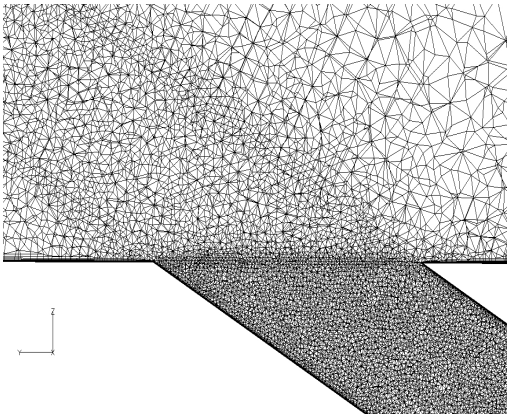

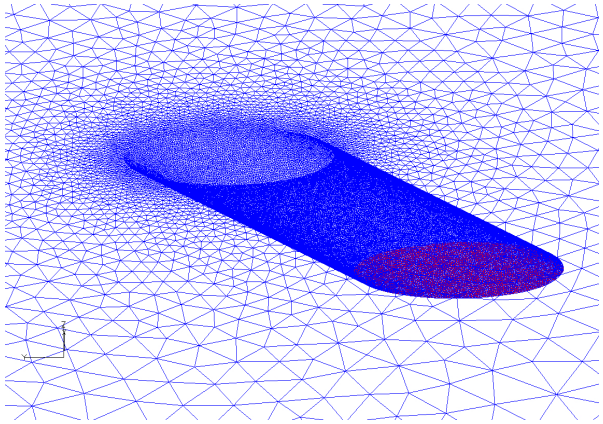

Figure 25:(left) Single jet at the X=0.83 plane.

Figure 26:(right) "Drilled" jet hole domain.

Figure 26 shows the new jet hole domains (depicted by the color red). The S-duct and jet hole solid surfaces are colored in blue. Again, element packing around the jet hole edges was controlled by Gridgen's boundary decay parameter. Total node count for the second computational grid equaled 30.5 million. The substantial node increase was due

to the new solid surfaces, tight cell packing, and viscous layering on all 16 jets and 8 radial rakes.

The third and final grid continued to make minor revisions to better capture the physics of the fluid flow. In the previous two grids, a purely tetrahedron grid was necessary for using the viscous layer insertion program. Upon closer examination, it was found that the triangle surface areas and tetrahedron volumes were too course and insufficient around the jet hole edges. Figure 27 and 28 show the difference in spacing around the jet hole edges.

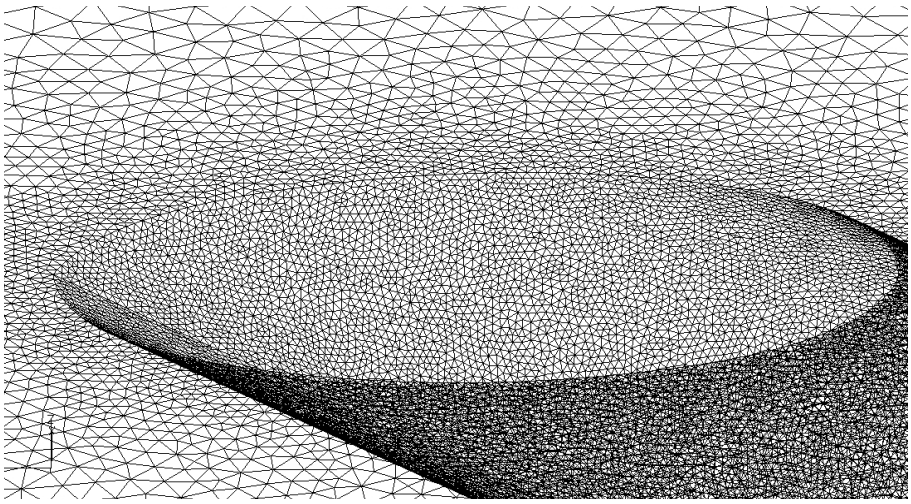

Figure 27. Second computational grid, jet hole edge spacing.

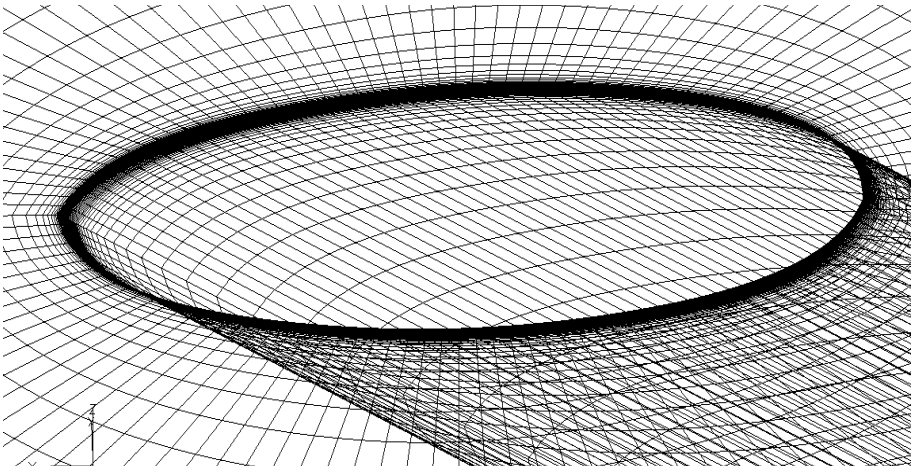

Figure 28. Third computational grid, jet hole edge spacing.

To adequately resolve the jet hole edge, a structured grid type was used in the regions of concern. The structured grid type allowed for better control of the element spacing leading up to the jet hole edge. Structured grids are more time consuming to construct, but adequate spacing is more easily attained at the jet hole edges, rake geometry, and cowl surfaces. The use of structured grids also means the viscous layers have to be user created using Gridgen's block extrusion tool. 35 layers were extruded in a surface normal direction for all solid surface boundaries. Again, viscous layer packing for all three grids start at 1e-5, increasing at a 1.1 growth rate factor.

Another area of concern was that the duct exit. There was concern the specified non-dimensional back pressure, declared at the exit domain, created numerical error upstream by forcing the flow conditions to meet this boundary condition. As a result, the last modification was to extend the duct distance by one exit diameter, 2.448 inches. The third computational grid consisted of 36.9 million nodes. Views of the third computational grid are shown in figures 29 through 34.

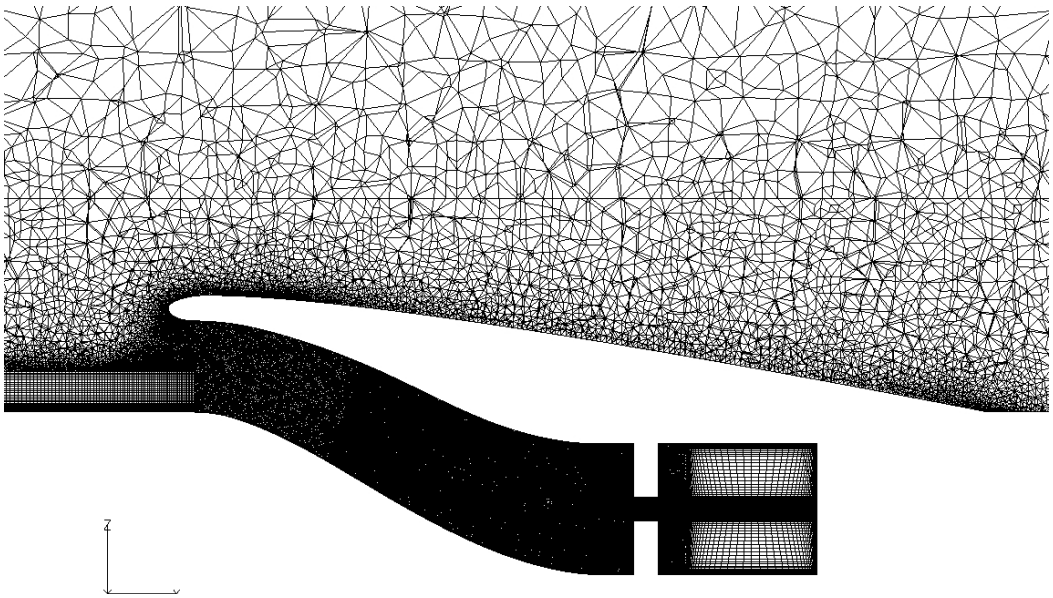

Figure 29: Y=0 plane of third computational grid.

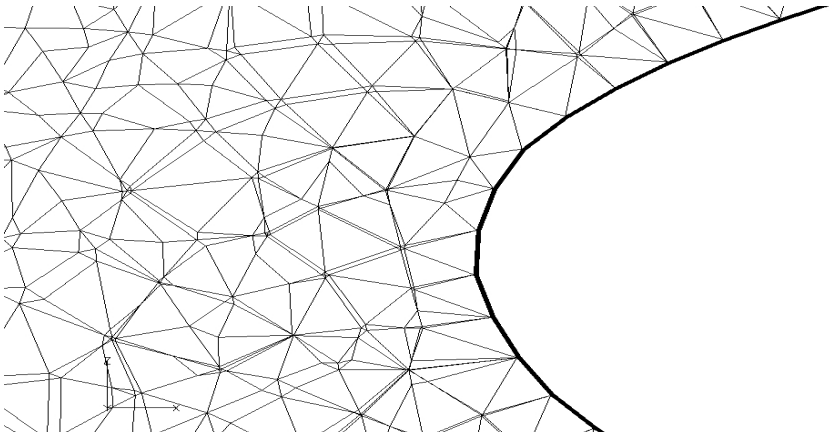

Figure 30: Viscous layers of third grid.

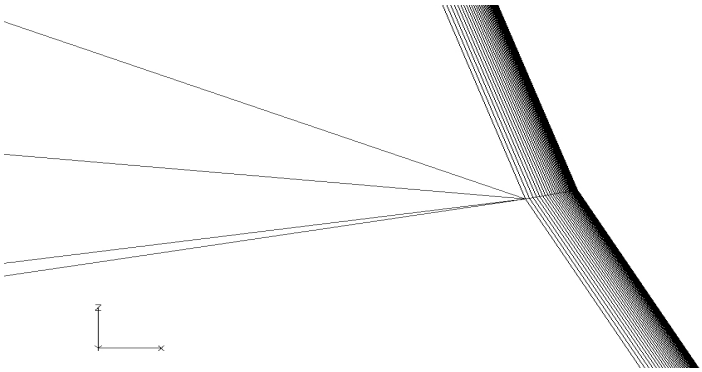

Figure 31: Closer look at viscous layers of third grid.

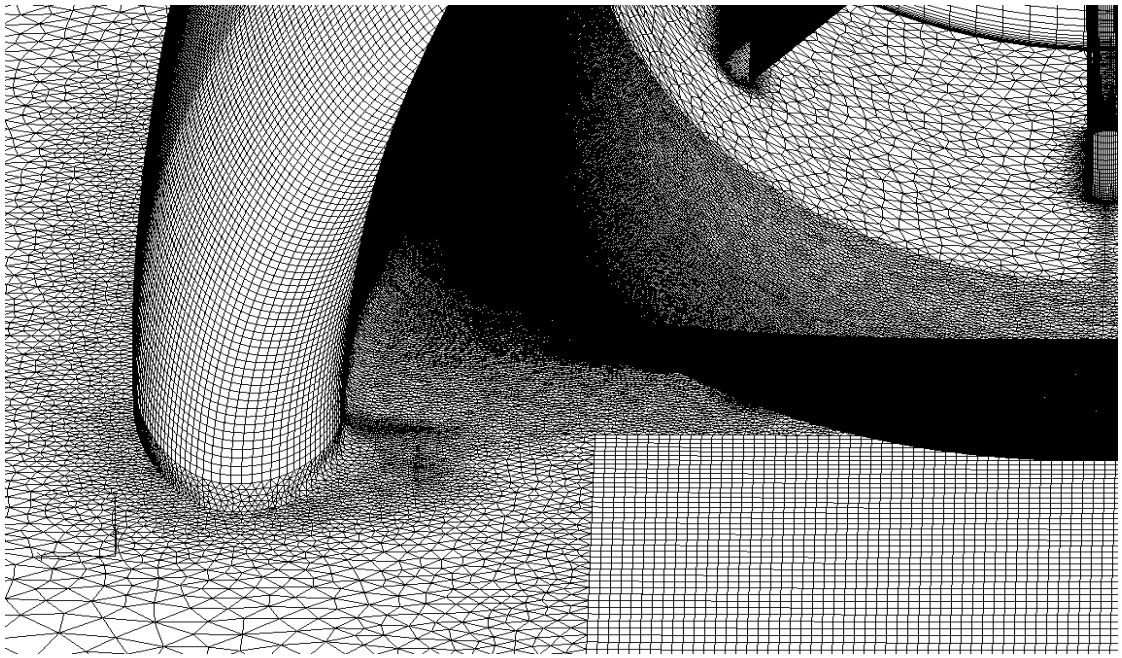

Figure 32: Third computational grid surface spacing.

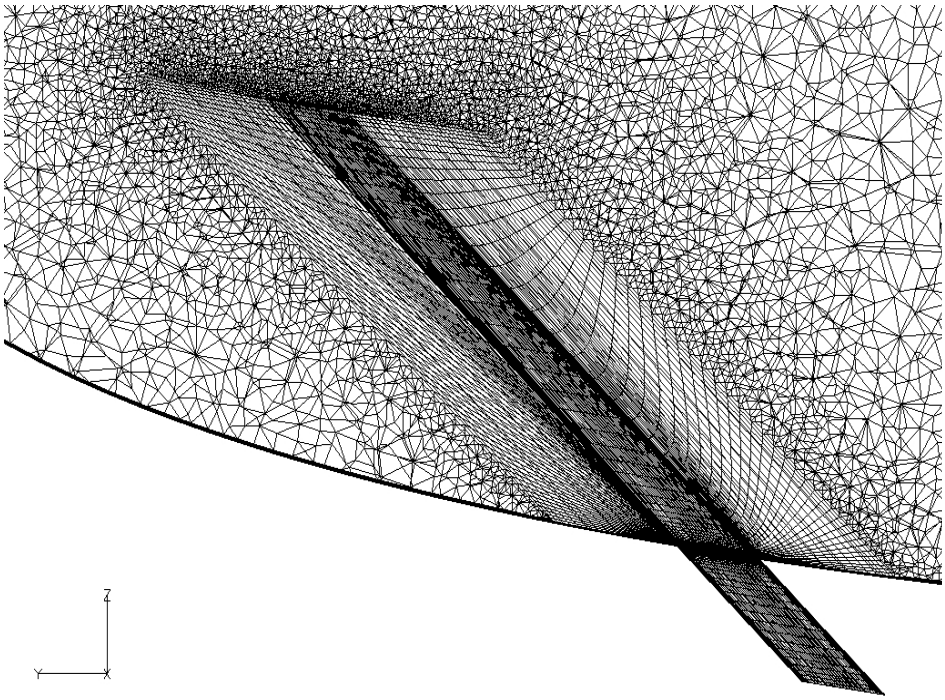

Figure 33: Single jet at the X=0.83 plane of third grid.

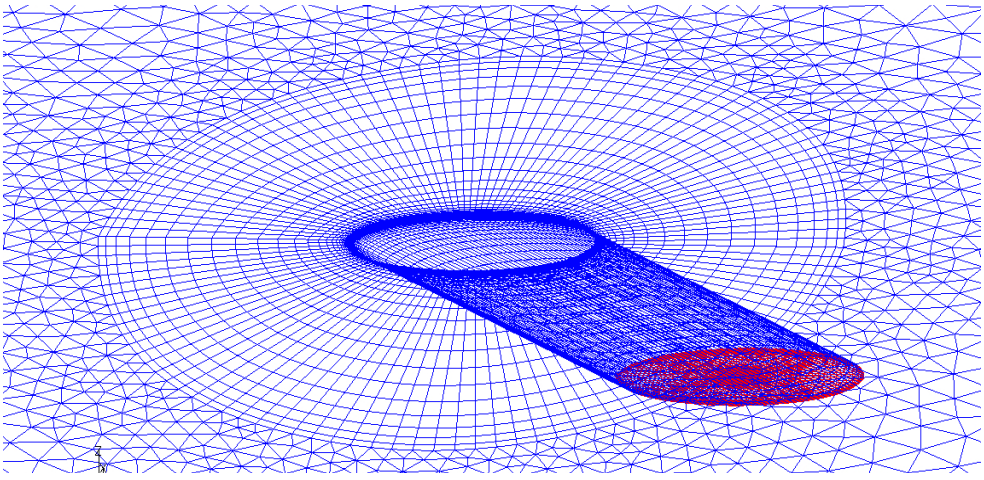

Figure 34: Structured grid at jet hole of third grid.

CHAPTER VI
Problem Setup and Implementation

In an effort to validate the numerical solution, the computational results are being compared to the experimental data recorded by Owens, Allan, and Gorton (2006): mass flow ratio, pressure readings along the upper and lower centerlines of the duct, and circumferential distortion at the aerodynamic interface plane (AIP). It is also important that the numerical solution show similar flow characteristics to those of S-duct flows. Flow parameters for the jets were specified in accordance with experimental values found in Owens' Microsoft Excel sheet. A non-dimensional back pressure value, at the duct exit, was used to "throttle" the mass flow rate through the S-duct. Numerical pressure measurements for the 40 probe rake and S-duct centerlines were extracted from the computational results using the Fieldview post-processing software. Circumferential distortion calculations followed the SAE Aerospace Recommended Practice 1420 standard.(2002) This chapter covers further details of the implementation process. Topics include: validation criteria, boundary conditions, initial conditions, general simulation facts, and post processing.

A. Validation Criteria

It is important to set a list of criteria for achieving a valid numerical solution. Details on the procedures for acquiring the experimental data are documented in the journal article by Owens, Allan, and Gorton.(2008) Attempts at achieving valid numerical solutions were made by comparison with the following experimental data: mass flow ratio, pressure reading along the upper and lower centerlines of the duct, and circumferential distortion at the AIP. Test studies on the well documented M2129 S-duct

geometry provided insight into vorticity and secondary flow characteristics generated within a duct of this kind. Valid numerical solutions will need to show similar secondary flow characters as those of S-bend geometries like the M2129.

$$Mass\ \ Flow\ \ Ratio = \frac{MFR_{jets}}{MFR_{inlet}} \tag{6.A.1}$$

Recall the equation for mass flow ratio. Mass flow ratio is regulated by the boundary conditions specified at the duct exit and jet grid domains. For the "baseline" case where $MFR_{jets} = 0$ and mass flow ratio equals zero, the numerical inlet mass flow rate must agree with recorded experimental values. Fieldview's point probe and 2-D plot feature is used to extract numerical pressure measurements for the 40 probe rake and S-duct centerlines, respectively.

Inlet distortion calculations follow the SAE Aerospace Recommended 1420 Standard Practice.(2002) According to the SAE standard, distortion is the area weighted average of the pressure measurements recorded along eight, evenly spaced, circumferential rakes. Five pressure samples are taken at varying radial distances along each rake, providing a total of forty total pressure measurements. For the "Inlet-A" duct exit radius of 1.224 inches, the five rings are set to radial distances of 0.274, 0.660, 0.861, 1.021, and 1.159 inches. Immediately following is an image of the AIP pressure rake.

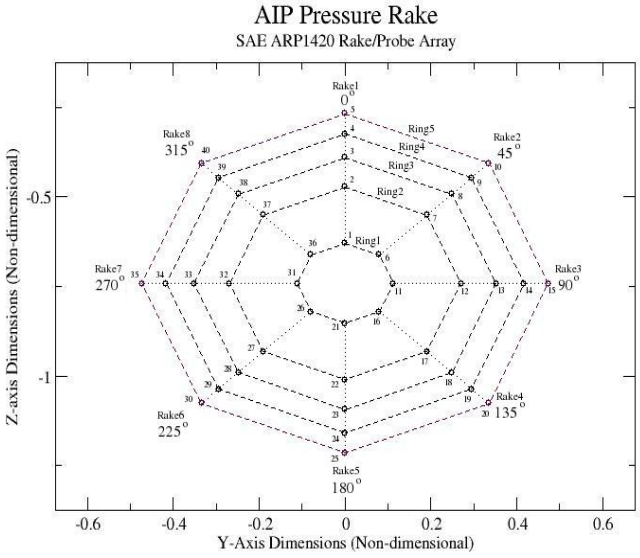

Figure 35. 1420 SAE standard coordinates for AIP plane

Equations 6.A.2 through 6.A.5 are the governing equations for calculating distortion $DCPC_{avg}$ at the AIP as described in the SAE standard.

$$DPCP_{avg} = 1/N_{rings} \sum_{i=1-5} intensity_i \tag{6.A.2}$$

where i is the radial ring number on the AIP rake, and N_{rings} denoting the total number of rings.

$$intensity_i = (PAV_i - PAVLOW_i)/PAV_i \tag{6.A.3}$$

$$PAV_i = \frac{1}{360}\int_0^{360} P(\theta)_i \, d\theta \text{ (ring average pressure)} \tag{6.A.4}$$

The total pressure function $P(\theta)_i$ is a linear curve. The upper and lower limits of the integration are 0 and 360, respectively.

$$PAVLOW_i = \frac{1}{extent_i}\int P(\theta)_i \, d\theta \text{ (Average low Pressure)} \tag{6.A.5}$$

$extent_i$ is defined as the radial region of pressure below PAV_i.

Again, Fieldview's point probe feature was used to extract the forty total pressure measurements. A C-language post-processing code was used to implement equations 6.A.2 through 6.A.5. In concordance with the SAE standard, circumferential distortion figures for a one-per-rev pattern were generated using the post-processing code. Single ring plots for each numerical test case can be seen in Appendix-C.

B. Boundary Conditions and Initial Conditions

The previous numerical work by Sreenivas and Sawyer (2008) followed initial conditions documented in numerical simulations by Allan and Owens.(2006) Allan's free stream conditions consisted of a Mach number equal to 0.877 and Reynolds numbers, Re_D , ranging from 1.8 to 3.8 million. The present numerical study of the R094 test case took free stream values of $Re_D = 1.8 \cdot 10^6$ and $M = 0.877$. The pressure and temperature readings were set to agree with experimental measurements reported by Owens, Allan, and Gorton.(2006) Total temperature, T_t , and total pressure, P_t , were set to 80 degrees Fahrenheit and 30 pounds per square inch, respectively. Fluid flow through the jets were documented to be 70 degrees Fahrenheit. A private communication with Dr. Owens (2009) was conducted to obtain more guidance in the areas of initial and boundary conditions. It was discussed that the recorded jet pressure measurement of 25 psi. was too high, and a jet pressure of 20.5 psi would be a more accurate estimate of the pressure at the jet hole edge.

Now that the reference values are known, the next step is to non-dimensionalize the flow parameters. The length scale is normalized with respect to the duct exit diameter of 2.448 inches. Static pressure, density, and temperature values were calculated by using the Isentropic flow relations. Using equations 6.B.1 through 6.B.3 , the resulting static values for the free stream and jets were specified in the initial and boundary conditions.

$$\frac{T_t}{T_s} = 1 + \frac{\gamma - 1}{2} M^2 \tag{6.B.1}$$

$$\frac{P_t}{P_s} = (1 + \frac{\gamma - 1}{2} M^2)^{\frac{\gamma}{\gamma - 1}} \tag{6.B.2}$$

$$\frac{\rho_t}{\rho_s} = (1 + \frac{\gamma - 1}{2} M^2)^{\frac{1}{\gamma - 1}} \tag{6.B.3}$$

Shown below is a list of known values.

$M_r = 0.877$ = reference mach

$P_t = 30$ = total pressure (psi.)

$T_t = 80$ = total temperature (degrees Fahrenheit)

$P_{jet} = 20.5$ = jet pressure (psi.)

$T_{jet} = 70$ = jet temperature (degrees Fahrenheit)

The reference speed of sound and density are set to be their corresponding free stream static values.

$$a_r = a_s \quad , \quad \rho_r = \rho_s \tag{6.B.4}$$

Speed of sound is calculated by:

$$a_r = a_s = \sqrt{(\gamma R T_s)} \tag{6.B.5}$$

where R is the gas constant, and static temperature, T_s , is calculated by rearranging equation 6.B.1. Recall the specific heat ratio, γ , for air is approximately 1.4. The ideal gas law is used to calculate a reference density value.

$$\rho_r = \rho_s = \frac{P_s}{R T_s} \tag{6.B.6}$$

Static temperature and static pressure were obtained from equation 6.B.1 and 6.B.2, respectively. Reference velocity, U_r , is obtained by the following equation.

$$U_r = M_r a_r \tag{6.B.7}$$

Non-dimensional static pressure, $\hat{P}_s$, is calculated by using either equation 6.B.8 or 6.B.9.

$$\hat{P}_s = \frac{P_s}{\rho_r U_r^2} - \frac{1}{\gamma M_r^2} \quad \text{(Variable-Mach)} \tag{6.B.8}$$

$$\hat{P}_s = \frac{P_s}{\rho_r U_r^2} \quad \text{(compressible)} \tag{6.B.9}$$

Equation 6.B.9 is used to calculate non-dimensional pressure when running the "Tenasi"code in compressible mode, and equation 6.B.8 is used to calculate non-dimensional pressure while running variable-Mach mode. When running variable-Mach, a good check to see if the variables have been non-dimensionalized correctly is to insert P_r into P_s and see if equation 6.B.8 equals approximately zero. Thus the following is true when the flow parameters are non-dimensionalized correctly.

$$\frac{P_r}{\rho_r U_r^2} \approx \frac{1}{\gamma M_r^2}$$

Depending on which mode "Tenasi" is set to run, a non-dimensional jet pressure is calculated using either equation 6.B.8 or 6.B9 by plugging in P_{jet} into P_s . After solving for $\hat{P}_{jet}$, a non-dimensional jet density, $\hat{\rho}_{jet}$, is derived by the following equation.

$$\hat{\rho}_{jet} = \frac{\rho_{jet}}{\rho_r} \tag{6.B.10}$$

where

$$\rho_{jet} = \frac{P_{jet}}{RT_{jet}} \tag{6.B.11}$$

Equations 6.B.1 through 6.B.11 were implemented in a C-language program. Reading in all reference and jet values, the C-language code was able to rapidly generate boundary condition files for varying jet configurations and jet mass flow rates. The input file

included the jet hole specific velocity vectors for all 176 jets, allowing for flexibility in choosing a jet configuration. Once the jet configuration was selected and the number of jets were known, the program implemented the simplifying assumption that all jets had identical portions of the cumulative jet mass flow rate. Jet mass flow rates for each case were obtained from Owens' Microsoft Excel sheet.(2006) Immediately following is the equation used to equally divide up the jet mass flow rate.

$$MFR_{singlejet} = \frac{MFR_{jets}}{total\ number\ of\ jets} \tag{6.B.12}$$

Knowing jet density from equation 6.B.10, velocity magnitude was calculated by rearranging the mass flow rate equation.

$$MFR = \rho U A \tag{6.B.13}$$

$$U_{jet} = \frac{MFR_{singlejet}}{\rho_{jet} A_{singlejet}} \tag{6.B.14}$$

$A_{singlejet}$ is the cross-sectional area of a single jet. According to the engineering drawings by Ortega (2004), the jet hole diameter is specified to 0.04 inches. The jet velocity magnitude calculated in equation 6.B.14 was non-dimensionalized with respect to the reference velocity from equation 6.B.7.

$$\hat{U}_{jet} = \frac{U_{jet}}{U_r} \tag{6.B.15}$$

Non-dimensional jet velocity vectors were obtained by multiplying the non-dimensional velocity magnitude with the jet specific directional unit vectors. The simplifying assumption of evenly dividing the combined jet mass flow rate, with identical density and pressure values, is the ideal jet flow condition and does not necessarily represent reality. Seeking guidance to an alternative, a private communication was conducted with Dr. Owens (2009), discussing the validity of the simplifying assumption. With the limitations

of working with a 2.5% scale model of the "Inlet-A" geometry, it was not possible to obtain measurements to know the exact flow conditions located at the jet hole edges. Dr. Owens commented on the unlikelihood of identical flow through each of the 16 jets, but both parties agreed that this was a reasonable starting assumption. Thus, non-dimensional jet density (from equation 6.B.10), non-dimensional jet pressure (from equation 6.B.11), and non-dimensional jet velocity vectors were specified for each jet boundary condition.

Nodes lying on the solid surfaces, where fluid velocity is zero, were given viscous adiabatic boundary conditions. Solid surfaces include the flat plate, cowl, S-duct, and rake. In the case of the second and third computational grids, the side walls of the jet holes were set to viscous adiabatic boundary conditions. Farfield boundaries were set to maintain the free stream flow parameters. The S-duct exit domain was assigned a non-dimensional back pressure value. This back pressure value was used to "throttle" the numerical mass flow rate passing through the duct. An example of "throttling" the flow to match experimental inlet mass flow rate values is included in the results portion of this study.

By using a scaling factor ranging from 0 to 1, initial conditions for interior nodes were set to a percentage of the free stream flow parameters. A scaling factor of zero sets all flow variables at the interior nodes to zero. The disadvantage of using a scaling factor of zero is the number of iterations it takes to fill the vacuum-like interior domain. On the other hand, a scaling factor of one sets all flow variables at interior nodes to free stream conditions. The disadvantage for using a scaling factor of one is possible numerical stability issues for complex fluid flows and geometries. In the case of this research, the "Tenasi" solver remained stable while running a scaling factor of one for all flow cases, including cases with high jet velocities.

Allan's numerical study used the and Mentor SST turbulence models. (2006) The Mentor SST model was used in a few numerical simulations, but the Mentor one-equation showed better results in meeting the specified validation criteria. Thus, the Mentor one-equation was used as the preferred turbulence model through out this study. Turbulence modeling is discussed more in the results portion of this paper.

C. Computational Simulation Requirements

Available to all faculty and students, the UTC SimCenter maintains and operates a cluster consisting of 1300 processors. The first computational grid accumulated 6.5 million nodes. Standard practice suggests dividing computational grids into blocks containing approximately 150,000 nodes per processor. Grid decomposition and re-composition was made possible through an “in-house” code. The first computational grid was subdivided into 64 blocks. Taking up 64 processors on the cluster, the “Tenasi” flow solver would converge to a steady-state solution in approximately 8 hours. The second computational grid, being 30.5 million nodes, had to be decomped and simulated across 200 processors. Steady-state solutions for the second grid were obtained in about 24 hours. The third grid, consisting of 36.9 million nodes, was subdivided into 200 blocks. Though 200 processors did not meet the preferred 150,00 nodes per processor standard, it was limited to 200 to minimize traffic on the 1300 processor cluster. CFD simulations on the 36.9 million node grid are ongoing and run times for the grid have not been found at this time.

The flow solver's restart capabilities significantly reduced computational run times. Restarting from a steady-state solution, numerical simulations for different mass flow ratios could be calculated in approximately half the “dead start” times. For example, the R094 Pt. 771 “baseline” case took 8 hours to converge on the 6.5 million node grid.

Restarting from the Pt. 771 solution, the R094 Pt. 773 case converged in approximately 4 hours. This trend was also true for the second computational grid as simulations from restart files took 12 hours in comparison to the 24 hours of a “dead start” case run.

CHAPTER VII
Results

The objective of this research was to validate the "Tenasi" flow solver while gathering data on the effectiveness of using air jets as a flow control device. The validation criteria sought agreement between the numerical solutions and the following experimental data: mass flow ratio, pressure reading along the upper and lower center lines of the duct, and distortion at the aerodynamic interface plane (AIP). Boundary-layer ingestion (BLI) should remain at the required 35% boundary-layer to inlet ratio. This chapter is a summary of all computational results calculated for the 6.5 and 30.5 million node grids. Data for the 36.9 million node grid was not included due to time constraints.

A. 6.5 Million Node Grid

To begin the computational study, it was important to confirm the 35% boundary-layer to inlet height ratio. With an inlet throat height of approximately 1.7 inches, the boundary-layer height was expected to be close to 0.6 inches. Below is a graph showing one experimental boundary-layer and four computational boundary-layers.

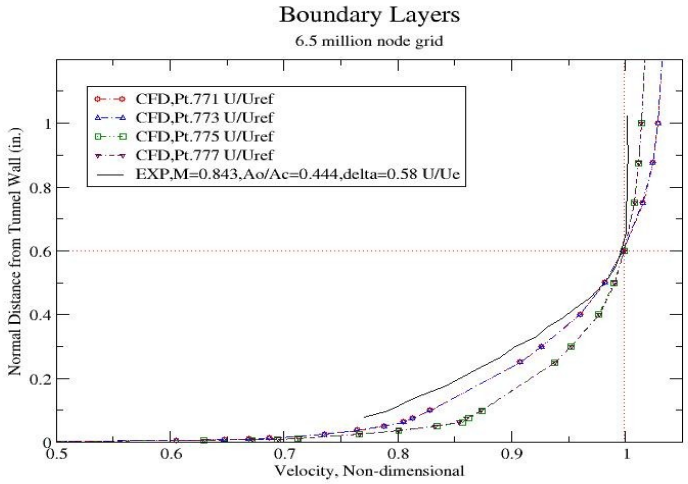

Figure 36: Boundary-Layers for R094 Pt. 771, 773, 775, and 777 case. (6.5M nodes)

NASA Langley's experimental research featured a 30 probe Pitot tube array. Yet, the vertical spacings, distances normal to the flat plate, for the 30 probe boundary-layer rake were not found in previous documentation. Berrier's 8 probe array provided the basis for the 20 point computational boundary-layer rake. Fieldview's point probe feature was used to measure the non-dimensional pressure values for the converged numerical solutions.

For this study, the boundary-layer height, δ , was determined by the height at which the non-dimensional velocity $U/U_{ref}=0.999$ which is shown in figure 36 by the dashed vertical line. The 35% boundary-layer to inlet height ratio, $\delta=0.6$ inches, is depicted in figure 36 by the dashed horizontal line. Note, the experimental boundary-layer was normalized with respect to U_e . Since no recorded experimental values for U_e were documented, the CFD boundary-layers are plotted according to their non-dimensional velocity values U/U_{ref} . With the dashed lines included, it is clearly evident that the boundary-layers for all four CFD solutions meet the 35% boundary-layer to inlet height ratio. By plotting the CFD results according to U/U_{ref} , one can see the "Tenasi" solver captures the boundary-layer overshoot common to flat plate simulations. Keep in mind, the location of the boundary-layer rake and the proximity of the tunnel walls directly influence the experimental boundary-layer measurements. The streamlines in figure 37 are colored with respect to local Mach number.

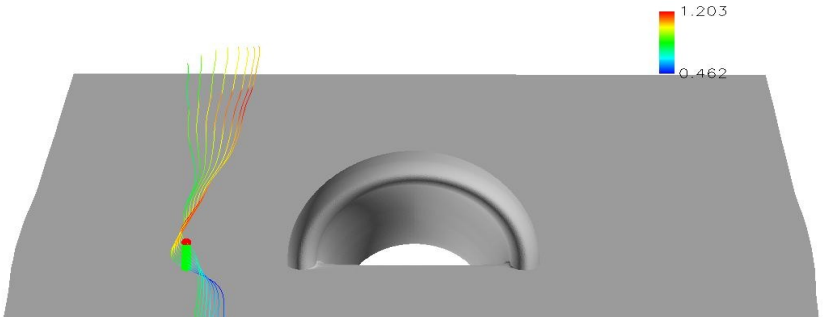

Figure 37: Boundary-Layer streamlines. (tunnel grid)

Notice in figure 37 that the tunnel wall width varies along the length of the tunnel. The walls bend with the local streamlines in a fashion similar to adaptive tunnel wall techniques. Recall length scale is non-dimensionalized according to the duct exit diameter. As seen in figure 37, the tunnel walls appear to be a couple exit diameters in the positive and negative Y-directions. The close vicinity of the walls affect the velocity of the flow downstream. Shown below is a comparison of the boundary-layer streamlines for the grid featuring the tunnel walls and the 6.5 million node grid featuring farfield outer boundaries.

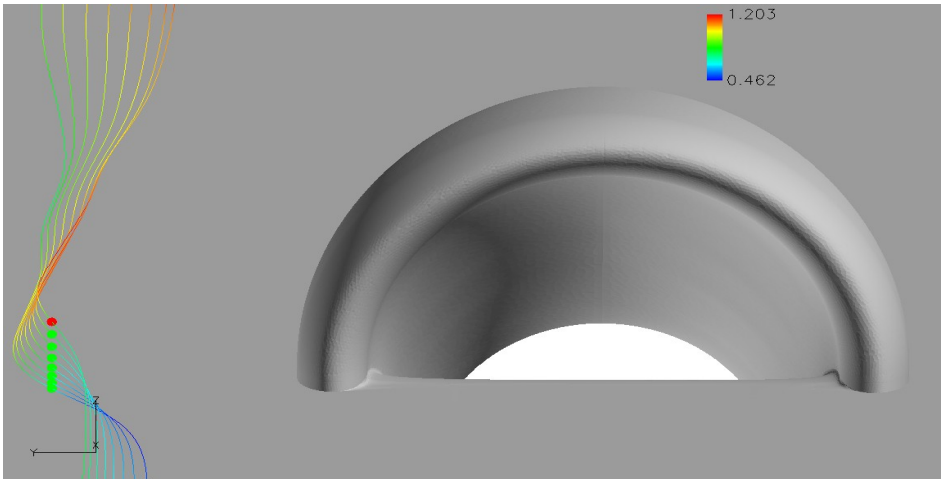

Figure 38: Boundary-Layer streamlines.(tunnel grid)

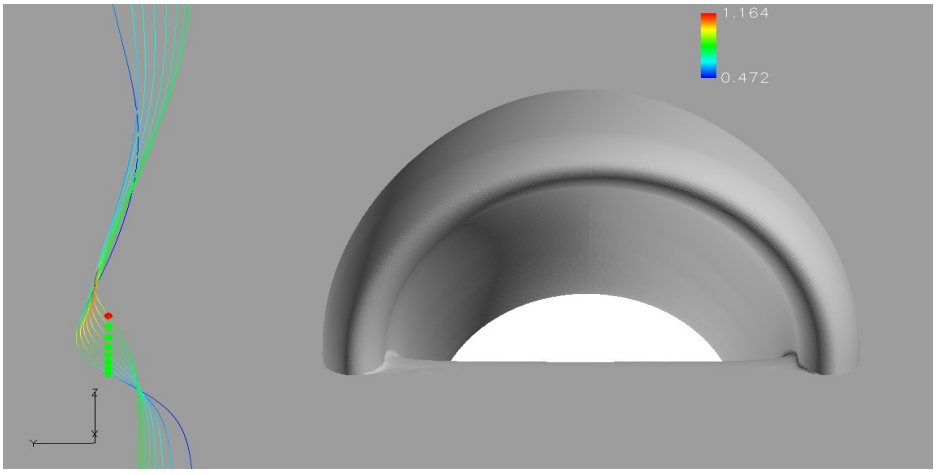

Figure 39: Boundary-Layer streamlines R094 Pt. 771.(6.5M node grid)

Figures 38 and 39 have streamlines passing through Berrier's 8 probe boundary-layer rake. Again, the streamlines are colored with respect to local Mach number. The maximum Mach number for Figures 38 and 39 are 1.203 and 1.164, respectively. Notice in figure 38, the streamlines disperse in the Y-direction and appear to fan out. From figure 39, one can see the farfield boundaries result in a more intuitive streamline flow pattern because the streamlines follow the profile and shape of the cowl. Also notice in figure 39, the region of higher Mach flow is smaller in regards to its length in the X-direction when compared to figure 38. According to the mass conservation equation, the close vicinity of the walls would cause the flow to speed up around the cowl to meet the over all tunnel mass flow rate. This effect can be seen by the presence of two shocks which form on and aft of the cowl. Figure 14 shows a numerical solution for the grid feature the tunnel walls.

In figure 36, the Pt. 771 and Pt. 773 solutions have a larger boundary-layer overshoot, a non-dimensional velocity greater than one, than the higher jet mass flow rate cases (Pt. 775 and Pt. 777). The difference in boundary-layers could be evidence that the boundary-layer rake is positioned too close to the cowl. As a result, the cowl shock could contaminate the boundary-layer measurements. Figures 40 through 42 are three pictures showing the flow characteristics around the cowl lip. The twelve streamlines span evenly from the first boundary-layer point in Berrier's 8 probe rake (-0.37, 1.546, 0.0139) to the corresponding point at the Y-axis symmetry plane (-0.37, 0.0, 0.0139). Streamlines in figures 40, 41, and 42 are again colored with respect to local Mach number.

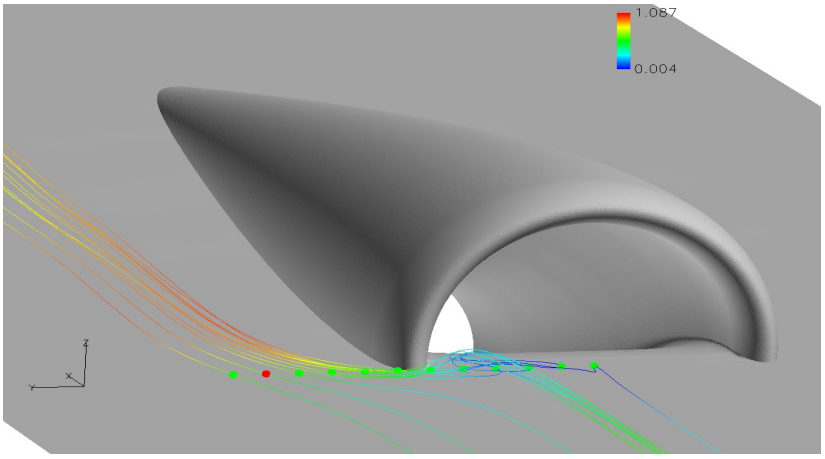

Figure 40: Streamlines around cowl.(tunnel grid)

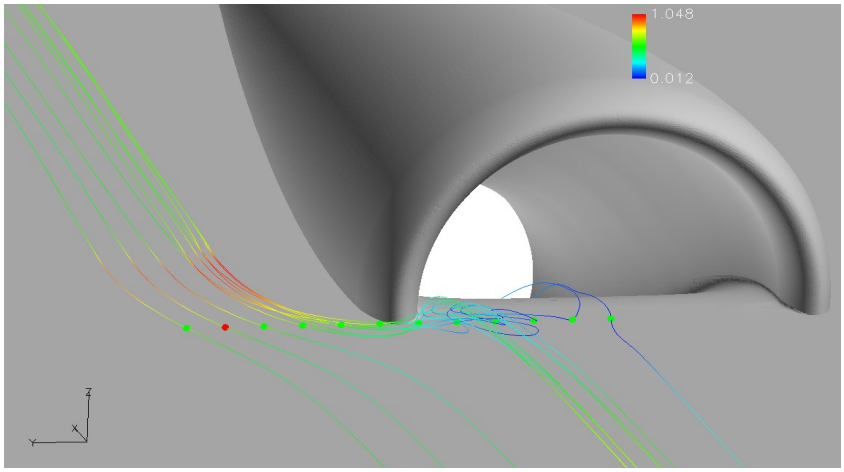

Figure 41: Streamlines around cowl, R094 Pt. 771.(6.5M node grid)

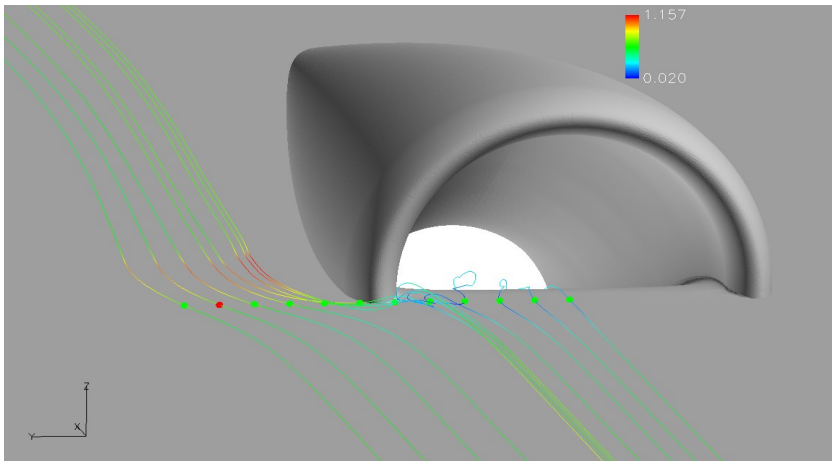

Figure 42: Streamlines around cowl, R094 Pt. 777.(6.5M node grid)

In the case of the tunnel grid seen in figure 40, none of the twelve streamlines enter the S-duct. The maximum local Mach number for the tunnel grid equals 1.087. Again, one can see the region of high Mach flow extends farther downstream with the inclusion of the tunnel walls. In figure 41, the Pt. 771 case has a maximum local mach number of 1.048. Notice in figure 41 and 42, the Pt. 771 case has two streamlines entering the S-duct while the Pt. 777 case calculated four streamlines entering the S-duct. The increased number of streamlines entering the S-duct reveals that the air jet flow control devices have a noticeable affect on the fluid flow upstream. The experimental Pt. 777 case reported less mass flow passing through the duct than the Pt. 771 case. The increased back pressure enforced at the duct exit results in more mass traveling around the cowl. Thus for the Pt. 777 case, the local maximum mach number rises slightly to 1.157.

The next step is to clarify the meaning of using a non-dimensional back pressure value to throttle the flow through the S-duct. Table 2 shows the iterative process of honing in on the experimental mass flow rate. Iteratively stepping towards the experimental mass flow rate yielded the following results for the R094 Pt. 771 "baseline" case. Recall, the "baseline" case has a jet mass flow rate of zero. As a result, emphasis was place on matching the experimental inlet mass flow rate, $MFR_{inlet} = 2.073\ lbm/sec$.

Table 2: Case R094 Pt. 771 Throttling Technique.(6.5M nodes)

Non-dimensional Back Pressure (duct exit domain)	**Inlet Mass Flow Rate (lbm/sec)**	**Pressure Recovery** Pt_2/Pt_∞	**Distortion coefficient** $DpCp_{avg}$
0.32	1.9535	0.9322	0.0509
0.30	2.0593	0.9337	0.0556
0.29	2.1089	0.9342	0.0561

Notice in table 2, a non-dimensional back pressure of 0.30 provided an adequate inlet mass flow rate. The accuracy of the numerical inlet mass flow rate could be improved by continuing to iteratively search beyond two decimal digits. Due to solution run times, the non-dimensional back pressure was limited to two decimal places. The experimental circumferential distortion, documented in Owens' Excel sheet (2006), reported a $DpCp_{avg} = 0.0555$ for the "baseline" case. Note for a back pressure of 0.30, the numerical distortion coefficient was 0.0556 which is within the experimental tolerance of $\pm$ 0.001. Thus, a non-dimensional back pressure out to two decimal places is adequate within experimental tolerances. The pressure recovery for each back pressure case was lower than the corresponding experimental value of 0.949. At this point, the reason for this disagreement is not known. These results suggest that there is a significant amount of numerical loss in the system, since the pressure recovery is lower than expected. Matching well with inlet mass flow rate and distortion values, figure 43 shows a comparison of pressure readings along the upper and lower centerlines of the S-duct surface.

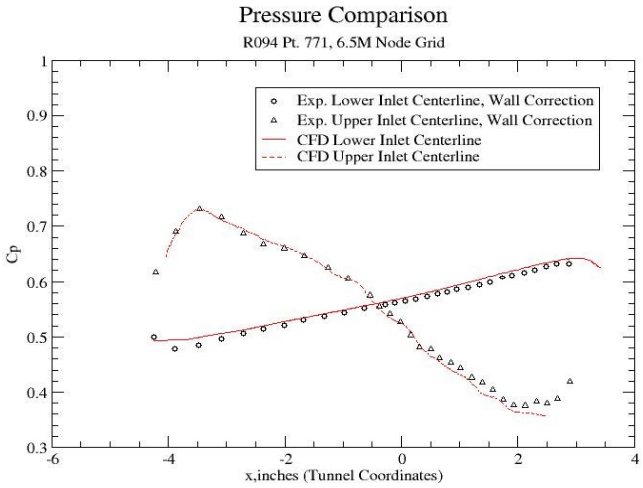

Figure 43: Experimental vs. CFD Centerline pressure Comparison for Pt. 771 case.(6.5M nodes)

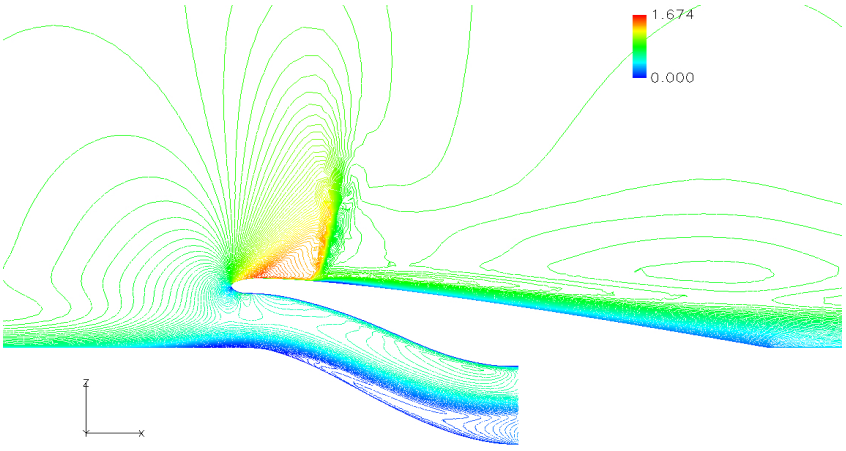

Figure 44: Mach number contour plot for Pt. 771 case at y/L= 0.0 plane. (6.5M nodes)

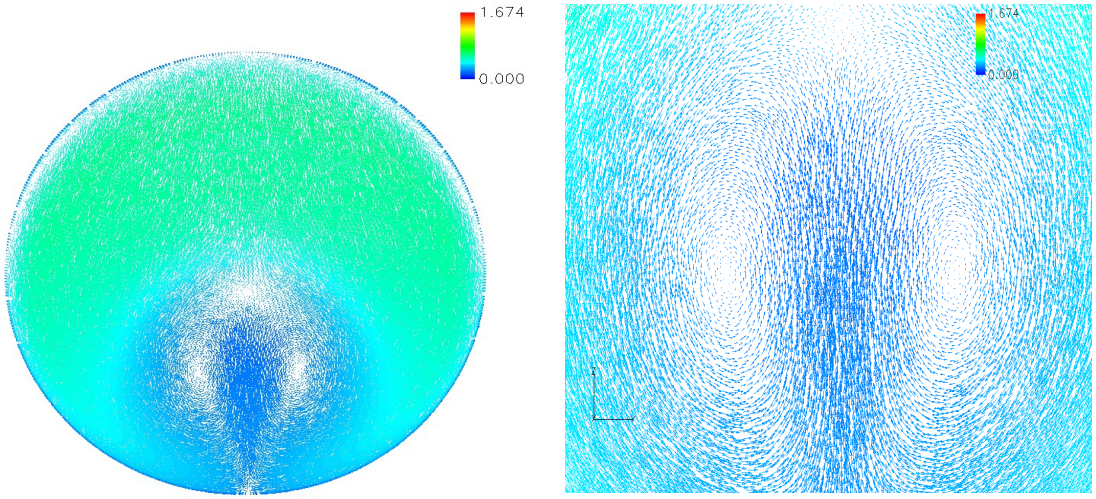

Figure 45:(left)Secondary flow vectors for Pt. 771 case at AIP. (6.5M nodes)

Figure 46:(right) Closer image of secondary flow vectors for Pt. 771 case at AIP. (6.5M nodes)

Figure 44 is a contour plot of Mach number at the Y=0.0 plane. Figures 45 and 46 show the secondary flow vectors at the AIP. Vectors are colored with respect to Mach number. The secondary flow descends down the side walls, impacts in the middle, and shoots upward resulting in two counter-rotating vortices. The left vortex rotates counter-clockwise while the right rotates clockwise. As seen in figures 45 and 46, the Pt. 771 numerical solution shows similar secondary flow characteristics common to S-duct geometries with no flow control devices.

Checking the numerical solution with regards to the validation criteria, the numerical solution for the Pt. 771 “baseline” case agreed well with the experimental values for inlet mass flow rate, distortion at the fan-face location, and pressure readings along the centerlines. Results also showed similar flow characteristics and vorticity trends common to S-bend type fluid flows. Satisfied with the baseline results, it was time to run cases including the air jet flow control devices. By changing the boundary conditions of the jet domains, numerous jet mass flow rate cases were tested in rapid succession. The steady-state “baseline” solution was used as a restart file to minimize simulation run times. Table 3 shows computational results for the R094 Pt. 771 , Pt. 773, Pt. 775 and pt777. The “baseline” Pt. 771 was included for quick comparison between other flow cases.

Table 3: Experimental vs. CFD for Pt. 771, Pt. 773, Pt. 775 and Pt. 777 case.(6.5M nodes)

note: Owens' and Allan's experimental data are listed in parenthesis.

Case	**Inlet Mass Flow Rate (lbm/sec)**	**Mass Flow Ratio** $\frac{MFR_{jets}}{MFR_{inlet}}$	**Pressure Recovery** Pt_2 / Pt_∞	**Distortion coefficient** $DPCP_{avg}$
R094 Pt. 771 “Baseline”	2.0593 (2.0730)	0.00000 (0.00000)	0.9337 (0.9490)	0.0556 (0.0555)
R094 Pt.773	2.0765 (2.0720)	0.00385 (0.00386)	0.9328 (0.9480)	0.0576 (0.0579)
R094 Pt.775	2.0885 (2.0670)	0.00718 (0.00726)	0.9427 (0.9480)	0.0361 (0.0487)
R094 Pt.777	2.0925 (2.0700)	0.01099 (0.01111)	0.9342 (0.9450)	0.0186 (0.0322)

Recall, the equation for mass flow ratio (6.A.1).

$$Mass\,Flow\,Ratio = \frac{MFR_{jets}}{MFR_{inlet}} \qquad (7.A.1)$$

For the "baseline" case where $MFR_{jet}=0$, the numerator is a constant. The back pressure was varied to match the experimental inlet mass flow rate because the mass flow ratio equals zero for the "baseline" case. While implementing the use of the flow control devices, the numerator is constant but not equal to zero. The non-dimensional back pressure value throttles the inlet mass flow rate (denominator) to achieve the necessary experimental mass flow ratio.

Notice, the pressure recovery values continue to disagree with Owens' experimental values.(2006) It is interesting to note that the difference between numerical and experimental pressure recover values decreases as the jet mass flow rate increases. Numerical research by Allan (2006) documents a similar trend of lower pressure recovery values that get better with the higher jet mass flow rate cases. Like the numerical data presented by Allan, the reason for this pressure recovery trend is unknown.

Seeking another valid solution, case R094 Pt.773 shows good agreement with the experimental mass flow ratio and distortion coefficient values. Figure 47 shows that the numerical pressure measurements along the centerline correspond well with the Pt. 773 experimental values.

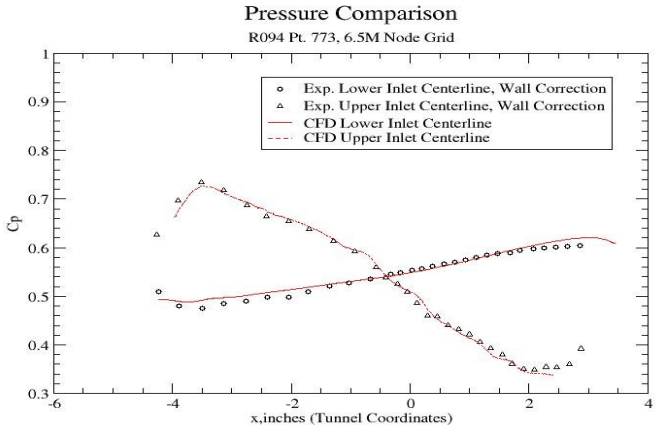

Figure 47: Experimental vs. CFD pressure centerline comparison for Pt. 773 case.(6.5M nodes)

A contour plot and a secondary flow vector plot for the Pt. 773 case are found in Figure 48 and 50, respectively. Again, the plots are colored according to Mach number. In regards to the validation criteria, the R094 Pt. 773 case showed satisfactory agreement with the experimental mass flow ratio, distortion, and centerline pressure values while showing familiar vorticity trends. At this point, two valid numerical solutions for the two lower jet mass flow rate cases have been obtained.

Before looking at the higher jet mass flow rate cases, note experimental centerline pressure values could not be found for cases beyond Pt. 773. Thus, numerical centerline pressure values for the Pt. 775 and Pt. 777 cases are not included in this report. Notice in table 3, the computational distortion values began to diverge from experimental data between the R094 Pt.773 and R094 Pt.775 cases. After comparing the two computational solutions, it was discovered that the two cases had drastically different secondary flow characteristics at the AIP. The difference between the computational and experimental values confirmed that circumferential distortion is highly influenced by the air jet flow control devices. Numerical and experimental distortion values continued to diverge for the higher jet mass flow rates above Pt. 775. The exact reason for the noticeable difference between computational and experimental $DpCp_{avg}$ values is not known at this time. It is suspected that the assumption of equally divided and uniform flow conditions at the jet boundary conditions (mass flow, velocity and their inherent influence of jet momentum) produces error that continues to escalate in correlation with the increase in jet mass flow rate. The methodology of rendering the jet holes as a grid domain was another possible cause of the discrepancies. Oval grid domains located on the S-duct surface behaved numerically as a step function. Constant and uniform velocity vectors across the entire jet hole does not reproduce the same velocity profile as fluid

passing through a tube and out a jet nozzle. In retrospect, it is not surprising the jet hole boundary conditions overpower the vorticity formed within the S-duct, resulting in considerably lower distortion values. This grid concern was kept in mind during the construction of the second computational grid. Figures 48 and 49 show the primary flow through the inlet for the Pt. 773 and Pt. 775 case, respectively. Figures 50 and 51 show the secondary flow vectors at the AIP. Figures 48 through 51 are colored with respect to Mach number.

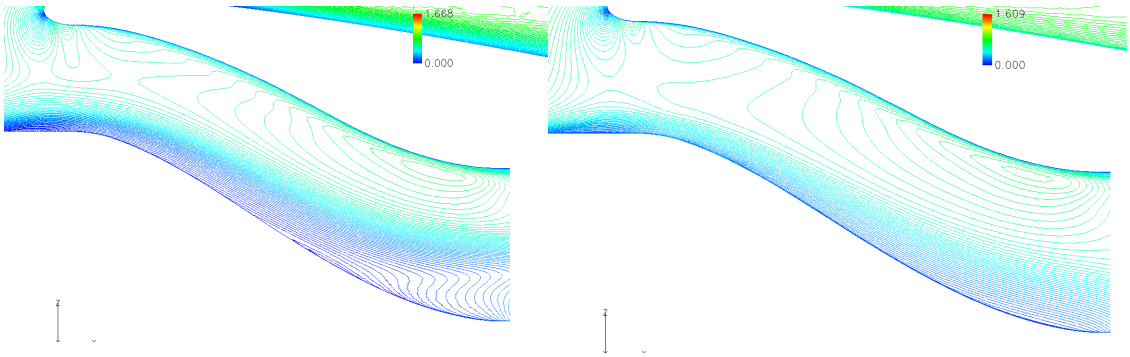

Figure 48:(left) Mach number contour plot for R094 Pt. 773 case at y/L = 0.0 plane.(6.5M nodes)

Figure 49:(right) Mach number contour plot for R094 Pt. 775 case at y/L = 0.0 plane.(6.5M nodes)

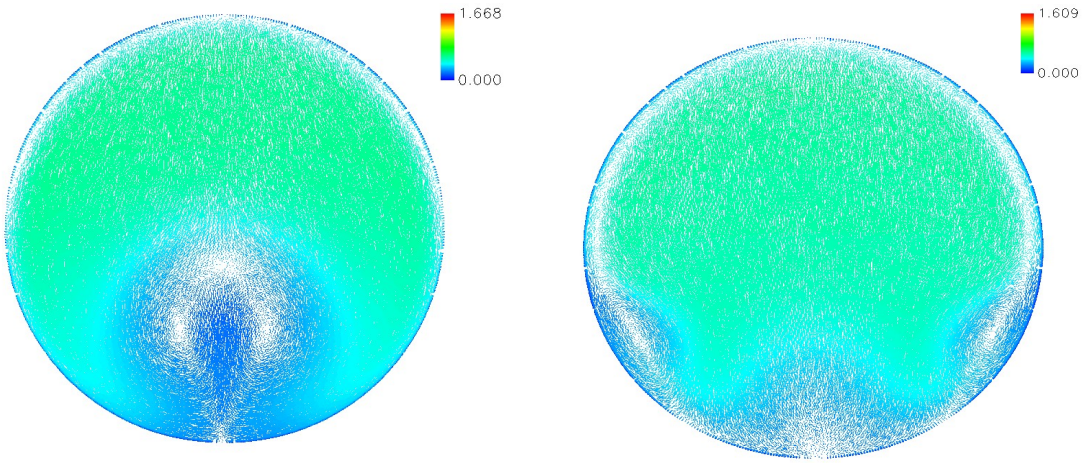

Figure 50:(left) Secondary flow vectors for R094 Pt. 773 case at AIP.(6.5M nodes)

Figure 51:(right) Secondary flow vectors for R094 Pt. 775 case at AIP.(6.5M nodes)

From figures 48 and 49, one can see a slight height difference in the low pressure regions. The temptation is to assume that the jets reduce the size of the counter rotating vortices seen in the Pt. 771 and Pt. 773 cases. Figures 50 and 51 show a transition in the secondary flow physics due to increasing the jet mass flow rate. Similar to the "baseline" numerical solutions, the secondary flow of in the R094 Pt.773 case (figure 50) descends down the side walls, impacts in the middle, and causes the flow to shoot upward in the positive Z-axis direction. Thus, two counter-rotating vortices form. The left vortex rotates counter-clockwise and the right vortex rotates clockwise. For the R094 Pt.775 case (figure 51), the counter-rotating vortices have been split down the middle. In this case, the downward fluid flow forces the counter rotating vortices towards the side walls. Interestingly, the left vortex rolls up in a clockwise direction while the right vortex rotates counter-clockwise, which is opposite to the vortex rotation found in the "baseline" Pt. 771 and Pt. 773 cases.

The vast difference in secondary flow raised concerns about the Menter one-equation turbulence model. In agreement with the turbulence model used by Allan and Owens (2006), the simulations were repeated using the Menter SST turbulence model. The Menter SST numerical solutions calculated lower distortion coefficient values for all cases, including the "baseline" Pt. 771 case. Though the SST turbulence model noticeably affected the solution, the numerical solutions were less accurate than the Mentor one-equation simulations. Knowing the boundary conditions have a significant influence on the fluid flow, it was decided to stick with the Menter one-equation for the rest of this computational research.

To further test the grid's adequacy, the mass conservation within the S-duct was checked for each of the mass flow ratio cases. Error calculations between experimental and numerical values follow the equation listed below.

$$percent\ error = \frac{|experimental - numerical|}{experimental} \times 100 \qquad (7.A.2)$$

Table 4: Mass conservation within S-duct.(6.5M nodes)

note: Owens' and Allan's experimental data are listed in parenthesis.

Case	Inlet Mass Flow Rate (lbm/sec)	% Error	Mass Flow Ratio	% Error	Exit Mass Flow Rate (lbm/sec)	% Error	% numerical loss
R094 Pt.771	2.0593 (2.0730)	0.660	0.00000 (0.00000)	0.000	2.0323 (2.0730)	1.964	1.311
R094 Pt.773	2.0765 (2.0720)	0.215	0.00385 (0.00386)	0.215	2.0543 (2.0759)	1.038	1.468
R094 Pt.775	2.0885 (2.0670)	1.039	0.00718 (0.00726)	1.028	2.0723 (2.0743)	1.092	1.502
R094 Pt.777	2.0925 (2.0700)	1.085	0.01099 (0.01111)	1.073	2.0828 (2.0811)	0.082	1.568

Experimental exit mass flow rate was calculated the following way.

$$MFR_{inlet} + MFR_{jets} = MFR_{exit} \qquad (7.A.3)$$

Error percentages might have been improved by continuing to iteratively search for the correct non-dimensional back pressure value declared at the duct exit. Recall, table 2 showed iterative “throttling” process. The error recorded in table 4 might have been decreased if the back pressure search carried on beyond two decimal digits. Knowing this technique would be time consuming, a more brute force search was considered for simulations on the 30.5M node grid.

Looking at the error percentages only, one might say there is acceptable agreement between experimental and numerical mass flow rate values. Located in the right most column of table 4, numerical loss is error associated with mass conservation, mass flow in equals mass flow out. These error percentages reveal significant amounts of numerical mass conservation losses within the S-duct. These losses were thought to be a result of course element spacings along the surface of the S-duct. With a pure unstructured mesh, a rendered surface geometry is directly dependent on the number of nodes making up a connector. For example, one can imagine the geometry truncation when trying to render a circle with just 10 nodes verses 100 nodes. Geometry truncation, due to the connectors, only grows when expanding to a grid domain and block. The numerical loss seen in mass flow rate could be causing further losses affecting circumferential distortion. If insufficient connector spacings propagated into inadequate volume spacings, the grid could, in effect, be damping and dissipating vorticity within the S-duct. Numerical losses in the secondary flow could directly impact the accuracy of the computational distortion values. For the second computational grid, element and node counts were increased to better resolve the complex geometric transition from the semi-circle inlet to the full circle exit.

Post-processing figures and tables for the Pt. 771, 773, 775, and 777 cases are included in Appendix-C. As mentioned in the Chapter 5, a higher node count and more realistic solid model were part of the main revisions implemented in the second computational grid. Before concluding the case study on the 6.5 million node grid, it is helpful to see error percentages for the pressure recovery and distortion values. Table 5 lists the error percentages of test cases run on the 6.5 million node grid.

Table 5: Error percentages for pressure recover and distortion.(6.5M nodes)

note: Owens' and Allan's experimental data are listed in parenthesis.

Case	Pressure Recovery Pt_2 / Pt_∞	% Error	Distortion coefficient $DPCP_{avg}$	% Error
R094 Pt. 771 "Baseline"	0.9337 (0.9490)	1.615	0.0556 (0.0555)	0.178
R094 Pt.773	0.9328 (0.9480)	1.604	0.0576 (0.0579)	0.451
R094 Pt.775	0.9427 (0.9480)	0.564	0.0361 (0.0487)	25.895
R094 Pt.777	0.9342 (0.9450)	1.147	0.0186 (0.0322)	42.286

B. 30.5 Million Node Grid

As before, we begin by examining the 35% boundary-layer to inlet height ratio. The dashed horizontal line, $\delta = 0.6$ inches ,and dashed vertical line, $U/U_{ref} = 0.999$, are included in figure 52 for quick assessment of the four computational boundary layers. Like figure 36, the experimental boundary-layer is normalized with regard to U_e . The computational results are left in their non-dimensional form, $U/Uref$. The dashed lines make it clear to see that the numerical boundary-layers meet the 35% height ratio.

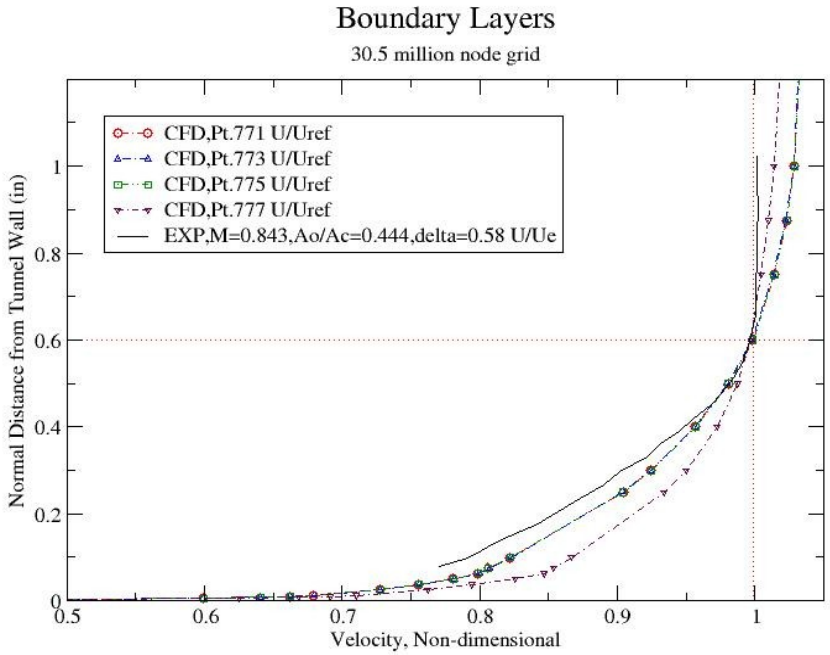

Figure 52: Boundary-Layers for R094 Pt. 771, 773, 775, and 777 case.(30.5M nodes)

Again, the boundary-layer overshoot of $U/U_{ref} = 1.033$ (Pt. 771, Pt. 773, and Pt. 775) and $U/U_{ref} = 1.019$ (Pt. 777) show common flow characteristics analogous to flat plat calculations. In comparison to the 6.5 million node grid, the 30.5 million node grid has three boundary-layers (Pt. 771, Pt. 773, and Pt. 775) converging to the profile closest to the experimental boundary-layer, having the larger overshoot. The difference in the Pt.

775 boundary-layers (6.5M vs. 30.5M) could be a result of the increased number of nodes inside and around the inlet.

While on this subject, let us see if the refined grid improved the numerical loss with respect to mass conservation within the S-duct. Calculations in table 6 for error and exit mass flow rate follow equations 7.A.2 and 7.A.3, respectively. Immediately, one can see the grid refinements have reduced the numerical loss. Like before, the non-dimensional back pressure was varied until the numerical mass flow ratio matched experimental values. Again, inlet mass flow rate was the experimental parameter used for the R094 Pt. 771 case.

Table 6: Mass conservation within S-duct.(30.5M nodes)

note: Owens' and Allan's experimental data are listed in parenthesis.

Case	Inlet Mass Flow Rate (lbm/sec)	% Error	Mass Flow Ratio	% Error	Exit Mass Flow Rate (lbm/sec)	% Error	% numerical loss
R094 Pt. 771	2.0745 (2.0730)	0.074	0.00000 (0.00000)	0.000	2.0746 (2.0730)	0.076	0.002
R094 Pt.773	2.0731 (2.0720)	0.052	0.00386 (0.00386)	0.052	2.0814 (2.0759)	0.267	0.016
R094 Pt.775	2.0636 (2.0670)	0.165	0.00727 (0.00726)	0.165	2.0781 (2.0743)	0.187	0.022
R094 Pt.777	1.9497 (2.0700)	5.812	0.01180 (0.01111)	6.170	1.9838 (2.0811)	4.678	0.557

Notice the large amount of error for the R094 Pt. 777 case. Non-dimensional back pressure values, accurate to two decimal places, were no longer adequate in matching the experimental mass flow rate values. As a result, back pressure was increased to four digit precision, iterating on quarter increments of ± 0.0025. This was done for the Pt. 771, 773,

and 775 cases. The Pt. 777 case was left with a back pressure accurate to two decimal places because the numerical distortion was considerably off from the experimental value. The time cost for iteratively searching to four decimal places might not be justifiable. The Pt. 771 case had very good agreement with a back pressure of 0.2700. For the Pt. 773 case, a back pressure of 0.2625 yielded the best mass flow ratio value. Likewise, Pt. 775 had a back pressure of 0.2600, and Pt. 777 was left at a back pressure of 0.33. Shown below are the CFD results for the 30.5 million node grid, and immediately following is a table of the error percentages.

Table 7: Experimental vs. CFD for Pt. 771, Pt. 773, Pt. 775 and Pt. 777 case.(30.5M nodes)

note: Owens' and Allan's experimental data are listed in parenthesis.

Case	**Inlet Mass Flow Rate (lbm/sec)**	**Mass Flow Ratio** $\frac{MFR_{jets}}{MFR_{inlet}}$	**Pressure Recovery** Pt_2 / Pt_∞	**Distortion coefficient** $DPCP_{avg}$
R094 Pt. 771 "Baseline"	2.0745 (2.0730)	0.00000 (0.00000)	0.9328 (0.9490)	0.0557 (0.0555)
R094 Pt.773	2.0731 (2.0720)	0.00386 (0.00386)	0.9304 (0.9480)	0.0592 (0.0579)
R094 Pt.775	2.0636 (2.0670)	0.00727 (0.00726)	0.9315 (0.9480)	0.0587 (0.0487)
R094 Pt.777	1.9497 (2.0700)	0.01180 (0.01111)	0.9492 (0.9450)	0.0244 (0.0322)

Table 8: Error percentages for pressure recover and distortion.(30.5M nodes)

note: Owens' and Allan's experimental data are listed in parenthesis.

Case	Pressure Recovery Pt_2 / Pt_∞	% Error	Distortion coefficient $DPCP_{avg}$	% Error
R094 Pt. 771 "Baseline"	0.93282 (0.9490)	1.705	0.0557 (0.0555)	0.328
R094 Pt.773	0.93038 (0.9480)	1.859	0.0592 (0.0579)	2.383
R094 Pt.775	0.93151 (0.9480)	1.740	0.0587 (0.0487)	20.456
R094 Pt.777	0.94920 (0.9450)	0.445	0.0244 (0.0322)	24.298

Like the 6.5 million node grid, the numerical solution does not match experimental pressure recovery values. However, the higher jet mass flow (Pt. 775 and Pt. 777) cases show better agreement than the low jet mass flow cases (Pt. 771 and Pt. 773). Again, this pressure recovery trend was seen in previous numerical work by Allan and Owens (2006), but the reason for the discrepancies is still unknown.

Let us continue by checking the "baseline" case with respect to the validation criteria. Table 7 confirms that the numerical solution agrees with the experimental inlet mass flow rate and experimental distortion values. A comparison of centerline pressure readings is presented in figure 53. Figure 54 shows the primary flow through the S-duct. Figures 55 and 56 show the secondary flow at the AIP. Figures 53 through 56 are colored with respect to mach number.

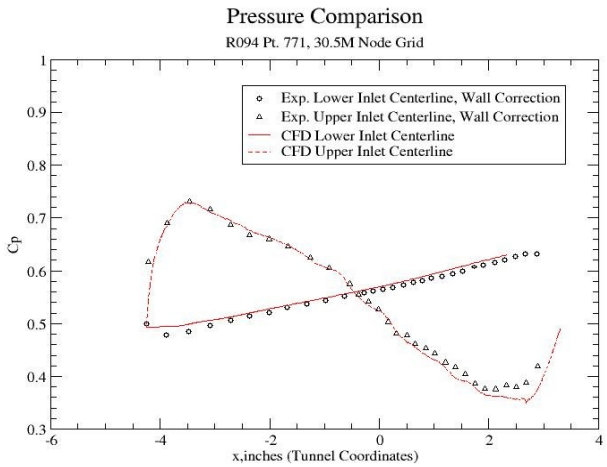

Figure 53: Experimental vs. CFD Centerline pressure Comparison for Pt. 771 case.(30.5M nodes)

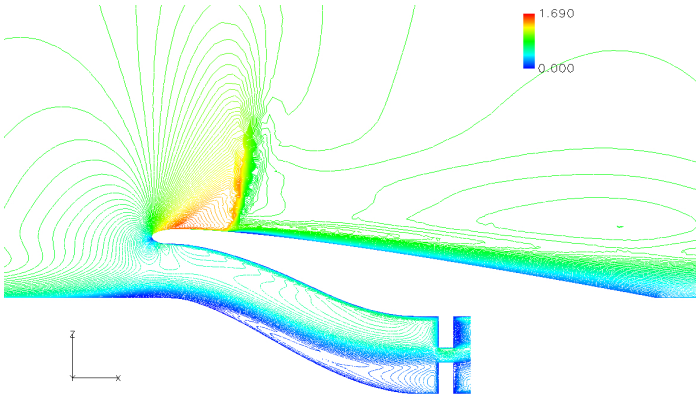

Figure 54: Mach number contour plot for Pt. 771 case at y/L= 0.0 plane.(30.5M nodes)

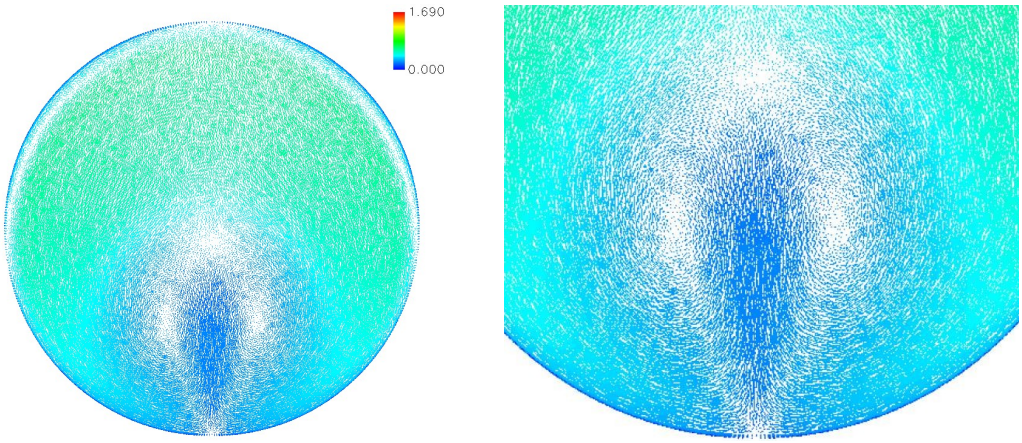

Figure 55:(left) Secondary flow vectors for Pt. 771 case at AIP.(30.5M nodes)

Figure 56:(right) Closer image of secondary flow vectors for Pt. 771 case at AIP.(30.5M nodes)

In addiction to an increase in point count, the AIP rake geometry is included in the 30.5 million node grid and can be seen in figure 54. Between the two computational grids, the slight increase in distortion could be a result of either the finer mesh or the inclusion of the AIP rake. The finer mesh reduces vorticity dissipation due to the grid. It is interesting to note that the AIP rake does not significantly change the secondary flow for the "baseline" case. The counter-rotating vortices still follows the same trend found in the first computational grid. The left vortex rotates counter-clockwise and the right vortex rotates clockwise.

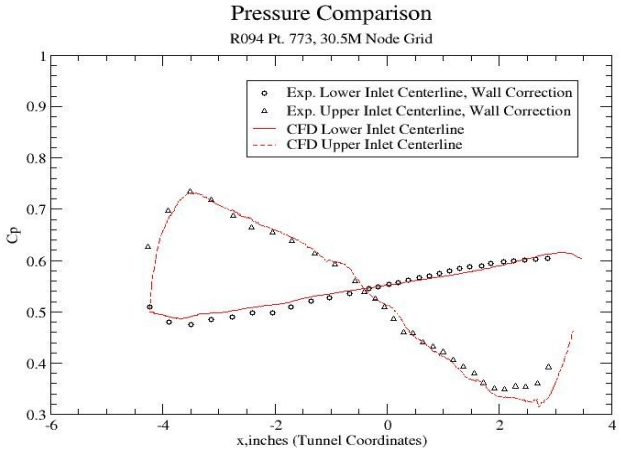

Figure 57: Experimental vs. CFD Centerline pressure Comparison for Pt. 771 case.(30.5M nodes)

Moving on to the R094 Pt. 773 case, figure 57 demonstrates how the CFD centerline pressures match well with the experimental values. Tables 5 and 8 shows that the distortion coefficient error increases from 0.451% to 2.383%. Previously mentioned, the slight increase in distortion could be a result of the increased node count. Adding more nodes and grid elements into the S-bend allows the flow solver to better capture the numerical vorticity. As seen in table 6, the reduction of numerical loss translates into more realistic velocity values towards the exit of the S-duct. The increase in flow rate

through the S-duct could cause the counter rotating vortices to stretch in the stream-wise direction, resulting in larger cross-sectional vortices, increasing distortion. Another possible reason for the increase in distortion could be the newly rendered jet holes. Recall from Chapter 5, the uniform flow conditions declared at the jet grid domains has to travel through 0.1 inches of a constant diameter (0.04 inches). This would result in a more realistic velocity profile injecting into the flow stream. Thus, the jet flow control devices are weaker in strength in comparison to the 6.5 million node grid. To match the experimental distortion values, a re-evaluation of the inflow boundary conditions for the flow control jets is required.

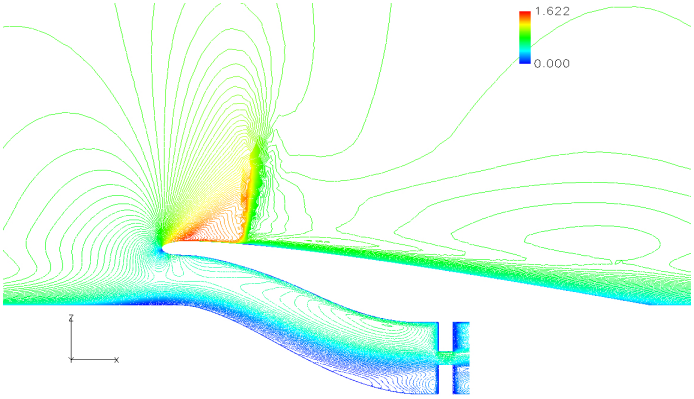

Figure 58: Mach number contour plot for Pt. 773 case at y/L= 0.0 plane.(30.5M nodes)

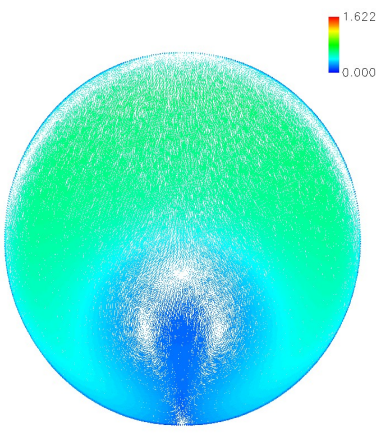

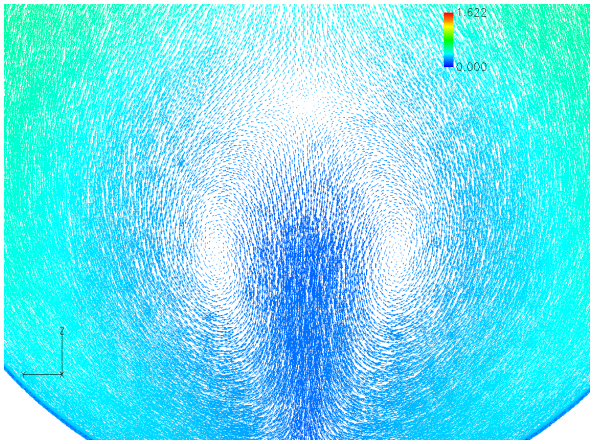

Figure 59:(left) Secondary flow vectors for Pt. 773 case at AIP.(30.5M nodes)

Figure 60:(right) Closer image of secondary flow vectors for Pt. 773 case at AIP.(30.5M nodes)

For the Pt. 773 case, the 30.5 million node grid shows the same flow characteristics to the 6.5 million node grid. The only difference being the increased cross-sectional area of the low pressure region. The counter-rotating vortices still rotate counter-clockwise (left vortex) and clockwise (right vortex). Other than differing from the experimental distortion coefficient by approximately 2.4%, the Pt. 773 case appears to be a valid numerical solution. Minor changes to the jet boundary conditions might increase the accuracy of the numerical distortion value.

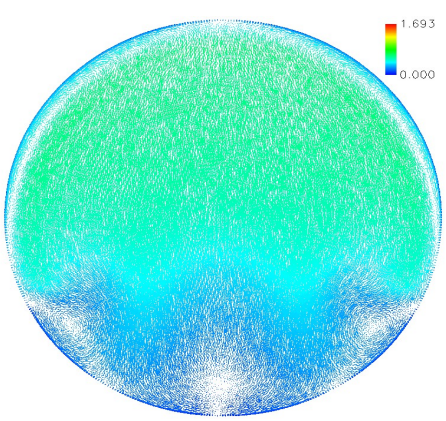

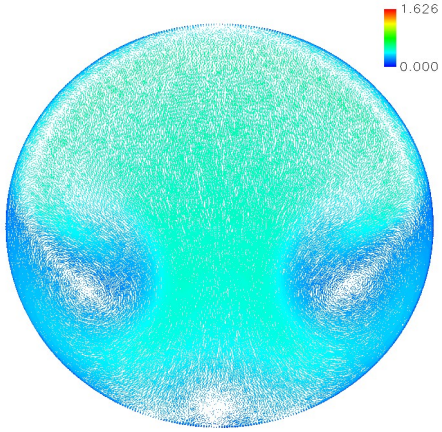

Figure 61:(left) Secondary flow vectors for R094 Pt. 775 case at AIP.(30.5M nodes)

Figure 62:(right) Secondary flow vectors for R094 Pt. 777 case at AIP.(30.5M nodes)

Just like the 6.5 million node grid, a noticeable change in the distortion values takes place between the Pt. 775 and Pt. 777 test cases. As seen in figure 61, the Pt. 775 case interestingly reveals a “transition phase” in the secondary flow physics. Along the symmetry plane, there exists the counter-rotating vortices common to S-bend flows. Yet, two additional vortices have formed along the side walls. From left to right, the vortices rotate clockwise, counter-clockwise, clockwise, and counter-clockwise. Note, the new vortices start out small, and the dominant secondary flow remains to be the counter-rotating vortices located in the center of the duct. Notice in figure 62, the high jet mass flow rate causes the vortices along the wall to become the dominant secondary flow.

Thus, the term “transition phase” describes how the secondary flow changes from center dominance to side wall dominance, as the jet mass flow rate is increased. The relocation of the vortices and low pressure region result in noticeable drops in circumferential distortion.

C. Review of Numerical Results

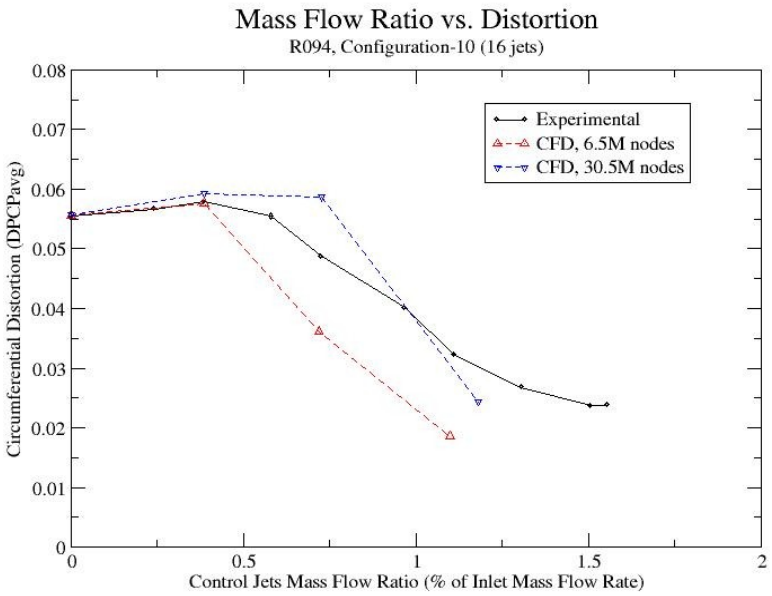

Figure 63: Mass Flow Ratio vs Distortion: Experimental, 6.5M node grid, and 30.5M node grid.

Figure 63 plots distortion curves for the 6.5 million node grid and 30.5 million node grid with respect to the experimental data by Owens, Allan, and Gorton (2006). Even though there is disagreement with experimental distortion values, the computational research provides valuable knowledge and insight into the flow physics linked to distortion reduction within the S-duct. Notice in figure 63, the experimental distortion increases slightly before significantly decreasing. The secondary flow vectors shown in figure 55, 59, 61, and 62 contributes visual evidence of the flow physics, as jet mass flow rate is increased. The “baseline” Pt. 771 case (figure 55) shows vorticity trends common

to S-bend geometries. The Pt. 773 case (figure 59) reveals that the counter-rotating vortices grow in area. The Pt. 775 case (figure 61) captures the creation of two new vortices located on the side walls. Distortion slightly increases due to the growth of the center counter rotating vortices and the creation of two additional vortices located on the side walls. The Pt. 777 case (figure 62) presents visual evidence that the new side wall vortices develop into the dominant secondary flow, and the vortices align themselves in a way to pass flow between the rake geometry. The new knowledge and understanding of the flow physics emphasizes the usefulness of CFD as a engineering tool.

The second computational grid showed more favorable results in reducing numerical loss found in the 6.5 million node grid. Grid revisions like edge resolution of the jet holes and excessive node counts are discussed in Chapter 5. The jet boundary conditions are in need of further examination. As previously stated, limitations with the tunnel geometry and 2.5% scale model prevented experimental measurements of flow parameters at the jet hole edges. Thus, simplifying assumptions have been made for these computational simulations. Sensitivity analysis could be useful in pursuing unequal distribution of the jet mass flow rate and studying injection angles greater than 30 degrees. Boundary conditions monitoring jet momentum instead of density, pressure and velocity could be another direction for future research. Further, post-processing tables and figures for the 30.5 million node grid can be found in Appendix-C.

D. New Questions and a Look at the AIP Rake

Figure 61 and 62 raises a question. Do the flow control devices truly reduce distortion, or do the air jets simply reposition the vorticity in a way that exploits the pressure rake geometry? Figures 64 and 65 have the AIP rake coordinates overlapped on the numerical solutions to show the influence of the geometry. Figure 64 is colored with respect to local Mach number, and figure 65 is colored according to global Mach number. Recall, the 6.5 million node grid does not include the rake solid model while the 30.5 million node grid includes the SAE standard rake geometry.(2002)

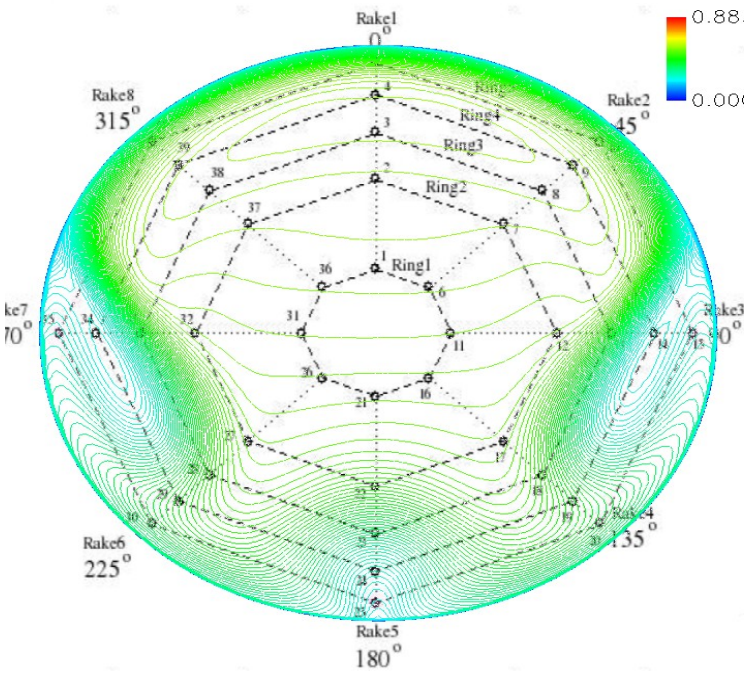

Figure 64: Contour plot at the AIP for R094 Pt. 777 case.(6.5M nodes)

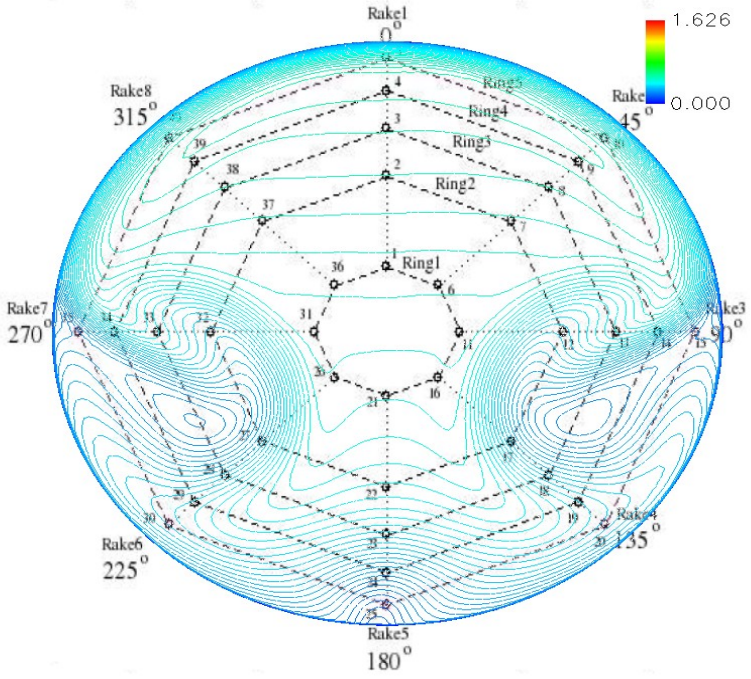

Figure 65: Contour plot at the AIP for R094 Pt. 777 case.(30.5M nodes)

Notice in figure 64 and 65, the high pressure region descends into the low pressure region close to the same angles as pressure rake 4 (135 degrees) and 6 (225 degrees). Also notice, the center of the two vortices on the side walls lie between their respective rakes. This raises another question: at 15% area blockage, how much does the rake influence the vorticity? In the 30.5 million node grid, a stream-wise spacing (in the X-direction) could not be found for positioning the AIP rake. It is completely possible the 0.5 inches between the rake geometry and the AIP is too small. Raising the question, how much of an affect does the rake geometry and rake placement have on experimental measurements? Placing objects directly influences flow paths and flow physics. These are important questions that influence future computational and experimental research. Appendix-C includes post-processing calculations for non-intrusive measurements with a "clocked" (22.5 degrees) AIP rake for the "baseline" case (6.5 million node grid).

Circumferential distortion was also calculated using the combined data from both the standard and “clocked” rakes (80 total non-intrusive measurements). Future research could implement a “clocked” solid model of the AIP rake to see if the vortices continue to align with the rake geometry.

CHAPTER VIII
Conclusions

The intention of this research was to validate the UTC "Tenasi" flow solver while providing analysis on the effectiveness of using air jets as a flow control device. The "Tenasi" flow solver calculated valid numerical solutions for the Pt. 771 and Pt. 773 cases. It is felt that improved estimates of the jet hole inlet boundary conditions would improve the agreement between the computational simulations and experimental values for the higher mass flow ratio cases.

Even though there is disagreement with experimental distortion values, this numerical analysis provides valuable knowledge and insight into the flow physics linked to distortion reduction within the S-duct. This computational study gathered visual evidence of four stages to the secondary flow behavior. The first stage consists of vorticity trends common to S-bend geometries. The secondary flow descends down the side walls, impacts in the middle, and shoots upward resulting in two counter-rotating vortices. In stage two, distortion slightly increases due to the growth of the center counter-rotating vortices. In stage three, the air jets cause the creation of two additional vortices located on the side walls. The new vortices start out small, and the dominant secondary flow remains to be the counter-rotating vortices located in the center of the duct. Stage four shows that the new side wall vortices develop into the dominant secondary flow, and the vortices align themselves in a way to pass flow between the rake geometry. The relocation of the vortices and low pressure region result in noticeable drops in circumferential distortion. This new knowledge and understanding of the flow physics emphasizes the usefulness of CFD as a engineering tool.

The proposed revisions from Chapter 7 present promising ways for pursuing valid numerical solutions for any mass flow ratio. The Pro-E solid model provides a means for future research of any jet configuration which contributes to the future goal of running a numerical simulation of a coupled inlet and turbo fan grid. Overall, the information gathered in this study can aid future computational studies supporting aerodynamic design and development for blended-wing-body (BWB) transport configurations.

LIST OF REFERENCES

Allan, B. G. and Owens, L. R.,, "Numerical Modeling of Flow Control in a Boundary-Layer-Ingesting Offset Inlet Diffuser at Transonic Mach Numbers,"*AIAA-2006-845*, January, 2006.

Anderson B. H. and Gibb J., "Study on Vortex Generator Flow Control for the Management of Inlet Distortion,"*Journal of Propulsion and Power* Vol. 9 No.3, May-June, 1993.

Arabshahi, A., "A Dynamic Multiblock Approach to Solving the Unsteady Euler Equations About Complex Configurations," *Ph.D. Dissertation*, Department of Aerospace Engineering,Mississippi State University, 1989.

Arabshahi, A., and Whitfield, D. L., "Multiblock Euler Computation of Transonic Flow About A Generic Aircraft Configuration," *International Journal of Computational Fluid Dynamics*, Vol.4, pp. 307-321, 1995.

Barnstorff,K.,"X-48B Blended Wing Body", NASA Langley Research Center. *NASA* May 4, 2006. http://www.nasa.gov/vision/earth/improvingflight/x48b.html

Berrier, B. L., Carter M. B., Allen B. G., "High Reynolds Number Investigation of a Flush- Mounted, S-Duct Inlet With Large Amounts of Boundary Layer Ingestion," *NASA/TP- 2005-213766*, Langley Research Center, Hampton, Virginia, September, 2005.

Creech, G., "Skyray 48 Takes Flight", NASA Dryden Flight Research Center. *NASA* September 11, 2007. http://www.nasa.gov/vision/earth/improvingflight/skyray_48.html

FV, Fieldview, *Software Package*, Ver. 12.2.1, Intelligent Light, Rutherford, NJ.

Gatlin, B., "An Implicit, Upwind Method for Obtaining Symbiotic Solutions to the Thin-Layer Navier-Stokes Equations," *Ph.D. Dissertation*, Department of Aerospace Engineering, Mississippi State University, 1987.

Gridgen, Software Package, Ver.15.14, Pointwise Inc., Fort Worth, TX

Hyams, D. G., "An Investigation of Parallel Implicit Solution Algorithms for Incompressible Flows on Unstructured Topologies", *Ph.D. Dissertation*, Mississippi State University, May, 2000.

Karman, S. L., "Unstructured Viscous Layer Insertion Using Linear-Elastic Smoothing", *AIAA Journal*, Volume 45, Number 1, pp.168-180, 2007.

Ortega, J. BLI S-Duct Inlet Model, Inlet Modifications Layout, *Engineering drawings of NASA Model RBD-04-0471*, Advanced Technologies, Incorporated, Newport News, Virginia, August, 2004.

Osher, S., and Chakravarthy, S., "Very High Order Accurate TVD Schemes," *ICASE Report* No. 84-44, 1984.

Owens, L. *Private Communication*, May, 2009.

Owens, L. R., Allan, B. G., and Gorton, S. A., "Boundary-Layer-Ingesting Inlet Flow Control,"*AIAA-2006-839*, January, 2006.

Owens, L. R., Allan, B. G., and Gorton, S. A., "Boundary-Layer-Ingesting Inlet Flow Control," *Journal of Aircraft*,Vol.45, No. 4, pp. 1431-1440, July-August, 2008.

Pro E, Pro Engineer, *Software Package*, Ver. Wildfire 2.0, PTC, Needham, MA

Roe, P. L., "Approximate Riemann Solvers, Parameter Vectors, and Difference Schemes," *Journal of Computational Physics*, Vol. 43, pp. 357-372, 1981.

S-16 Turbine Engine Inlet Flow Distortion Committee, Gas Turbine Engine Inlet Flow Distortion Guidelines, Aerospace Recommended Practice ARP142-B, *Society of Automotive Engineering International*, March 2002, http://www.sae.org/technical/standars/ARP1420B.

Sreenivas, K. and Sawyer S., *research/notes*, University of Tennessee Chattanooga SimCenter, 2008.

Swafford, T. “Computational Fluid Dynamics I: An Introduction to the Fluid Dynamics Equations and Formulations for Numerical Solution”, *lecture notes* ,The University of Tennessee SimCenter at Chattanooga, 2007

Vanden, K. J., “Direct and Iterative Algorithms for Three-Dimensional Euler Equations,” *Ph.D. Dissertation*, Department of Aerospace Engineering, Mississippi State University, 1992.

Whitfield, D. L., Janus, J. M., and Simpson, L. B., “Implicit Finite Volume High Resolution Wave-Split Scheme for Solving the Unsteady Three-Dimensional Euler and Navier-Stokes Equations on Stationary or Dynamic Grids,” *Mississippi State University Engineering and Industrial Research Station Report*, MSSU-EIRS-ASE-88-2, 1988.

APPENDIX-A

C. The Non-Dimensionalization of the Conservation Equations

The following section presents the full non-dimensionalization process for the three conservation equations. According to equation 2.B.7, the mass conservation equation is the following.

$$\frac{\partial \rho}{\partial t}+\frac{\partial}{\partial x_j}(\rho u_j)=0 \tag{2.C.28}$$

To begin, the following rearranged identities from 2.C.1 are inserted into equation 2.C.28.

$$\rho=\hat{\rho}\,\rho_\infty \qquad x_j=\hat{x}_j L \qquad u_j=\hat{u}_j a_\infty \tag{2.C.29}$$

$$\frac{d\hat{t}}{dt}\frac{\partial}{\partial \hat{t}}(\hat{\rho}\,\rho_\infty)+\frac{\partial \hat{x}_j}{\partial x_j}\frac{\partial}{\partial \hat{x}_j}(\hat{\rho}\,\rho_\infty \hat{u}_j a_\infty)=0 \tag{2.C.30}$$

Rearranging the reference variables, equation 2.C.30 becomes

$$\frac{\rho_\infty a_\infty}{L}\frac{\partial \hat{\rho}}{\partial \hat{t}}+\frac{\rho_\infty a_\infty}{L}\frac{\partial}{\partial \hat{x}_j}(\hat{\rho}\,\hat{u}_j)=0 \tag{2.C.31}$$

Divide through by the common leading term $\frac{\rho_\infty a_\infty}{L}$, and we obtain the non-dimensional form of the conservation of mass equation.

$$\frac{\partial \hat{\rho}}{\partial \hat{t}}+\frac{\partial}{\partial \hat{x}_j}(\hat{\rho}\,\hat{u}_j)=0 \tag{2.C.32}$$

Performing the same procedure on the conservation of momentum equation, the procedure starts with equation 2.B.11.

$$\frac{\partial}{\partial t}(\rho u_j)+\frac{\partial}{\partial x_i}(\rho u_j u_i)-\frac{\partial \sigma_{ij}}{\partial x_i}-\rho f_j=0 \tag{2.C.33}$$

Let us use the following identities from 2.C.1 and 2.C.8.

$$\rho=\hat{\rho}\,\rho_\infty \qquad x_j=\hat{x}_j L \qquad u_j=\hat{u}_j a_\infty \qquad f_j=\frac{a_\infty^2}{L}\hat{f}_j \qquad \sigma_{ij}=\hat{\sigma}_{ij}\rho_\infty a_\infty^2 \tag{2.C.34}$$

Inserting identities from 2.C.34 into equation 2.C.33, the momentum equation becomes the following.

$$\begin{gathered}\frac{d\hat{t}}{dt}\frac{\partial}{\partial \hat{t}}(\hat{\rho}\rho_\infty \hat{u}_j a_\infty)+\frac{\partial \hat{x}_i}{\partial x_i}\frac{\partial}{\partial \hat{x}_i}(\hat{\rho}\rho_\infty \hat{u}_j a_\infty \hat{u}_i a_\infty) \\ \frac{-\partial \hat{x}_i}{\partial x_i}\frac{\partial}{\partial \hat{x}_i}(\hat{\sigma}_{ij}\rho_\infty a_\infty^2)-\hat{\rho}\rho_\infty \hat{f}_j\frac{a_\infty^2}{L}=0\end{gathered} \tag{2.C.35}$$

Rearrange the reference terms.

$$\frac{\rho_\infty a_\infty^2}{L}\frac{\partial}{\partial \hat{t}}(\hat{\rho}\hat{u}_j)+\frac{\rho_\infty a_\infty^2}{L}\frac{\partial}{\partial \hat{x}_i}(\hat{\rho}\hat{u}_j\hat{u}_i)-\frac{\rho_\infty a_\infty^2}{L}\frac{\partial}{\partial \hat{x}_i}\hat{\sigma}_{ij}-\frac{\rho_\infty a_\infty^2}{L}\hat{\rho}\ \hat{f}_j=0 \tag{2.C.36}$$

Divide through by the common leading term $\frac{\rho_\infty a_\infty^2}{L}$.

$$\frac{\partial}{\partial \hat{t}}(\hat{\rho}\hat{u}_j)+\frac{\partial}{\partial \hat{x}_i}(\hat{\rho}\hat{u}_j\hat{u}_i)-\frac{\partial}{\partial \hat{x}_i}\hat{\sigma}_{ij}-\hat{\rho}\ \hat{f}_j=0 \tag{2.C.37}$$

Recall, the stress tensor can be further specified in non-dimensional terms by equations 2.C.16 and 2.C.17.

$$\hat{\sigma}_{ij}=-\hat{p}\delta_{ij}+\hat{\tau}_{ij}$$

where

$$\hat{\tau}_{ij}=\frac{1}{Re'_\infty}\left[\delta_{ij}\hat{\lambda}\frac{\partial \hat{u}_k}{\partial \hat{x}_k}+\hat{\mu}\left(\frac{\partial \hat{u}_i}{\partial \hat{x}_j}+\frac{\partial \hat{u}_j}{\partial \hat{x}_i}\right)\right]$$

Inserting equations 2.C.16 and 2.C.17 into equation 2.C.37, we arrive at the final non-dimensional form of the conservation of momentum equation.

$$\begin{gathered}\frac{\partial}{\partial \hat{t}}(\hat{\rho}\hat{u}_j)+\frac{\partial}{\partial \hat{x}_i}(\hat{\rho}\hat{u}_j\hat{u}_i)+\delta_{ij}\frac{\partial \hat{p}}{\partial x_i} \\ \frac{-1}{Re'_\infty}\frac{\partial}{\partial x_i}\left[\delta_{ij}\hat{\lambda}\frac{\partial \hat{u}_k}{\partial \hat{x}_k}+\hat{\mu}\left(\frac{\partial \hat{u}_i}{\partial \hat{x}_j}+\frac{\partial \hat{u}_j}{\partial \hat{x}_i}\right)\right]-\hat{\rho}\ \hat{f}_j=0\end{gathered} \tag{2.C.38}$$

Doing the same for the conservation of energy equation, the process begins with equation 2.B.14, shown immediately following.

$$\frac{\partial}{\partial t}\left[\rho\left(e+\frac{1}{2}u_j\cdot u_j\right)\right]+\frac{\partial}{\partial x_i}\left[\rho\left(e+\frac{1}{2}u_j\cdot u_j\right)u_i\right]$$
$$-\frac{\partial}{\partial x_i}(u_j\cdot\sigma_{ij})-\rho u_j f_j+\frac{\partial q_j}{\partial x_j}=0 \qquad (2.C.39)$$

Recall equation 2.A.29.

$$e_t=e+\frac{1}{2}u_j\cdot u_j$$

Substituting equation 2.A.29 into equation 2.C.39, the conservation of energy equation is presented in terms of total energy, e_t .

$$\frac{\partial}{\partial t}(\rho e_t)+\frac{\partial}{\partial x_i}(\rho e_t u_i)-\frac{\partial}{\partial x_i}(u_j\cdot\sigma_{ij})-\rho u_j f_j+\frac{\partial q_j}{\partial x_j}=0 \qquad (2.C.40)$$

The following rearranged identity equations are found in 2.C.1 and 2.C.8.

$$\rho=\hat{\rho}\,\rho_\infty \qquad x_j=\hat{x}_j L \qquad u_j=\hat{u}_j a_\infty \qquad f_j=\frac{a_\infty^2}{L}\hat{f}_j$$
$$\sigma_{ij}=\hat{\sigma}_{ij}\rho_\infty a_\infty^2 \qquad e_t=\hat{e}_t a_\infty^2 \qquad (2.C.41)$$

Plugging the above into equation 2.C.40, we get the following.

$$\frac{\partial \hat{t}}{\partial t}\frac{\partial}{\partial \hat{t}}(\hat{\rho}\rho_\infty\hat{e}_t a_\infty^2)+\frac{\partial \hat{x}_i}{\partial x_i}\frac{\partial}{\partial \hat{x}_i}(\hat{\rho}\rho_\infty\hat{e}_t a_\infty^2\hat{u}_i a_\infty)$$
$$\frac{-\partial \hat{x}_i}{\partial x_i}\frac{\partial}{\partial \hat{x}_i}(\hat{u}_j a_\infty\cdot\hat{\sigma}_{ij}\rho_\infty a_\infty^2)-\hat{\rho}\rho_\infty\hat{u}_j a_\infty\hat{f}_j\frac{a_\infty^2}{L}+\frac{\partial \hat{x}_j}{\partial x_j}\frac{\partial q_j}{\partial \hat{x}_j}=0 \qquad (2.C.42)$$

Rearrange the reference variables.

$$\frac{\rho_\infty a_\infty^3}{L}\frac{\partial}{\partial \hat{t}}(\hat{\rho}\hat{e}_t)+\frac{\rho_\infty a_\infty^3}{L}\frac{\partial}{\partial \hat{x}_i}(\hat{\rho}\hat{e}_t\hat{u}_i)-\frac{\rho_\infty a_\infty^3}{L}\frac{\partial}{\partial \hat{x}_i}(\hat{u}_j\cdot\hat{\sigma}_{ij})$$
$$\frac{-\rho_\infty a_\infty^3}{L}(\hat{\rho}\hat{u}_j\hat{f}_j)+\frac{1}{L}\frac{\partial q_j}{\partial \hat{x}_j}=0 \qquad (2.C.43)$$

Notice for the common leading term to drop out, the following expression has to be true.

$$\hat{q}_j=\frac{q_j}{\rho_\infty a_\infty^3} \quad \text{Or} \quad q_j=\hat{q}_j\rho_\infty a_\infty^3 \qquad (2.C.44)$$

Applying identity 2.C.44, the energy equation becomes

$$\frac{\partial}{\partial \hat{t}}(\hat{\rho}\,\hat{e}_t)+\frac{\partial}{\partial \hat{x}_i}(\hat{\rho}\,\hat{e}_t\,\hat{u}_i)-\frac{\partial}{\partial \hat{x}_i}(\hat{u}_j\cdot\hat{\sigma}_{ij})-(\hat{\rho}\,\hat{u}_j\hat{f}_j)+\frac{\partial \hat{q}_j}{\partial \hat{x}_j}=0 \qquad (2.C.45)$$

Like the momentum equation, the stress tensor term can be further specified using equations 2.C.16 and 2.C.17. To finish the non-dimensionalization of the energy equation, the heat flux equation (seen in equation 2.B.29) has to be non-dimensionalized.

$$q_j=-\kappa\frac{\partial T}{\partial x_j} \qquad (2.C.46)$$

Recall identities 2.C.26 and 2.C.44.

$$q_i=\hat{q}_i\rho_\infty a_\infty^3 \qquad T=\hat{T}\,a_\infty^2$$

Inserting the identities shown above, Equation 2.C.46 becomes

$$\hat{q}_j=-\kappa\frac{1}{\rho_\infty a_\infty^3}\frac{\partial}{\partial x_j}(\hat{T}\,a_\infty^2) \qquad (2.C.47)$$

Rearrange the reference terms.

$$\hat{q}_j=-\kappa\frac{1}{\rho_\infty a_\infty L}\frac{\partial \hat{T}}{\partial \hat{x}_j} \qquad (2.C.48)$$

Recall our dimensionless expression for temperature (equation 2.C.27).

$$\hat{T}=\frac{\hat{a}^2}{\gamma R}$$

Apply the above into equation 2.C.48.

$$\hat{q}_j=-\kappa\frac{1}{\rho_\infty a_\infty L}\frac{\partial}{\partial \hat{x}_j}\left(\frac{\hat{a}^2}{\gamma R}\right) \qquad (2.C.49)$$

Notice, the ratio of specific heat and gas constants can be brought out of the parenthesis. Rearranging appropriately, equation 2.C.49 becomes

$$\hat{q}_j=-\kappa\frac{1}{\gamma R}\frac{1}{\rho_\infty a_\infty L}\frac{\partial(\hat{a}^2)}{\partial \hat{x}_j} \qquad (2.C.50)$$

Recall equations 2.B.31, 2.B.32, and 2.B.33.

$$\gamma = \frac{c_p}{c_v} \qquad c_p = \frac{\gamma R}{\gamma - 1} \qquad c_v = \frac{R}{\gamma - 1}$$

Applying these equations, the heat flux equation becomes the following.

$$\hat{q}_j = -\frac{c_v}{R}\frac{\kappa}{c_p}\frac{1}{\rho_\infty a_\infty L}\frac{\partial(\hat{a}^2)}{\partial \hat{x}_j} \tag{2.C.51}$$

Simplify the first term.

$$\hat{q}_j = -\frac{1}{\gamma - 1}\frac{\kappa}{c_p}\frac{1}{\rho_\infty a_\infty L}\frac{\partial(\hat{a}^2)}{\partial \hat{x}_j} \tag{2.C.52}$$

Now if we multiply through by a factor of one in the following way.

$$1 = \frac{\mu}{\mu}$$

where μ is the dimensional viscosity term. The non-dimensional Reynolds and Prandtl numbers fall out of equation 2.C.52.

$$Re'_\infty = \frac{\rho_\infty a_\infty L}{\mu_\infty} \qquad Pr = \frac{\mu c_p}{\kappa}$$

Using the identity $\mu = \hat{\mu}\mu_\infty$ from 2.C.1, we complete the non-dimensionalization of the heat flux term.

$$\hat{q}_j = -\frac{1}{\gamma - 1}\frac{\kappa}{c_p \mu}\frac{\hat{\mu}}{1}\frac{\mu_\infty}{\rho_\infty a_\infty L}\frac{\partial(\hat{a}^2)}{\partial \hat{x}_j} \tag{2.C.53}$$

Rearranging, we arrive at the preferred non-dimensional form of the heat flux equation.

$$\hat{q}_j = -\frac{1}{Re'_\infty(\gamma - 1)}\frac{\hat{\mu}}{Pr}\frac{\partial(\hat{a}^2)}{\partial \hat{x}_j} \tag{2.C.54}$$

Presented in equation 2.C.55, the non-dimensional form of the conservation of energy equation was derived after inserting the non-dimensional stress tensor equations (2.C.16 and 2.C17) and heat flux equation (2.C.54) .

$$\frac{\partial}{\partial \hat{t}}(\hat{\rho}\,\hat{e}_t)+\frac{\partial}{\partial \hat{x}_i}(\hat{\rho}\,\hat{e}_t\hat{u}_i)+\delta_{ij}\frac{\partial}{\partial \hat{x}_i}(\hat{u}_j\,\hat{p})-(\hat{\rho}\,\hat{u}_j\,\hat{f}_j)$$
$$-\frac{1}{Re'_\infty}\left[\delta_{ij}\hat{\lambda}\frac{\partial \hat{u}_k}{\partial \hat{x}_k}+\hat{\mu}\left(\frac{\partial \hat{u}_i}{\partial \hat{x}_j}+\frac{\partial \hat{u}_j}{\partial \hat{x}_i}\right)\right] \qquad (2.C.55)$$
$$-\frac{1}{Re'_\infty(\gamma-1)}\frac{\partial}{\partial \hat{x}_j}\left[\frac{\hat{\mu}}{Pr}\frac{\partial(\hat{a}^2)}{\partial \hat{x}_j}\right]=0$$

APPENDIX-B

Fieldview Restart File Equations

Known Values:

$$\gamma = 1.4$$

$$M_r = 0.877$$

$$\rho_r = 1.681$$

note: $\hat{u}$, $\hat{v}$, $\hat{w}$, $\hat{T}_s$ *, and* $\hat{P}_s$ *are standard non-dimensional variables stored at the grid nodes. "Hatted" variables signify non-dimensional numbers.*

Governing Equations:

$$Velocity\ Magnitude = \sqrt{\hat{u}^2 \cdot \hat{v}^2 \cdot \hat{w}^2}$$

$$Local\ Speed\ of\ Sound = \sqrt{\frac{\hat{T}_s}{M_r^2}}$$

$$Local\ Mach\ Number = \frac{Velocity\ Magnitude}{local\ speed\ of\ sound}$$

$$Local\ Total\ Pressure = \hat{P}_s \left[1 + \frac{\gamma - 1}{2} (Local\ Mach\ Number)^2 \right]^{\frac{\gamma}{\gamma - 1}}$$

$$a_r = \sqrt{\gamma R T_s}$$

where R is the gas constant and $T_s = 260$ degrees Kelvin

$$U_r = M_r a_r$$

$$P_s = \rho_r U_r^2 \left[\hat{P}_s + \frac{1}{\gamma M_r^2} \right] \quad \text{(Variable Mach)}$$

$$P_s = \rho_r U_r^2 \hat{P}_s \quad \text{(compressible)}$$

$$\frac{P_t}{P_s} = (1 + \frac{\gamma - 1}{2} M^2)^{\frac{\gamma}{\gamma - 1}}$$

$$Local\ Total\ Pressure = P_s \cdot \frac{P_t}{P_s}$$

APPENDIX-C

AIP Pressure Rakes

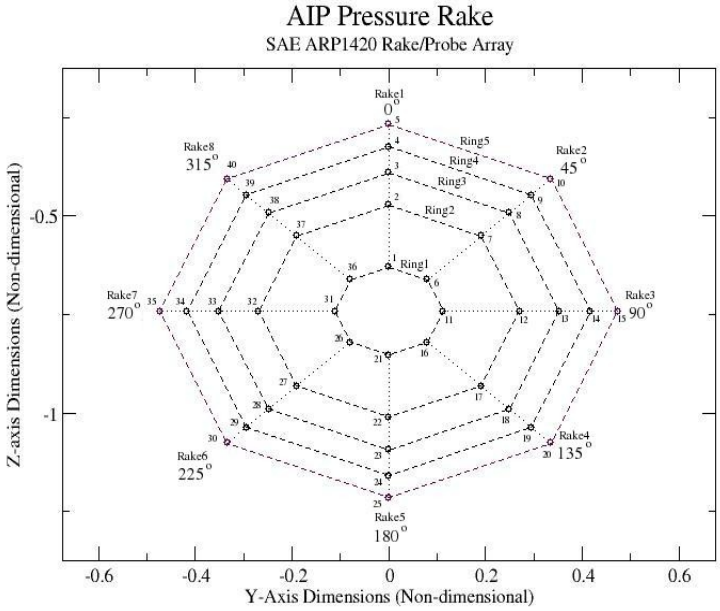

Figure 66: Standard SAE 1420 AIP rake.

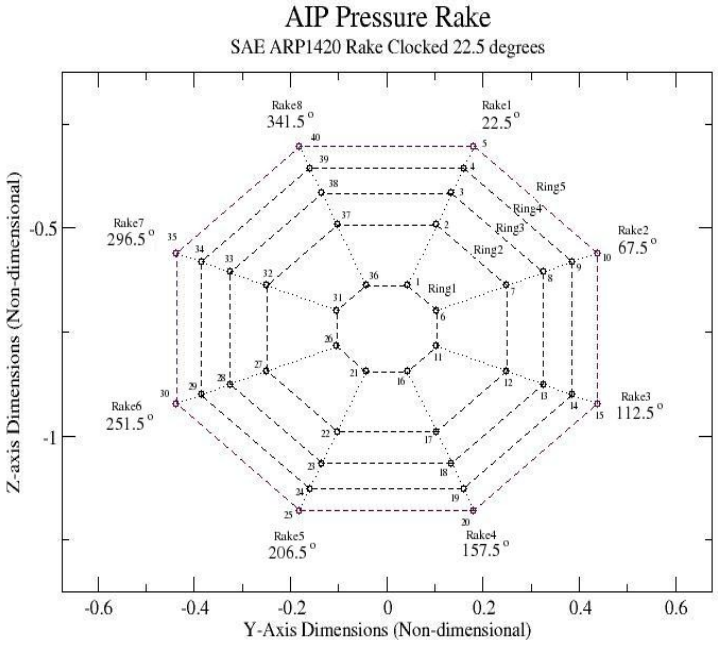

Figure 67: SAE 1420 AIP rake clocked 22.5 degrees.

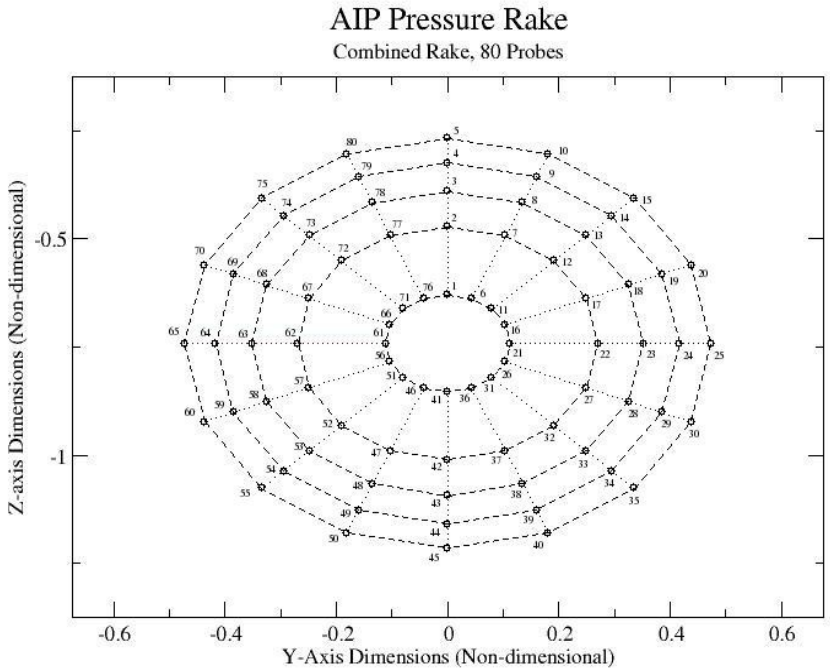

Figure 68: Combined AIP rake. (Figures 66 and Figures 67)

Post Processing 6.5 Million Node Grid

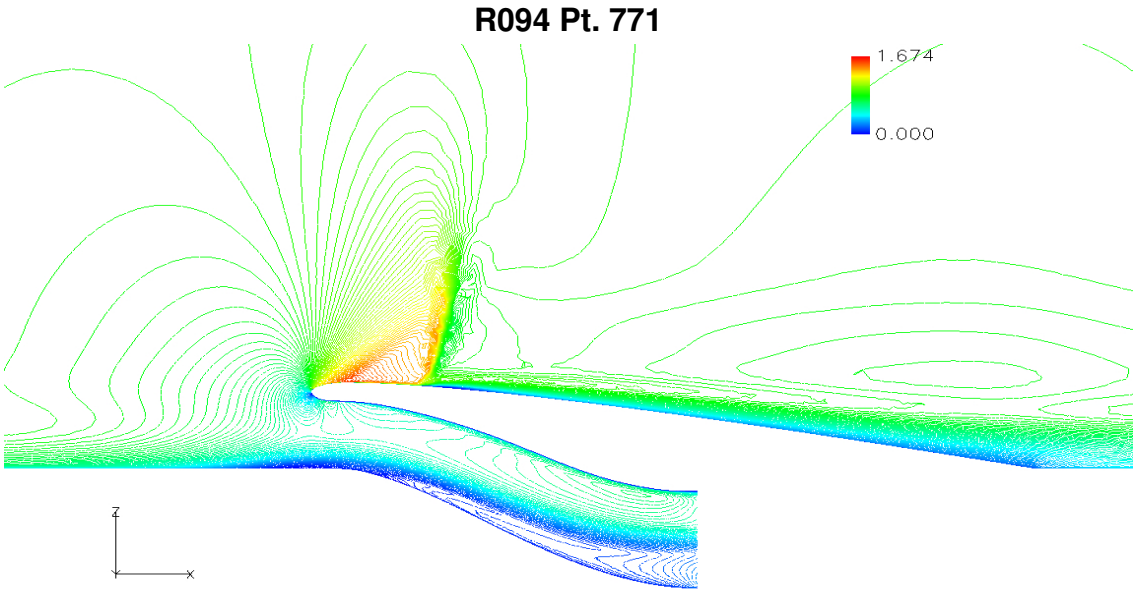

Figure 69: R094 Pt. 771 Contour Plot, y/L=0.0 plane.(Mach)

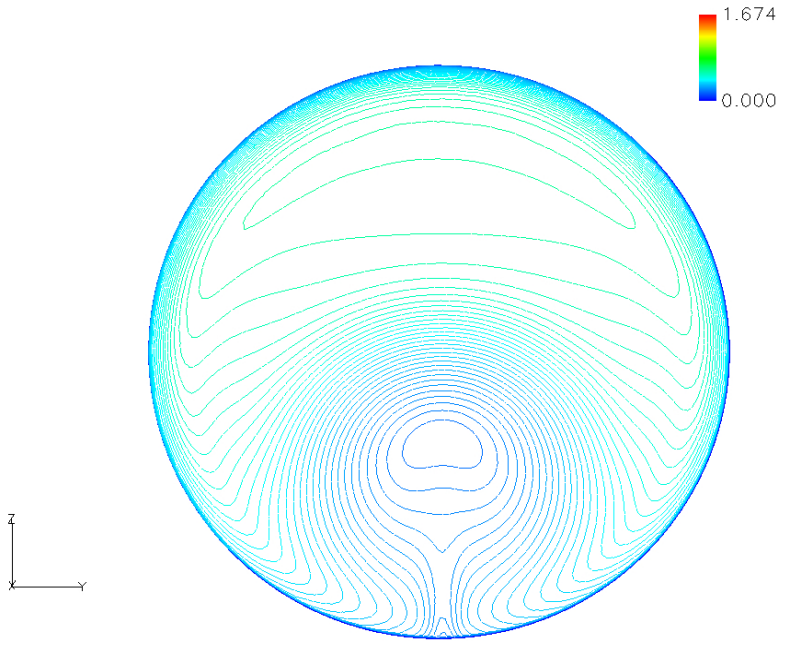

Figure 70: R094 Pt. 771 Contour Plot, AIP. (Mach)

Table 9: SAE 1420 post-processing, R094 Pt. 771. (standard)

	PAV	PAVLOW	Extent	Intensity	DPRP
Ring 1	26.990762	25.576069	183.724021	0.052414	0.036560
Ring 2	28.139712	26.320478	155.783810	0.064650	-0.004452
Ring 3	28.552850	26.789374	153.142431	0.061762	-0.019199
Ring 4	28.770025	27.073311	145.980541	0.058975	-0.026951
Ring 5	27.621637	26.511423	123.423903	0.040194	0.014041

Pt_2 / Pt_∞	Max Pt.	Min Pt.	Mean Pt.	DpCp
0.933678	30.570000	24.759300	28.014997	0.055599

Table 10: SAE 1420 post-processing, R094 Pt. 771.(clocked)

	PAV	PAVLOW	Extent	Intensity	DPRP
Ring 1	26.986800	25.671674	182.067340	0.048732	0.037707
Ring 2	28.114287	26.179003	163.195621	0.068836	-0.002497
Ring 3	28.581200	26.639139	152.832198	0.067949	-0.019146
Ring 4	28.823175	27.072606	149.428809	0.060735	-0.027774
Ring 5	27.715837	26.980879	122.057604	0.026518	0.011711

Pt_2 / Pt_∞	Max Pt.	Min Pt.	Mean Pt.	DpCp
0.934653	30.556500	24.860100	28.044260	0.054554

Table 11: SAE 1420 post-processing, R094 Pt. 771.(combined)

	PAV	PAVLOW	Extent	Intensity	DPRP
Ring 1	26.988781	25.501680	183.251878	0.055101	0.037134
Ring 2	28.127000	26.919719	156.084414	0.078476	-0.003474
Ring 3	28.567025	26.410067	148.698592	0.075505	-0.019172
Ring 4	28.796600	26.818853	145.004014	0.068680	-0.027363
Ring 5	27.668737	26.510727	119.072230	0.041853	0.012875

Pt_2 / Pt_∞	Max Pt.	Min Pt.	Mean Pt.	DpCp
0.934165	30.570000	24.759300	28.029629	0.063923

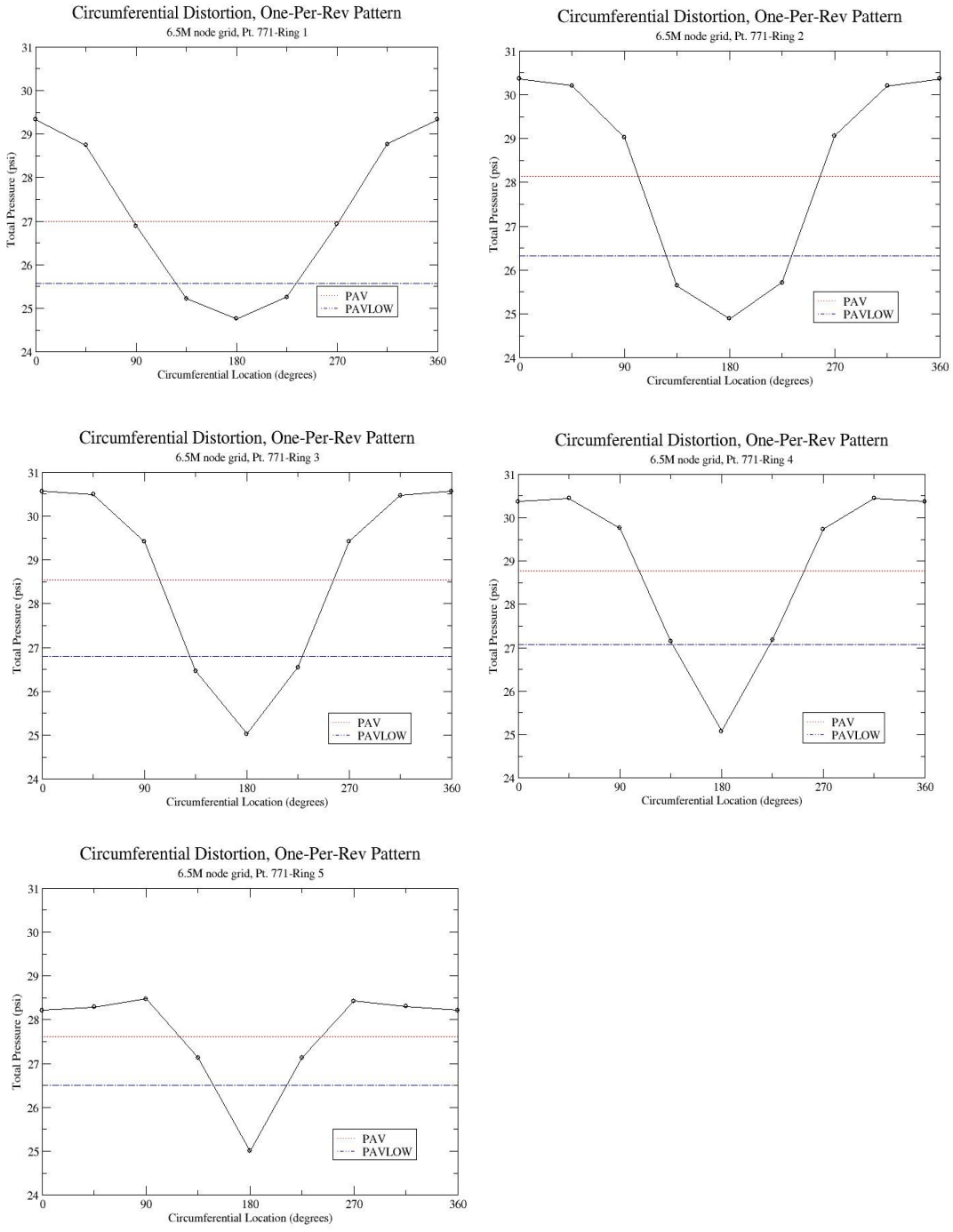

Figure 71: SAE 1420 post-processing plots, R094 Pt. 771.(standard)

R094 Pt. 773

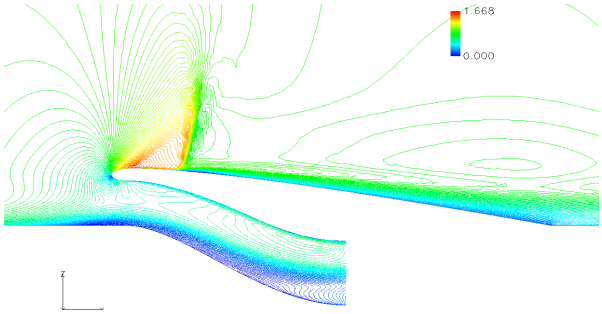

Figure 72: R094 Pt. 773 Contour Plot, y/L=0.0 plane.(Mach)

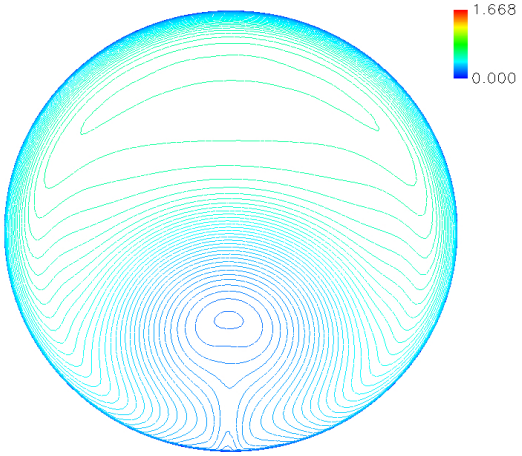

Figure 73: R094 Pt. 773 Contour Plot, AIP.(Mach)

Table 12: SAE 1420 post-processing, R094 Pt. 773.(standard)

	PAV	PAVLOW	Extent	Intensity	DPRP
Ring 1	27.230350	25.919555	177.469849	0.048137	0.027092
Ring 2	28.062025	26.130755	154.630927	0.068821	-0.002622
Ring 3	28.461575	26.599245	152.696098	0.065433	-0.016898
Ring 4	28.686175	26.892471	145.609295	0.062339	-0.024923
Ring 5	27.503013	26.312817	122.106604	0.043275	0.017350

Pt_2 / Pt_∞	Max Pt.	Min Pt.	Mean Pt.	DpCp
0.932799	30.569700	24.537700	27.988627	0.057639

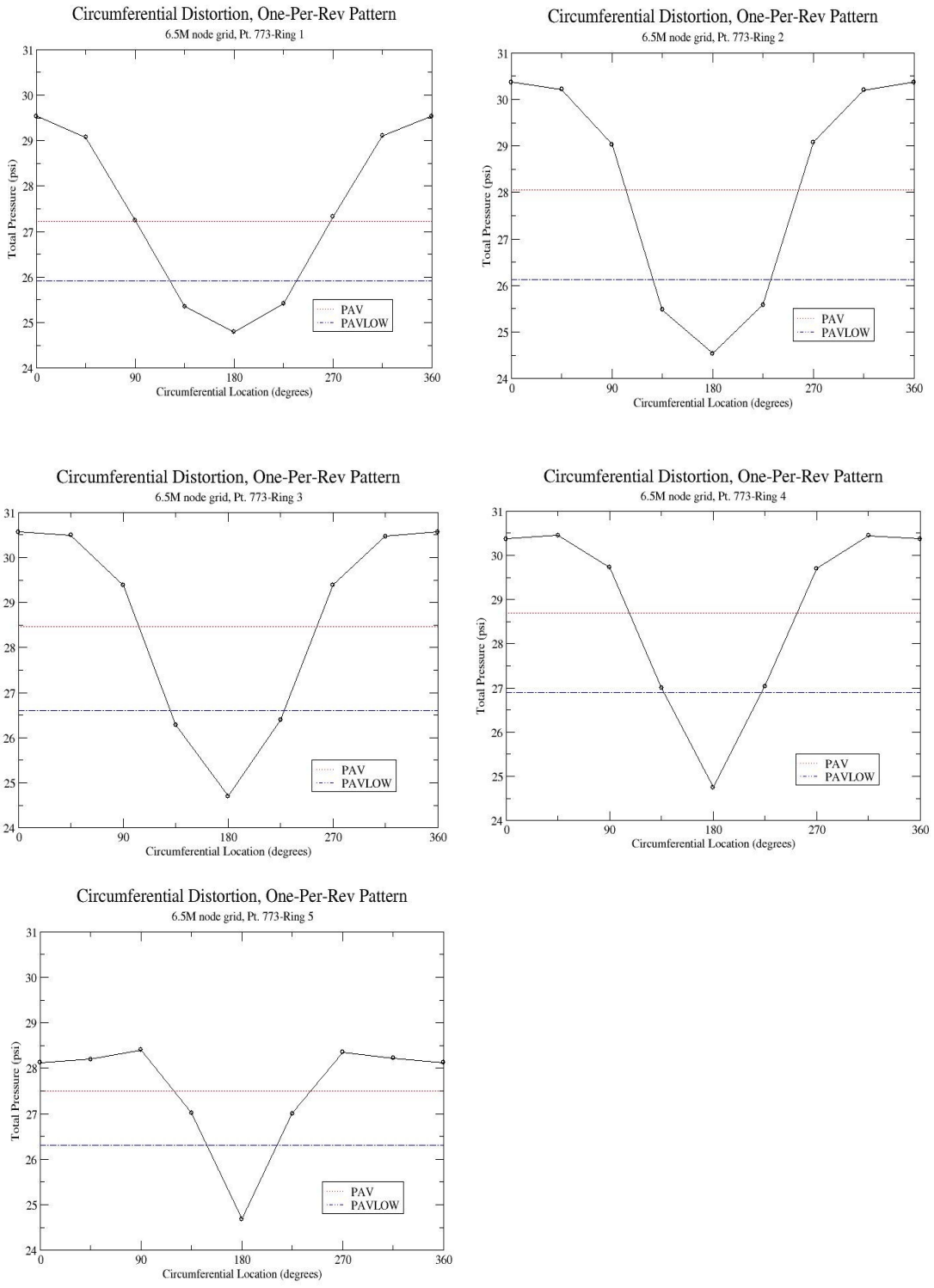

Figure 74: SAE 1420 post-processing plots, R094 Pt. 773.(standard)

R094 Pt. 775

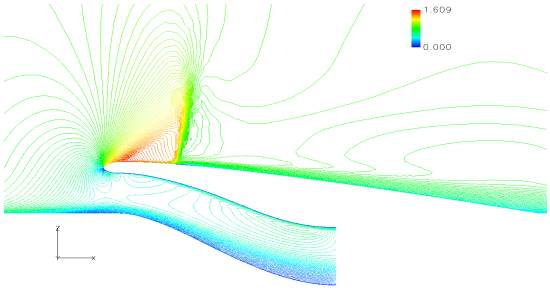

Figure 75: R094 Pt. 775 Contour Plot, y/L=0.0 plane.(Mach)

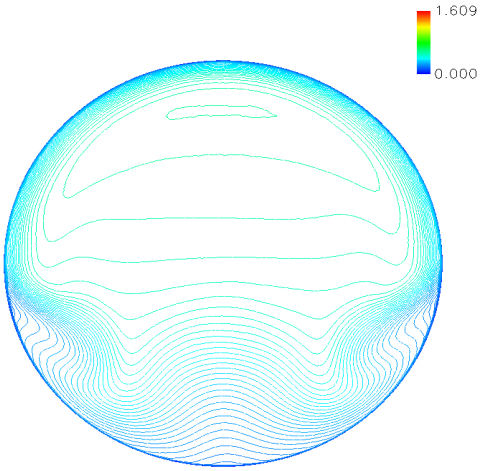

Figure 76: R094 Pt. 775 Contour Plot, AIP. (Mach)

Table 13: SAE 1420 post-processing, R094 Pt. 775.(standard)

	PAV	PAVLOW	Extent	Intensity	DPRP
Ring 1	29.037188	28.747988	157.215206	0.009960	-0.026617
Ring 2	28.757162	27.800610	138.036002	0.033263	-0.016716
Ring 3	28.555550	27.259302	146.367569	0.045394	-0.009588
Ring 4	28.252637	26.704601	147.688262	0.054793	0.001121
Ring 5	26.819225	25.825955	151.101052	0.037036	0.051800

Pt_2 / Pt_∞	Max Pt.	Min Pt.	Mean Pt.	DpCp
0.942655	29.947700	24.742600	28.284353	0.036089

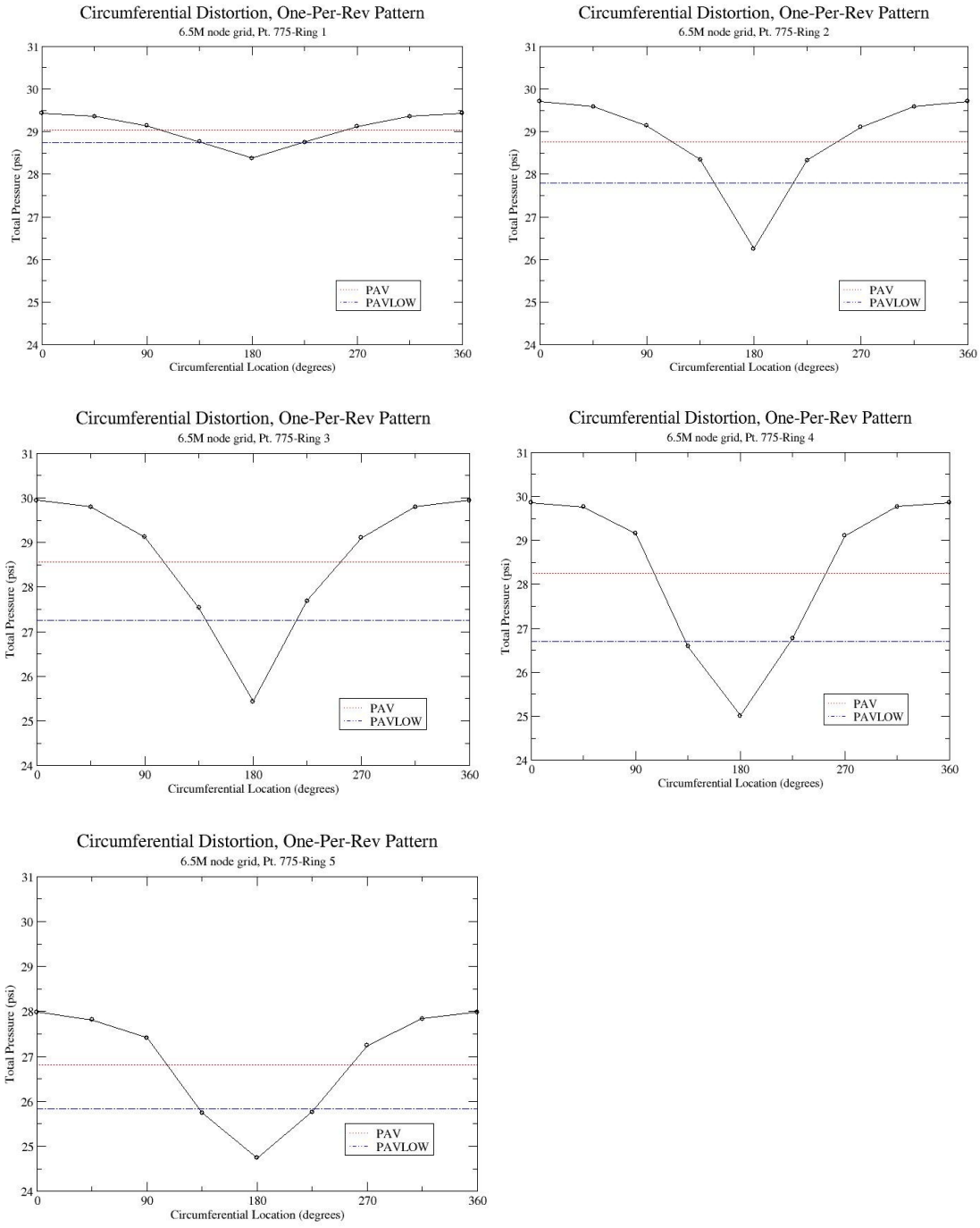

Figure 77: SAE 1420 post-processing plots, R094 Pt. 775.(standard)

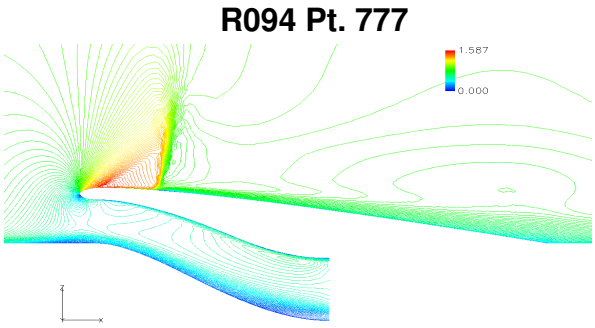

Figure 78: R094 Pt. 777 Contour Plot, y/L=0.0 plane.(local Mach)

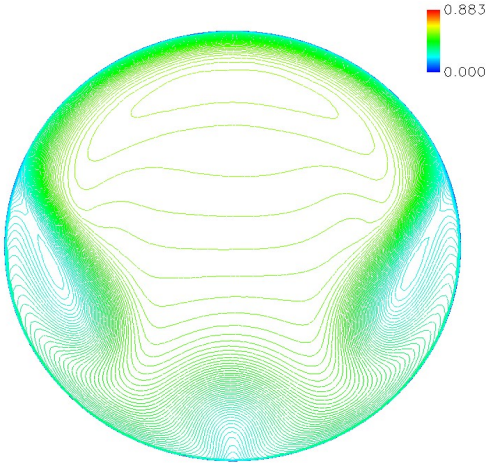

Figure 79: R094 Pt. 777 Contour Plot, AIP plane.(local Mach)

Table 14: SAE 1420 post-processing, R094 Pt. 777.(standard)

	PAV	PAVLOW	Extent	Intensity	DPRP
Ring 1	29.291363	29.163931	173.439628	0.004350	-0.045022
Ring 2	29.056263	28.597689	165.772822	0.015782	-0.036634
Ring 3	28.044137	27.231419	220.272456	0.028980	-0.000535
Ring 4	27.325087	26.376092	225.879241	0.034730	0.025129
Ring 5	26.430300	26.190348	208.527784	0.009079	0.057052

Pt_2 / Pt_∞	Max Pt.	Min Pt.	Mean Pt.	DpCp
0.934159	29.963600	24.900900	28.029430	0.018584

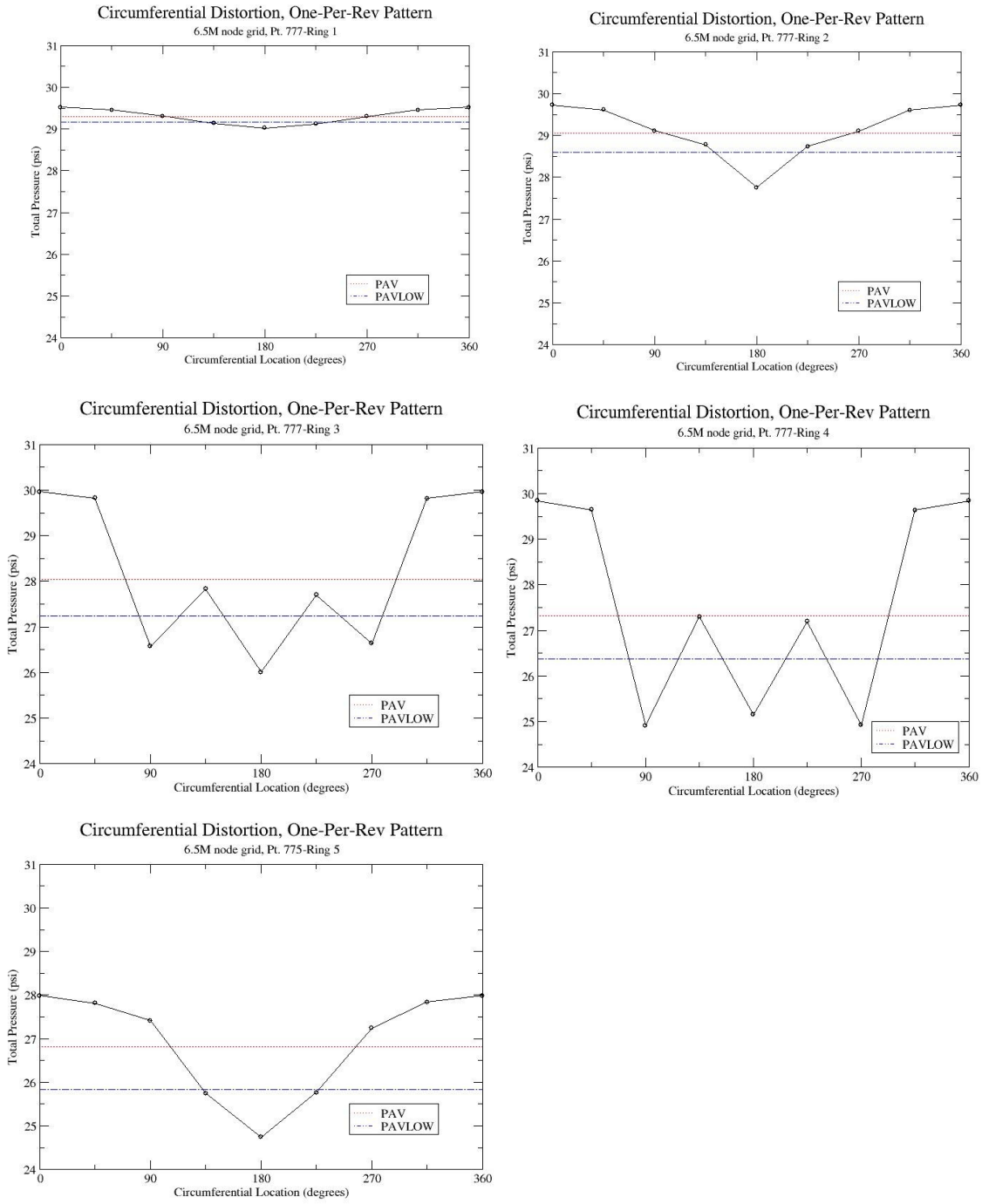

Figure 80: SAE 1420 post-processing plots, R094 Pt. 777.(standard)

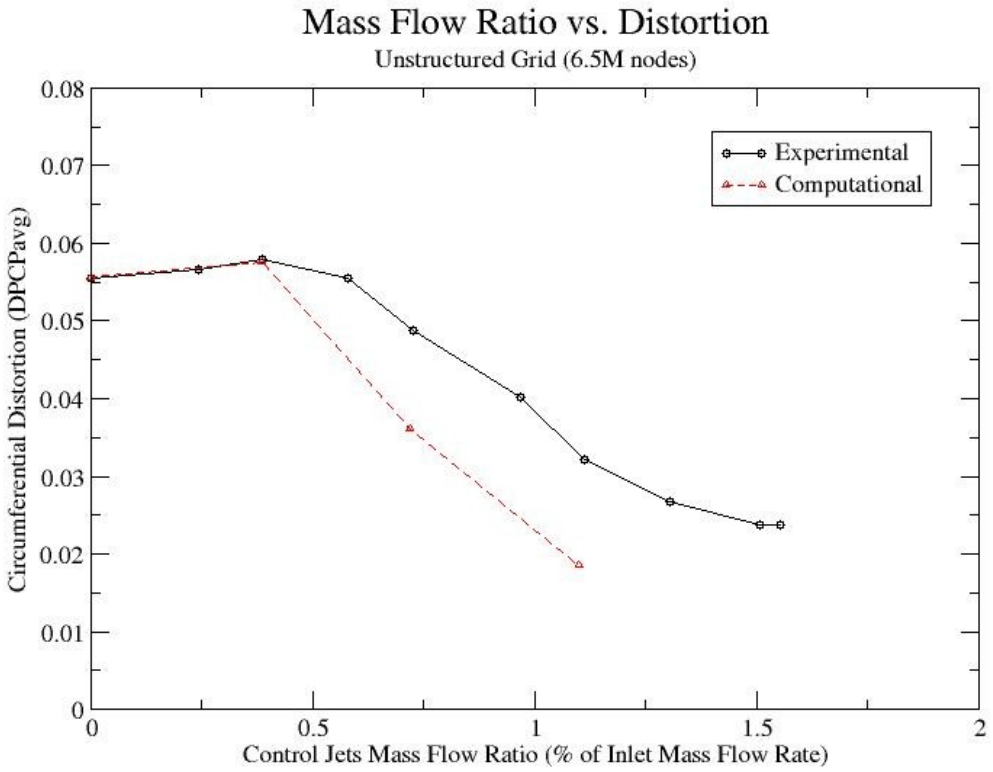

Figure 81: Mass Flow Ratio vs. Distortion.(6.5M grid)

Post Processing 30.5 Million Node Grid

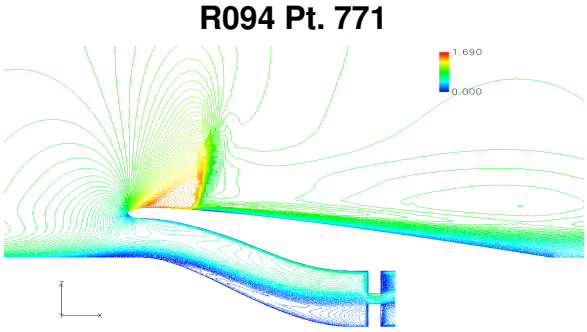

Figure 82: R094 Pt. 771 Contour Plot, y/L=0.0 plane.(Mach)

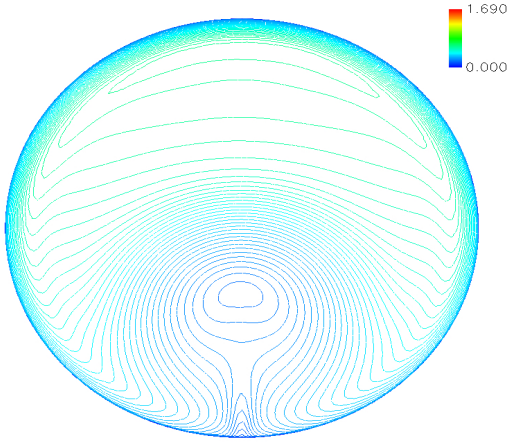

Figure 83: R094 Pt. 771 Contour Plot, AIP.(Mach)

Table 15: SAE 1420 post-processing, R094 Pt. 771. (standard)

	PAV	PAVLOW	Extent	Intensity	DPRP
Ring 1	26.904100	25.564594	186.345331	0.049788	0.038743
Ring 2	28.134338	26.315232	157.126680	0.064658	-0.005212
Ring 3	28.495750	26.745008	152.155499	0.061439	-0.018125
Ring 4	28.831900	27.093085	150.977058	0.060309	-0.030135
Ring 5	27.576187	26.411965	114.919079	0.042218	0.014730

Pt_2 / Pt_∞	Max Pt.	Min Pt.	Mean Pt.	DpCp
0.932824	30.710100	24.767000	27.988455	0.055682

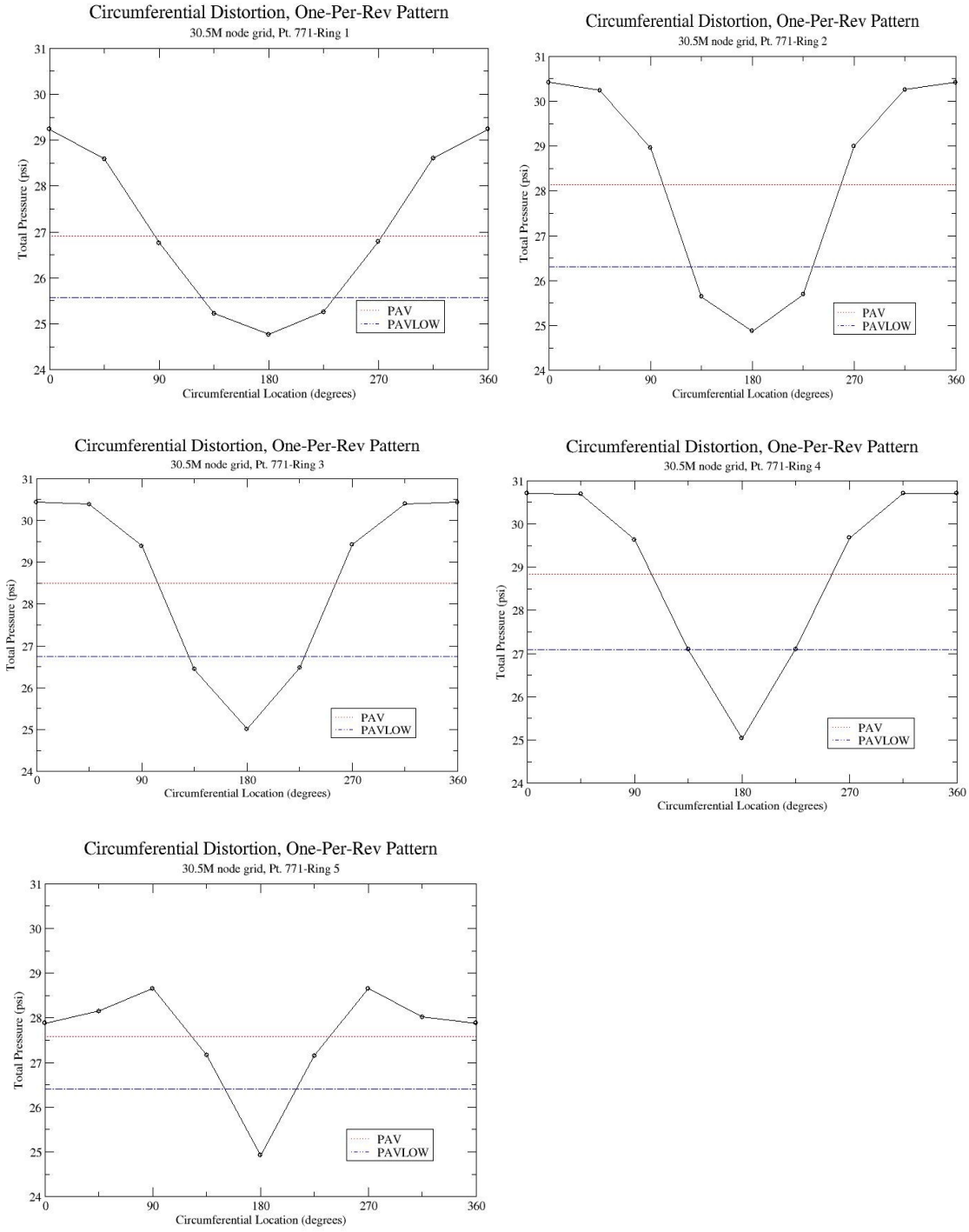

Figure 84: SAE 1420 post-processing plots, R094 Pt. 771. (standard)

R094 Pt. 773

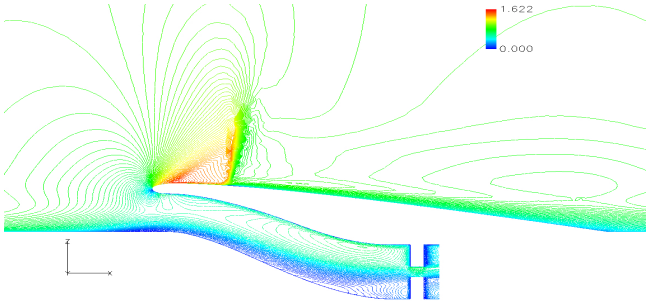

Figure 85: R094 Pt. 773 Contour Plot, y/L=0.0 plane.(Mach)

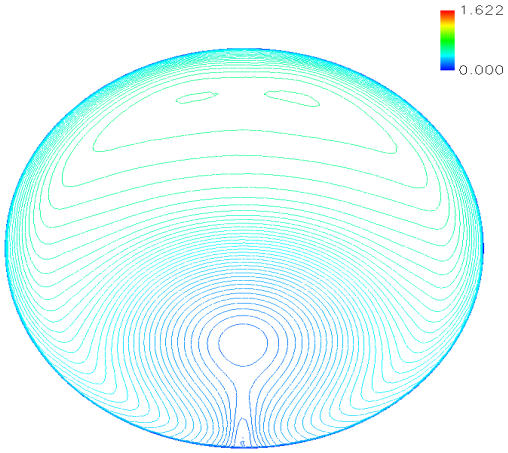

Figure 86: R094 Pt. 773 Contour Plot, AIP.(Mach)

Table 16: SAE 1420 post-processing, R094 Pt. 773.(standard)

	PAV	PAVLOW	Extent	Intensity	DPRP
Ring 1	27.159862	25.718337	180.954395	0.053076	0.027053
Ring 2	27.985163	26.040301	157.170346	0.069496	-0.002512
Ring 3	28.370137	26.467055	152.095598	0.067080	-0.016303
Ring 4	28.530763	26.760455	145.964257	0.062049	-0.022057
Ring 5	27.529287	26.298742	132.272790	0.044700	0.013819

Pt_2 / Pt_∞	Max Pt.	Min Pt.	Mean Pt.	DpCp
0.930377	30.483100	24.366200	27.915042	0.059280

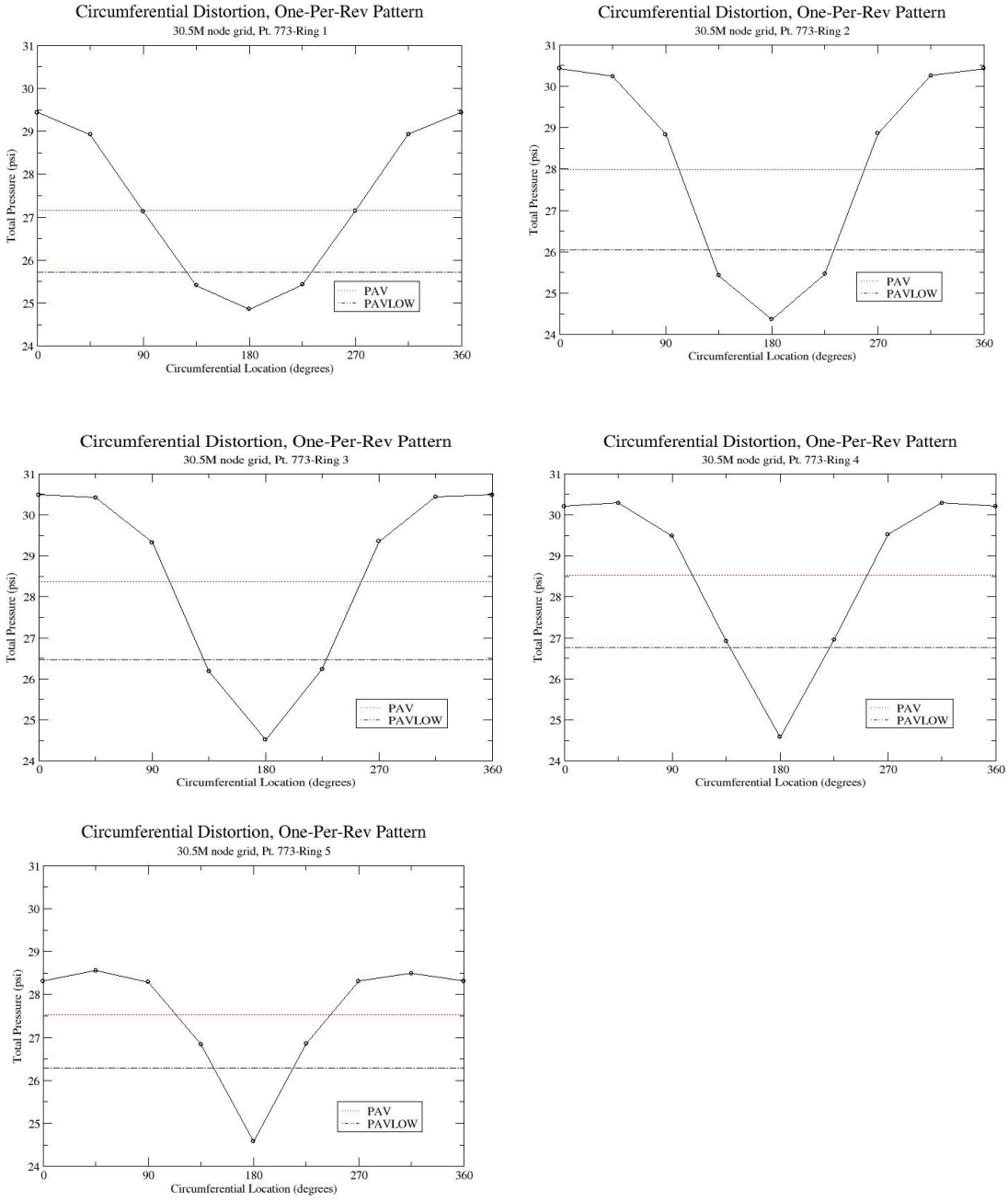

Figure 87: SAE 1420 post-processing plots, R094 Pt. 773.(standard)

R094 Pt. 775

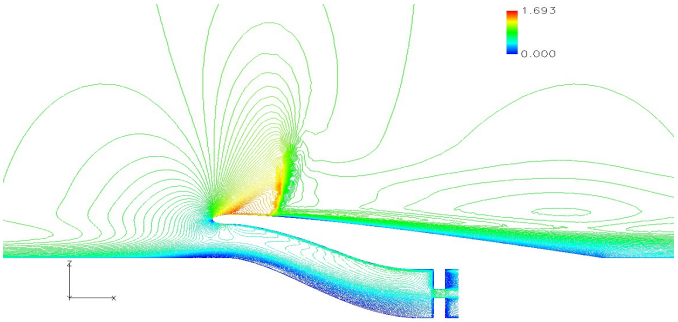

Figure 88: R094 Pt. 775 Contour Plot, y/L=0.0 plane.(Mach)

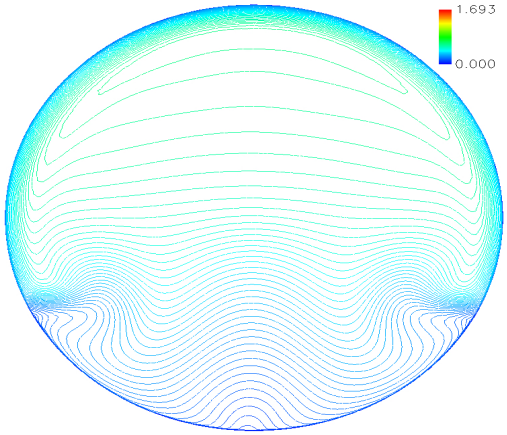

Figure 89: R094 Pt. 775 Contour Plot, AIP.(Mach)

Table 17: SAE 1420 post-processing, R094 Pt. 775.(standard)

	PAV	PAVLOW	Extent	Intensity	DPRP
Ring 1	28.584063	27.677894	161.142876	0.031702	-0.022725
Ring 2	28.365625	26.763884	159.111585	0.056468	-0.014909
Ring 3	28.037325	26.090710	158.179977	0.069429	-0.003163
Ring 4	28.087000	25.857697	156.276778	0.079371	-0.004940
Ring 5	26.670625	25.167982	141.098474	0.056341	0.045737

Pt_2 / Pt_∞	Max Pt.	Min Pt.	Mean Pt.	DpCp
0.931507	30.727900	24.050400	27.948927	0.067554

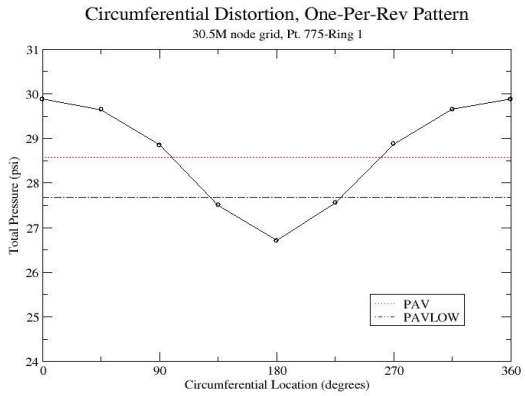

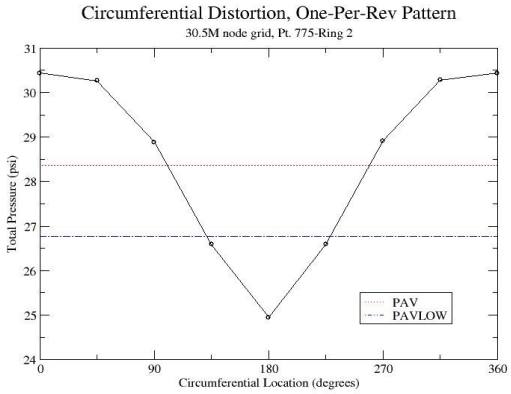

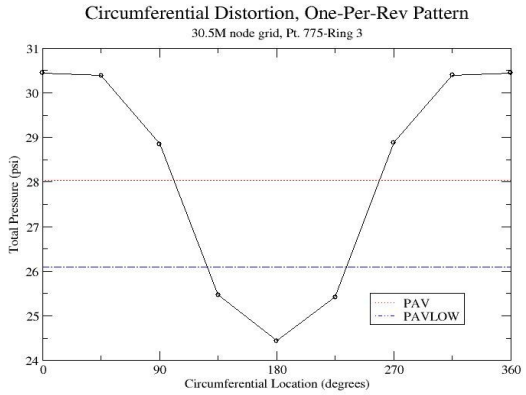

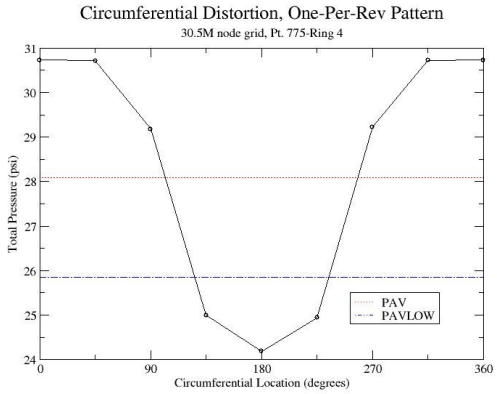

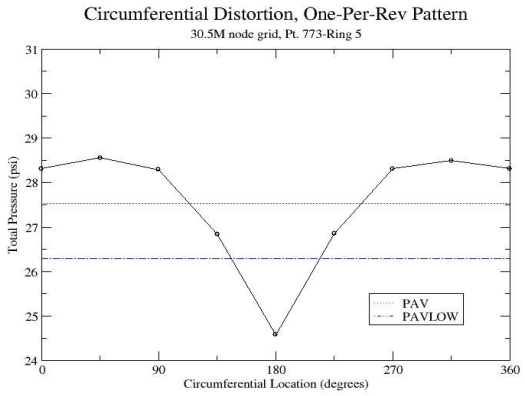

Figure 90: SAE 1420 post-processing plots, R094 Pt. 775.(standard)

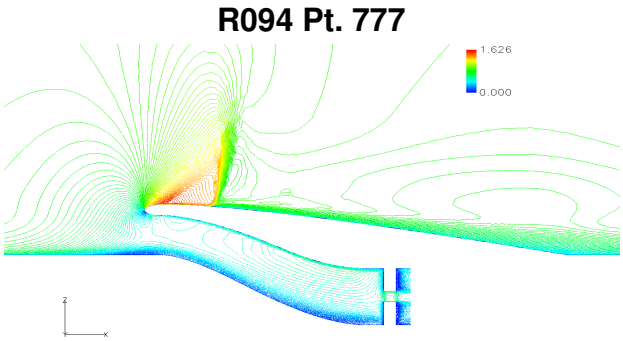

Figure 91: R094 Pt. 777 Contour Plot, y/L=0.0 plane.(Mach)

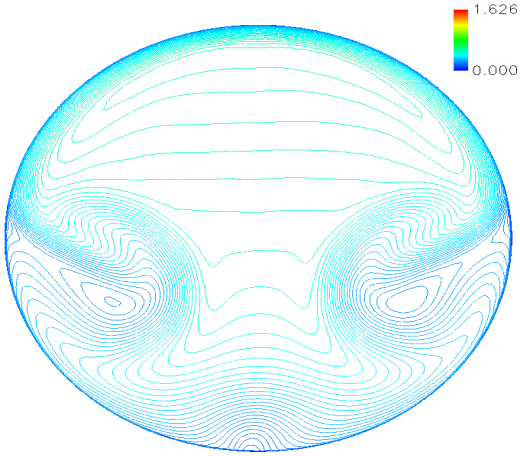

Figure 92: R094 Pt. 777 Contour Plot, AIP. (Mach)

Table 18: SAE 1420 post-processing, R094 Pt. 777.(standard)

	PAV	PAVLOW	Extent	Intensity	DPRP
Ring 1	29.633550	29.489922	188.825071	0.004847	-0.040508
Ring 2	28.363788	27.642251	202.195919	0.025439	0.004077
Ring 3	28.597250	27.628319	201.890170	0.033882	-0.041200
Ring 4	28.418988	27.420160	216.640864	0.035146	0.002139
Ring 5	27.385925	26.767916	224.601695	0.022567	0.038412

Pt_2 / Pt_∞	Max Pt.	Min Pt.	Mean Pt.	DpCp
0.949203	30.624600	25.877400	28.479900	0.024376

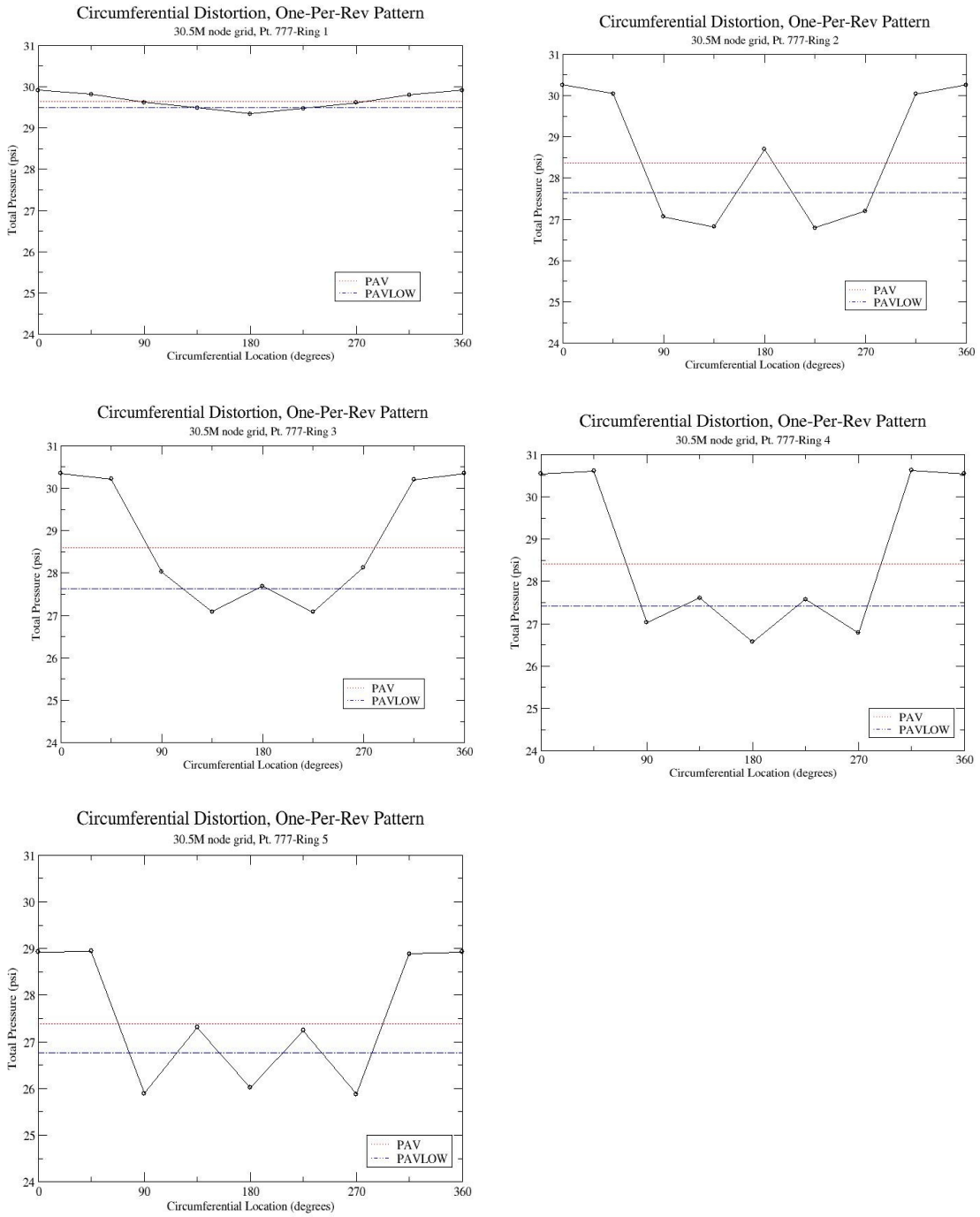

Figure 93: SAE 1420 post-processing plots, R094 Pt. 777.(standard)

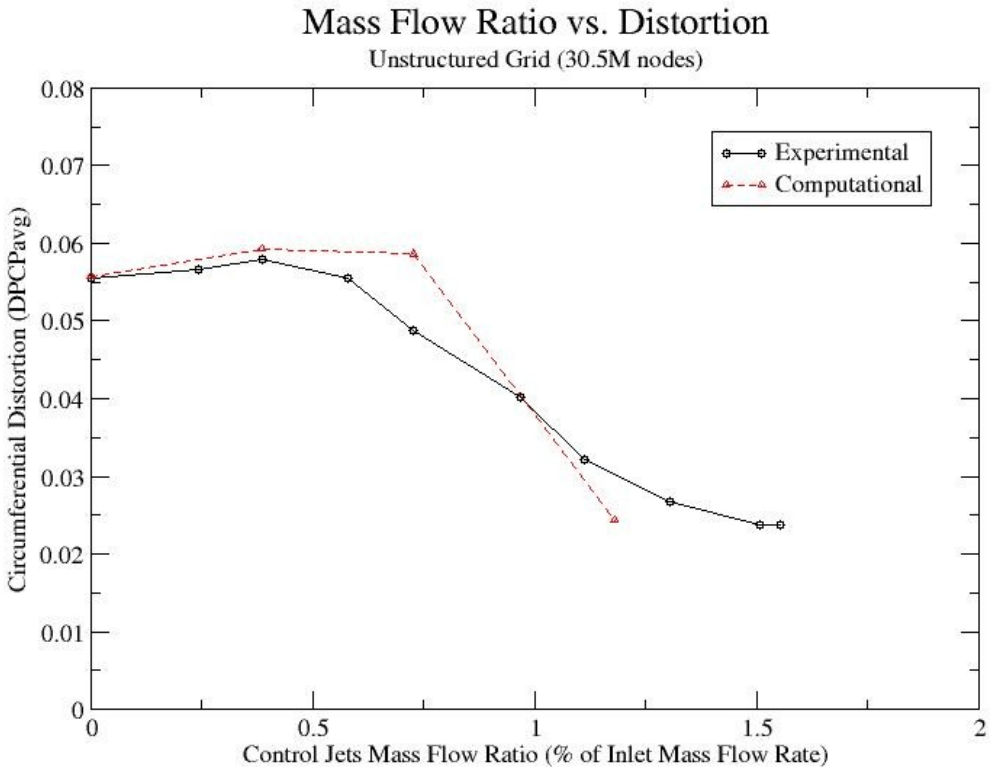

Figure 94: Mass Flow Ratio vs. Distortion.(30.5M grid)

VITA

Benjamin Craig Johnson was born in Knoxville ,Tn. He attended Gibbs High School, graduating in spring of 2003. Benjamin was accepted into the College of Engineering at the Tennessee Technological University in Cookeville, Tn. In the spring of 2007, he graduated with a Bachelors of Science in Mechanical Engineering. The following fall semester, Benjamin entered the Computational Engineering program at the Chattanooga SimCenter at the University of Tennessee Chattanooga. January 2010, Benjamin presented his research at the 48th AIAA aerospace science meeting in Orlando, Florida.

Email Address: BenjaminCJohnson85@gmail.com

Thesis was typed by the author.